NONLINEAR FREQUENCY CONVERSION IN III-V SEMICONDUCTOR PHOTONIC CRYSTALS

A DISSERTATION
SUBMITTED TO THE DEPARTMENT OF ELECTRICAL ENGINEERING
AND THE COMMITTEE ON GRADUATE STUDIES
OF STANFORD UNIVERSITY
IN PARTIAL FULFILLMENT OF THE REQUIREMENTS
FOR THE DEGREE OF
DOCTOR OF PHILOSOPHY

Kelley Rivoire
March 2012

Report Documentation Page

Form Approved
OMB No. 0704-0188

1. REPORT DATE **MAR 2012**	2. REPORT TYPE	3. DATES COVERED **00-00-2012 to 00-00-2012**

4. TITLE AND SUBTITLE **Nonlinear Frequency Conversion in III-V Semiconductor Photonic Crystals**	5a. CONTRACT NUMBER 5b. GRANT NUMBER 5c. PROGRAM ELEMENT NUMBER
6. AUTHOR(S)	5d. PROJECT NUMBER 5e. TASK NUMBER 5f. WORK UNIT NUMBER
7. PERFORMING ORGANIZATION NAME(S) AND ADDRESS(ES) **Stanford University,E. L. Ginzton Laboratory,Stanford,CA,94305**	8. PERFORMING ORGANIZATION REPORT NUMBER
9. SPONSORING/MONITORING AGENCY NAME(S) AND ADDRESS(ES)	10. SPONSOR/MONITOR'S ACRONYM(S) 11. SPONSOR/MONITOR'S REPORT NUMBER(S)

12. DISTRIBUTION/AVAILABILITY STATEMENT

Approved for public release; distribution unlimited

13. SUPPLEMENTARY NOTES

14. ABSTRACT

Nonlinear optical processes provide a physical mechanism for converting the frequency of light. This allows the generation of tunable light sources at wavelengths inaccessible with lasers, leading to a diverse set of applications in fields such as spectroscopy sensing, and metrology. To make these processes efficient has conventionally required relatively exotic materials that are incompatible with state of the art nanofabrication resulting in large-area devices that operate at high optical powers and cannot be integrated with on-chip optical and electronic circuits. This dissertation shows how optical nanocavities, by localizing light into sub-cubic optical wavelength volumes with long photon storage times, can greatly enhance the efficiency of nonlinear frequency conversion processes in III-V semiconductors, while simultaneously shrinking the device footprint, reducing the operating power, and providing a scalable on-chip platform. This approach also enables on-chip quantum frequency conversion interfaces, which are crucial for the construction of quantum networks. First, photonic crystal nanocavities in gallium phosphide are shown to generate second harmonic radiation with only nanowatts of coupled optical powers, and efficiency many orders of magnitude greater than in previous nanoscale devices. This approach is then extended to demonstrate sum-frequency generation in GaP photonic crystal cavities with multiple cavity modes, as well as broadband upconversion employing photonic crystal waveguides. The nanocavity-enhanced second harmonic generation is then integrated with a single quantum dot to create a single photon source triggered at 300 MHz by a telecommunication wavelength laser coupled with an external electro-optic modulator, a simpler and faster configuration than standard approaches. The efficiency of all the aforementioned processes can be further improved through resonant photonic crystal nanocavities allowing large frequency separation, which are described in this thesis. Finally, this dissertation presents spectroscopic measurements of quantum systems that emit photons at visible wavelengths, which are promising candidates for a number of quantum and classical applications and well-suited for integration with on-chip frequency conversion.

15. SUBJECT TERMS

16. SECURITY CLASSIFICATION OF:			17. LIMITATION OF ABSTRACT	18. NUMBER OF PAGES	19a. NAME OF RESPONSIBLE PERSON
a. REPORT **unclassified**	b. ABSTRACT **unclassified**	c. THIS PAGE **unclassified**	**Same as Report (SAR)**	**158**	

Standard Form 298 (Rev. 8-98)
Prescribed by ANSI Std Z39-18

I certify that I have read this dissertation and that, in my opinion, it is fully adequate in scope and quality as a dissertation for the degree of Doctor of Philosophy.

Jelena Vuckovic, Primary Adviser

I certify that I have read this dissertation and that, in my opinion, it is fully adequate in scope and quality as a dissertation for the degree of Doctor of Philosophy.

Shanhui Fan

I certify that I have read this dissertation and that, in my opinion, it is fully adequate in scope and quality as a dissertation for the degree of Doctor of Philosophy.

David Miller

Approved for the Stanford University Committee on Graduate Studies.

Patricia J. Gumport, Vice Provost Graduate Education

Abstract

Nonlinear optical processes provide a physical mechanism for converting the frequency of light. This allows the generation of tunable light sources at wavelengths inaccessible with lasers, leading to a diverse set of applications in fields such as spectroscopy, sensing, and metrology. To make these processes efficient has conventionally required relatively exotic materials that are incompatible with state of the art nanofabrication, resulting in large-area devices that operate at high optical powers and cannot be integrated with on-chip optical and electronic circuits.

This dissertation shows how optical nanocavities, by localizing light into sub-cubic optical wavelength volumes with long photon storage times, can greatly enhance the efficiency of nonlinear frequency conversion processes in III-V semiconductors, while simultaneously shrinking the device footprint, reducing the operating power, and providing a scalable on-chip platform. This approach also enables on-chip quantum frequency conversion interfaces, which are crucial for the construction of quantum networks.

First, photonic crystal nanocavities in gallium phosphide are shown to generate second harmonic radiation with only nanowatts of coupled optical powers, and efficiency many orders of magnitude greater than in previous nanoscale devices. This approach is then extended to demonstrate sum-frequency generation in GaP photonic crystal cavities with multiple cavity modes, as well as broadband upconversion employing photonic crystal waveguides. The nanocavity-enhanced second harmonic generation is then integrated with a single quantum dot to create a single photon source triggered at 300 MHz by a telecommunication wavelength laser coupled with an external electro-optic modulator, a simpler and faster configuration than standard approaches.

The efficiency of all the aforementioned processes can be further improved through resonant photonic crystal nanocavities allowing large frequency separation, which are described in this thesis. Finally, this dissertation presents spectroscopic measurements of quantum systems that emit photons at visible wavelengths, which are promising candidates for a number of quantum and classical applications and well-suited for integration with on-chip frequency conversion.

Acknowledgments

Over the course of my years at Stanford, I benefited enormously from the presence and assistance of a number of people who made my doctoral research possible as well as enjoyable.

I would very much like to thank my PhD advisor, Prof. Jelena Vučković, for the time I spent in her group. Within my first year in the group, I became interested in using the material gallium phosphide, and I was floored that Jelena trusted and supported my work enough to finance a custom-grown wafer. I have appreciated this level of support throughout my PhD work, which included starting new projects, building a new lab, and initiating many collaborations. I would also like to acknowledge the other members of my committee, Prof. David Miller and Prof. Shanhui Fan, and thank Prof. Hideo Mabuchi for chairing my oral defense.

I have spent an enormous amount of time with the talented and hardworking researchers in the Vuckovic group, all of whom I consider colleagues and friends. Andrei Faraon guided me in collecting the first data from gallium phosphide structures and always found time to help in the lab; I also benefited early in my PhD from the assistance of Dirk Englund and Vanessa Sih. Subsequently, I was fortunate to collaborate with newer members of the group, most significantly with Ziliang (Carter) Lin, who helped with the first frequency conversion experiments and always provided a detailed and critical perspective, and Sonia Buckley, who always has immense energy and dedication for whatever she pursues. I have also enjoyed collaborative work with Michal Bajcsy, Bryan Ellis, Olivia Grubert, Jesse Lu, Arka Majumdar, Marina Radulaski, and Gary Shambat. I would like to thank all the other members of the Vuckovic group with whom I interacted as well – Ilya Fushman, Yiyang Gong, Hideo Iwase, Erik Kim, Nicholas Manquest, Jan Petykiewicz, Armand Rundquist, and Mitsuru Toishi, as well as our group administrator, Ingrid Tarien.

In addition to my labmates, I was able to collaborate with many wonderful researchers outside our group. I was fortunate to collaborate for many projects with Fariba Hatami at Humboldt University, whose fantastic work growing gallium phosphide-based materials was a key ingredient for many of the experiments described in this thesis. Anika Kinkhabwala and Prof. W.E. Moerner at Stanford collaborated on work to couple molecules to photonic crystals and always challenged me to think more deeply and carefully about the details of my work. Toward the end of my PhD, I enjoyed collaborative work with Yuncheng Song and Prof. Minjoo Larry Lee at Yale on InGaAs/GaP quantum dots; I would also like to thank Prof. Lee for arranging my visit to Yale. Additionally Hyochul Kim and Prof. Pierre Petroff from UCSB provided the InAs/GaAs quantum dots used to build a faster telecom wavelength-pumped quantum dot single photon source; Yuri Avlasevich and Prof. Klaus Mullen at the Max Planck Institute for Polymer Research contributed the DNQDI molecules used in our work with the Moerner group; Dr. Klaus Biermann from the Paul Drude Institute provided very recent growth of (111)-oriented GaAs; and Tomas Sarmiento in the group of Prof. Jim Harris at Stanford collaborated on the growth of (111) material as well as growing numerous quantum well and quantum dot samples we used for fabricating test structures.

I would also like to thank the Stanford photonics and nanofabrication student communities, from whom I have received a tremendous amount of technical advice as well as encouragement. I am very appreciative of Seth Lloyd, Jesse Lu, and Lieven Verslegers for their help throughout the years from quals practice to defense practice talks. I would also like to acknowledge Seth Lloyd, Vicky Wen, Jason Pelc, Qiang Zhang, Peter McMahon, Liz Edwards, Stephanie Claussen, and Krishna Balram for lending equipment I used in experiments. Across Ginzton and the new Nano building, as well as CIS and McCullough, I benefited from the technical guidance and friendship of many others. Many staff members in SNF and SNC went beyond the call of duty to help me with processing; I would especially like to thank James Conway, Rich Tiberio, Jim Kruger, Elmer Enriquez, Cesar Baxter, and Uli Thumser.

I would like to acknowledge the sources of funding for this work, including: the National Science Foundation Graduate Research Fellowship, the Stanford Graduate Fellowship, the MARCO Interconnect Focus Center, the National Science Foundation, the Army Research Office, the Air Force Office of Scientific Research, and CIS Seed Funding. The work was performed in part at the Stanford Nanofabrication Facility of NNIN.

Finally, my research and life beyond have also been supported through the friendships of many wonderful people too numerous to list. I would especially like to thank Faye Kasemset, who has been a fantastic friend and roommate over my years at Stanford and MIT, and Yang Wang, who has made the last year even happier. I would also like to thank my family for support and perspective through the years. My grandfather, Bernard Rider, provided an early technical influence by writing me mathematical letters detailing, among other things, the properties of even and odd integers. I have been fortunate to frequently spend time with much of my extended family, especially during my college years on the East Coast, and I am deeply grateful for their presence in my life. More recently, it has been a pleasure to add my stepfather Bob Lee and his relatives to the family, as well as my brother-in-law, Grant Gavranovic. My sister Suzanne Rivoire, has been a life-long role model to whom I have enjoyed growing closer personally, professionally, and in physical proximity over my years at Stanford. My parents, Thomas Alexis Rivoire and Elizabeth Rivoire Lee, always encouraged and supported my academic interests without pushing me along any particular path. My mother has never minded even the most mundane tasks supporting these endeavors much less the more burdensome ones. My late father, despite his liberal arts background, somehow considered electrical engineering to be the best profession; no doubt he would have been proud to have two daughters with PhDs in EE from Stanford.

Contents

List of Tables

List of Figures

Chapter 1

Introduction

1.1 Motivation

Nonlinear optical frequency conversion is the basis of numerous photonic devices from green laser pointers to optical parametric oscillators. Since the first demonstration of second harmonic generation from a ruby crystal in 1961[3], on the heels of the development of the laser[4], the conventional view of nonlinear frequency conversion has involved high optical pump powers (often Watts), exotic materials such KDP and BBO that are disconnected from semiconductor electronics, and large crystals with dimensions of the order of millimeters to centimeters.

As the field of nanophotonics has emerged over the past decade, the boundary between semiconductor electronics and photonics has vastly diminished. In nonlinear optics, however, the divide remains. This thesis concerns the questions of how to perform nonlinear frequency conversion processes with materials, optical power levels, and device sizes amenable to on-chip semiconductor integration. Such integrated nonlinear optical frequency conversion devices could lead to miniaturized devices for applications such as on-chip spectroscopy and sensing of ultrasmall volumes of analyte from visible wavelengths to mid-infrared. Furthermore, emerging on-chip optical routing applications requiring nonlinear functionality are fundamentally incompatible with conventional nonlinear optics. Many of the optical elements such as beamsplitters and detectors that can be used for quantum optical computing have now been demonstrated on-chip[5], replacing an optical table's worth of carefully aligned components. One element that remains off-chip, however, has been a source of entangled photons coming from a nonlinear optical process. Classical optical information processing and routing could also benefit from on-chip nonlinear elements. Four-wave mixing[6] has been proposed as a way to enable frequency multiplexed on-chip sources; additionally, many computational and signal processing applications require nonlinear elements.

Dispersion engineered nanophotonic structures can simultaneously bring nonlinear frequency conversion on-chip and also robustly satisfy phase matching to achieve efficient devices. This thesis concerns the design, fabrication, characterization, and analysis of nanophotonic structures and semiconductor materials that can meet these requirements.

1.2 Contributions

The contributions in this dissertation include:

- The first photonic crystal cavities in gallium phosphide, which at the time of demonstration were the shortest wavelength photonic crystal cavities fabricated in a high (>3.0) refractive index material
- The demonstration of 430%/W (10^{-5} for 11 μW coupled power) continuous wave second harmonic generation in gallium phosphide photonic crystal cavities, an 8-orders of magnitude improvement on previous work in InP [7]
- The first demonstration of continuous wave sum-frequency generation in photonic crystal cavities, fabricated in GaP
- The first demonstration of second harmonic generation in photonic crystal waveguides, fabricated in GaP
- The demonstration of the fastest optically pumped single photon source, based on a quantum dot pumped by intracavity second harmonic generation from a telecom-wavelength laser

- The design, fabrication, and characterization of multiply resonant photonic crystal cavities with record frequency separation between resonances (more than 600 nm resonant wavelength separation measured experimentally)
- The first demonstration of lithographic techniques to align thin films of molecules to high-Q photonic crystal cavities
- Spectral and temporal characterization of InGaAs/GaP quantum dot luminescence, including the first observation of narrow spectral lines indicative of single quantum dots via the enhanced outcoupling of a photonic crystal cavity

1.3 Dissertation outline

Chapters 2 and 3 contain introductory material, with Chapter 2 providing background on second order nonlinear optical frequency conversion and Chapter 3 discussing thin membrane two dimensional photonic crystals.

Chapter 4 describes the design, fabrication, and characterization of the first GaP photonic crystal cavities, a crucial ingredient for the results in much of the later chapters of this dissertation. These results were published in Ref. [8], with Andrei Faraon as a collaborator.

Chapter 5 presents three experiments demonstrating three wave mixing in triangular lattice photonic crystal structures including second harmonic generation and sum frequency generation in linear three hole defect cavities, as well as second harmonic generation in W1 photonic crystal waveguides. These results were published in Refs. [9, 10, 11]. Ziliang Lin collaborated on cavity experiments and Sonia Buckley on waveguide experiments; the material for all three experiments was grown by Fariba Hatami with support from W. Ted Masselink.

Chapter 6 uses the frequency conversion techniques demonstrated in Chap. 5 to realize a fast (few hundred MHz) quantum dot single photon source triggered using intracavity second harmonic generation from a telecom-wavelength source. This work was a collaboration with Sonia Buckley and Arka Majumdar, with material provided by Hyochul Kim and Pierre Petroff and was published in Ref. [12].

Chapter 7 describes the design, fabrication and characterization of multiply resonant orthogonally crossed beam photonic crystal structures This work was a collaboration with Sonia Buckley and was published in Refs. [13, 14].

Chapter 8 presents specotroscopic measurements of two systems of visible quantum emitters: DNQDI molecules embedded in thin PMMA films and InGaAs/GaP quantum dots, coupled to GaP photonic crystal cavities. The work on molecules was performed jointly with Anika Kinkhabwala in collaboration with W.E. Moerner, with molecules provided by Yuri Avlasevich and Klaus Muellen and GaP material grown by Fariba Hatami with support from W. Ted Masselink; the principal results were published in Ref. [15]. Material for the InGaAs/GaP quantum dot spectroscopy, published in Ref. [16], was grown by Yuncheng Song with support from Minjoo Larry Lee.

Finally, Chapter 9 concludes the thesis and provides an outlook for future work in this field.

All work presented in this dissertation was performed under the supervision of Jelena Vučković.

Chapter 2

Nonlinear optical frequency conversion

The goal of frequency conversion is to change the frequency of the signal; at optical frequencies, this corresponds to changing the color of light. Such processes find applications in a diverse range of fields, including sensing, spectroscopy, metrology, communications, and quantum information. More specifically, the uses of optical frequency conversion include generation of light sources at frequencies otherwise inaccessible with available lasers, upconversion and downconversion of a fixed frequency signal (e.g. from an atom or semiconductor light emitter) to a more desirable frequency, and generation of entangled photon pairs via spontaneous parametric downconversion. This chapter introduces the basic physics for these processes; further details can be found in many references including [17, 18, 19], which this chapter follows in part.

2.1 Classical description of atomic polarization

Because the emission of photons at optical frequencies is based on electrons in atoms, which can be approximated classically as linear simple harmonic oscillators with quadratic potentials, optical frequency conversion cannot occur if the incident light is monochromatic and continuous wave (time-independent). The motion of an atomic electron of mass m and charge q with phenomenological damping constant γ and spring constant K driven by an electromagnetic field $\mathbf{E} = \mathbf{E_0}\cos(\omega t)$ can be modeled by the simple linear differential equation:

$$\frac{d^2\mathbf{r}}{dt^2} + \beta\frac{d\mathbf{r}}{dt} + \omega_0^2\mathbf{r} = \frac{q}{m}\mathbf{E_0}\cos(\omega t) \tag{2.1}$$

where $\beta = \gamma/m$ and $\omega_0 = \sqrt{K/m}$. This equation has steady-state solution

$$\mathbf{r}(t) = \frac{q/m}{\sqrt{\left(\omega^2 - \omega_0^2\right)^2 + \left(\beta\omega\right)^2}}\mathbf{E_0}\cos(\omega t + \delta) \tag{2.2}$$

where $\tan(\delta) = \frac{\omega^2 - \omega_0^2}{\beta\omega}$, producing a linear polarization $\mathbf{p} = q\mathbf{r} = \alpha\mathbf{E}$ where α is the polarizability. The total polarization will then be $\mathbf{P} = N\alpha\mathbf{E}$ where N is the atom density (number of atoms per unit volume). From this, it is clear that a linear combination of sinusoidal input signals (into which any other signal can be decomposed, via Fourier analysis) produces a linear superposition of sinusoidal outputs at the same frequencies. Accordingly, to perform frequency conversion requires either a time-dependent perturbation to the atom, or that we change our model to include a nonlinearity. In fact, a more accurate model does include such a nonlinearity due to the anharmonicity of the potential for the atomic electron at large values of electric field. The field at which this anharmonicity becomes significant can be estimated by assuming such a field would produce a displacement of the electron in the atom on the scale of the Bohr radius $a_0 = 4\pi\epsilon_0\hbar^2/me^2$, where ϵ_0 is the permittivity of free space, $\hbar$ is the reduced Planck's constant, m is the mass of the electron, and $-e$ is the charge on the electron. This results in an atomic electric field

$$E_{\text{at}} = \frac{e}{4\pi\epsilon_0 a_0^2} \tag{2.3}$$

giving $E = 5.14 \times 10^{11}$ V/m .

This anharmonicity adds quadratic and higher terms in $\mathbf{r}$ to Eqn. 2.2 (or cubic and higher terms in the potential), producing terms with new frequencies in the solution, starting with a frequency of 2ω for the lowest order nonlinearity. This results in the addition of nonlinear terms to the polarization,

$$\mathbf{p} = \alpha\mathbf{E} + \alpha_2\mathbf{E}^2 + \alpha_3\mathbf{E}^3... \tag{2.4}$$

For a crystal with a centrosymmetric structure, however, only higher order terms with even powers of $\mathbf{r}$ appear in the potential (or odd powers of $\mathbf{r}$ in the restoring force), that is:

$$\mathbf{p}_{\text{centrosymmetric}} = \alpha\mathbf{E} + \alpha_3\mathbf{E}^3... \tag{2.5}$$

2.2 Maxwell's equations-based description of nonlinear polarization

The nonlinear polarizaton can also be described macroscopically by Maxwell's Equations. For propagation of electromagnetic waves in a medium with no free charges or currents, the key equations are:

$$\nabla \times \mathbf{E} = -\frac{\partial \mathbf{B}}{dt} \tag{2.6a}$$

$$\nabla \times \mathbf{H} = \frac{\partial \mathbf{D}}{dt} \tag{2.6b}$$

where $\mathbf{B} = \mu_0\mathbf{H}$ for a nonmagnetic material where μ_0 is the permeability of free space, $\mathbf{D} = \epsilon_0\mathbf{E} + \mathbf{P} = \epsilon_0\epsilon E + P^{\text{NL}}$, ϵ_0 is the permittivity of free space and P^{NL} is the nonlinear polarization.

This leads to a driven wave equation

$$\nabla^2\mathbf{E} - \frac{\epsilon}{c^2}\frac{\partial^2\mathbf{E}}{\partial t^2} = \mu_0\frac{\partial^2\mathbf{P}^{\text{NL}}}{\partial t^2} \tag{2.7}$$

meaning that a nonlinear polarization will act as a source for a wave with the frequency contained in this nonlinear polarization. Returning to Eqn. 2.4, we can write the macroscopic nonlinear polarization

$$\mathbf{P} = \epsilon_0\chi^{(1)}\mathbf{E} + \epsilon_0\chi^{(2)}\mathbf{E}^2 + ... \tag{2.8}$$

where $1 + \chi^{(1)} = \epsilon$. For a monochromatic scalar input field $E(t) = E_0 \cos(\omega t)$, this leads to

$$P^{\rm NL}(t) = \epsilon_0 \chi^{(2)} E_0^2 \cos^2(\omega t) \tag{2.9}$$

Using the trigonometric identity $\cos(2x) = \frac{1+\cos^2(x)}{2}$, this then results in a term oscillating with frequency 2ω (as well as a constant term, which converts oscillating fields to DC and is known as optical rectification), which can act as a source in the wave equation 2.7. As this produces a term oscillating at twice the frequency of the original light, the process is known as second harmonic generation. Returning to Eqn. 2.3, this indicates displacements of the scale of the Bohr radius in the electron leading to optical nonlinearities could be produced by a nonlinear optical coefficient $\chi^{(2)} \approx 2$ pm/V.

Similarly, for two incident scalar fields with different frequencies ω_1 and ω_2, that is, $E_1(t) = E_{1,0}\cos(\omega_1 t)$ and $E_2(t) = E_{2,0}\cos(\omega_2 t)$, this produces additional terms in the nonlinear polarization with frequencies equal to the sum and difference of the two incident frequencies, $\omega_1 + \omega_2$ and $\omega_1 - \omega_2$:

$$\begin{aligned} P^{\rm NL}(t) &= \frac{\epsilon_0 \chi^{(2)}}{4} \left\{ E_{1,0}^2 e^{2i\omega_1 t} + E_{2,0}^2 e^{2i\omega_2 t} + \right. \\ &\quad 2\left[E_{1,0}E_{2,0} e^{i(\omega_1+\omega_2)t} + E_{1,0}E_{2,0}^* e^{i(\omega_1-\omega_2)t} \right] + \\ &\quad \left. 2\left[E_{1,0}E_{1,0}^* + E_{2,0}E_{2,0}^* \right] \right\} + c.c. \end{aligned} \tag{2.10}$$

where *c.c.* indicates the complex conjugate, the terms on the first line indicate second harmonic, terms on the second line indicate sum and difference frequency, and terms on the third line indicate optical rectification.

More generally, the second order suspectibility $\chi^{(2)}_{ijk}$ takes the form of a tensor, in this case third-rank, resulting in a 27-element matrix that depends on the polarizations of all three waves relative to the crystal structure. The number of elements in this tensor can be reduced to 18 by intrinsic permutation symmetry (arbitrary swapping of j and k), allowing the use of a contracted notation, resulting in:

$$\begin{bmatrix} P_1(\omega_1+\omega_2) \\ P_2(\omega_1+\omega_2) \\ P_3(\omega_1+\omega_2) \end{bmatrix} =$$

$$4\epsilon_0 \begin{bmatrix} d_{11} & d_{12} & d_{13} & d_{14} & d_{15} & d_{16} \\ d_{21} & d_{22} & d_{23} & d_{24} & d_{25} & d_{26} \\ d_{31} & d_{32} & d_{33} & d_{34} & d_{35} & d_{36} \end{bmatrix} \begin{bmatrix} E_X(\omega_1)E_X(\omega_2) \\ E_Y(\omega_1)E_Y(\omega_2) \\ E_Z(\omega_1)E_Z(\omega_2) \\ E_Y(\omega_1)E_Z(\omega_2) + E_Y(\omega_2)E_Z(\omega_1) \\ E_X(\omega_1)E_Z(\omega_2) + E_X(\omega_2)E_Z(\omega_1) \\ E_X(\omega_1)E_Y(\omega_2) + E_X(\omega_2)E_Y(\omega_1) \end{bmatrix} \tag{2.11}$$

For second harmonic generation, $\chi^{(2)} = 2d^{\mathrm{SHG}}$. The number of independent elements in the tensor can then be reduced to 10 unique elements with all 3 indices permuted (full permutation symmetry) when the process occurs far away from material resonances. The crystal structure and symmetries determines which of these 10 elements are non-zero.

Under certain approximations, such as the slowly varying envelope approximation (which allows the order of the differential equation to be reduced), this equation can be converted into coupled wave equations for each frequency for plane waves, focused beams, and several other common geometries. In certain regimes of operation, usually where the wave at one frequency is undepleted, simple solutions to these coupled wave equations exist. For example, for sum frequency generation with $\omega_3 = \omega_1 + \omega_2$, for waves propagating a distance L:

$$I_3 = \frac{8d_{\mathrm{eff}}^2\omega_3^2 I_1 I_2}{n_1 n_2 n_3 \epsilon_0 c^2} L^2 \mathrm{sinc}^2\left(\Delta k L/2\right) \tag{2.12}$$

where the d_{eff} is the nonlinearity determined by Eqn. 2.11, n is the refractive index. This relationship is illustrated in Figure 2.1.

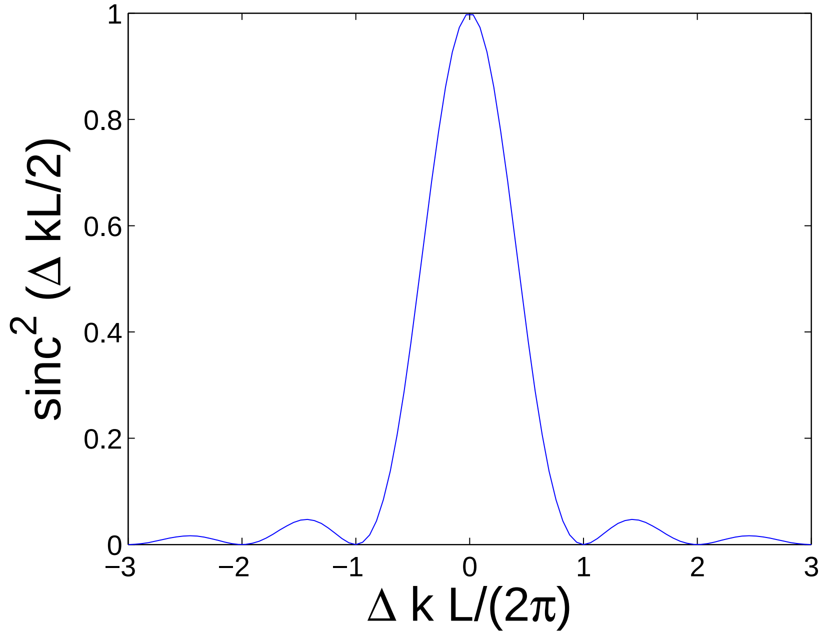

Figure 2.1: Reduction in sum-frequency signal over a distance L due to wavevector mismatch (as described in Eqn. 2.12).

2.3 Phase matching and materials for efficient frequency conversion

In order to generate new frequencies efficiently, two important constraints must be satisfied: (1) energy conservation and (2) momentum conservation, better known in this context as phase matching. Energy conservation stipulates that the frequency at which the nonlinear polarization is generated is the frequency radiated. Momentum conservation, or phase matching, means that to continue to add up coherently over long distances, the different frequencies must propagate at the same phase velocity; otherwise, the efficiency will be reduced. The phase velocity mismatch Δk can be written as $\Delta k = k_3 - k_2 - k_1$ for sum frequency or difference frequency generation and $\Delta k = k_2 - 2k_1$ for second harmonic generation. For second harmonic generation with monochromatic plane waves, $\Delta k = \frac{2\omega}{c}(n_{2\omega} - n_\omega)$, meaning that the indices of refraction at the two frequencies should be identical to minimize phase mismatch. In most materials, however, normal dispersion leads to a difference in the refractive indices at different frequencies.

In bulk materials, birefringence in materials such as $LiNbO_3$ and KDP can be used to satisfy phase matching, as beams at different frequencies can propagate along different crystal directions with different refractive indices. In practice, this requires careful control over the angle and frequently the temperature as well, as refractive indices are temperature dependent. For a birefringent material, the linear dielectric constant epsilon can be represented in a tensor form:

$$\epsilon = \begin{bmatrix} \epsilon_{XX} & 0 & 0 \\ 0 & \epsilon_{YY} & 0 \\ 0 & 0 & \epsilon_{ZZ} \end{bmatrix} \tag{2.13}$$

where ϵ_{XX}, ϵ_{YY}, and ϵ_{ZZ} can have different values, depending on the crystal structure, allowing phase matching to be satisfied.

When considering which materials to use for nonlinear optical frequency conversion, conventionally, large nonlinear optical coefficient, transparency at the frequencies of interest, and birefringence are the key parameters, with other properties such as high refractive index and large thermal conductivity also desirable. This typically results in a relatively exotic choice of materials for nonlinear optical frequency conversion that optimize these quantities of interest, but are difficult to integrate with semiconductor processing and electronics. These relevant properties for semiconductor materials, both Si and two III-V semiconductors, GaAs and GaP, and their comparison to the frequently used nonlinear optical material $LiNbO_3$ are shown below in Table 2.3.

We can observe that Si does not have a second order optical nonlinearity, due to the centrosymmetric nature of the crystal, making it a poor choice for second-order nonlinear optical processes. GaAs and GaP have large optical nonlinearities, broad transparency ranges (with GaP extending into the visible and GaAs far into the infrared), large thermal conductivity for reducing heat buildup, and large refractive index useful for confining light by total internal reflection. However, the zincblende

	Si	**GaAs**	**GaP**	**LiNbO$_3$**
d_{ij} (at 2 μm)	∼0	107	45	23
Transparency (μm)	1.1-5	0.9-17	0.5-11	0.4-4.5
Refractive index (at 1.5 μm)	3.5	3.4	3.1	2.1-2.2
Thermal conductivity (W/m K)	150	50	110	5
Birefringent	No	No	No	Yes

Table 2.1: Relevant parameters for nonlinear optical frequency conversion for semiconductors Si, GaAs, and GaP and traditional nonlinear optical material lithium niobate. $d = d_{14}$ for GaP, GaAs, $d = d_{33}$ for LiNbO$_3$. Low frequency side of absorption region determined by onset of two phonon absorption in the lattice. Values from Refs.[1, 2].

lattice of GaAs and GaP leads to an isotropic refractive index, meaning that phase matching cannot be accomplished via birefringence. Instead, phase matching can be achieved by structuring the material.

2.4 Phase matching in III-V semiconductors

The first methods introduced to support phase matching in III-V structures involved structuring the material on a macroscopic scale to periodically reverse the sign of the nonlinear optical coefficient every coherence length. This could be accomplished by gluing chunks of the material together (stack of plates approach), or more recently, by etching and regrowth of the material (known as orientation patterning[20, 21, 22]). Such methods are known as “quasi phase matching” and allow a continued increase in nonlinearly generated signal as the light propagates along a crystal.

An alternative approach is to structure the material on a smaller scale to change the dispersion relation, and accordingly the Δk. For example, for a second harmonic generation process, perfect phase matching could be accomplished with an arbitrary dispersion relation containing the two (k, ω) points (k_1, ω_1) and $(2k_1, 2\omega_1)$.

Several possible methods exist to engineer dispersion. A grating with periodicity a allows momentum to be converted in integer multiples of the reciprocal grating vectors $2\pi/a$; accordingly the maximum possible phase mismatch in such a structure would be set by the size of the first Brillouin zone. Nanoscale waveguides have also been designed to have anomalous dispersion[6], which can be engineered to cancel normal dispersion at a particular wavelength for a particular waveguide geometry.

Finally, it is also helpful to think of phase matching more generally as an overlap integral between the electric fields at different frequencies: in the case of planes waves, this leads to a product of $e^{ik_1\mathbf{r}}e^{ik_2\mathbf{r}}$, recovering the familiar Δk relation. For a nanoscale cavity structure, however, that exists in a region smaller than the coherence length and is not defined by a single k vector; this reduces to a spatial overlap of the electric fields, e.g. assuming all fields real, the overlap integral β for the three fields can be defined

$$\beta = \frac{\int_{\mathrm{NL}} dV E_1 E_2 E_3}{\sqrt{\int dV \epsilon |E_1|^2}\sqrt{\int dV \epsilon |E_2|^2}\sqrt{\int dV \epsilon |E_3|^2}} \tag{2.14}$$

so the electric fields are normalized by the energy and the numerator integral is taken only in the nonlinear material.

The radiated power at the sum or difference frequency generation will then be proportional to $|\epsilon_0\chi^{(2)}\beta|^2$. A nonlinear coupled mode theory approach including this overlap can be then used to model the frequency conversion process if the spatial form of all modes is known[23, 24, 25].

Note that such a field overlap also falls out naturally from a quantum mechanical description of three wave mixing, as the interaction Hamiltonian term comes from $P^{\mathrm{NL}} \cdot E$; the rate of any process is then proportional to the square of the relevant matrix elements, again resulting in a β^2 dependence. In this case, the total Hamiltonian can be written:

$$H = \hbar\omega_1 a_1^+ a_1 + \hbar\omega_2 a_2^+ a_2 + \hbar g \left(a_2 a_1^{+^2} + a_2^+ a_1^2 \right) \tag{2.15}$$

where the second term describes the nonlinear interaction and

$$g = \frac{\epsilon_0}{\hbar}\Sigma_{ijk} \int dV \chi_{ijk}^{(2)}(\mathbf{r}) E_1^i(\mathbf{r}) E_2^j(\mathbf{r}) E_3^k(\mathbf{r}) \tag{2.16}$$

where E is normalized to one photon per mode. In the limit $g > \kappa = \omega/(2Q)$, the second harmonic and first harmonic would experience Rabi oscillation [26].

In order to a define a quantity normalized to 1, it can also be useful to define a two-field overlap (this can be normalized as powers of electric field are the same in all integrals in numerator and denominator; this type of expression can be used to describe spatial overlap of two nanoscale modes, where the third frequency will have a classical form). In this case, we can introduce a modified form of β as γ[27], which will be used later in this thesis.

$$\gamma = \frac{\epsilon_{NL} \int_{\mathrm{NL}} dV E_1 E_2}{\sqrt{\int dV \epsilon |E_1|^2} \sqrt{\int dV \epsilon |E_2|^2}} \tag{2.17}$$

Chapter 3

Photonic crystal cavities

Optical components such as high reflectivity mirrors and ultrahigh-Q cavities have formed the cornerstone of many optical devices including lasers and other types of oscillators. Historically, these components have been machined on the macroscale. In the past decade, herculean efforts have been made to borrow the technology of semiconductor micro- and nanofabrication to dramatically reduce the size of optical components and facilitate their integration into on-chip devices. Planar photonic crystal cavities, the focus of this chapter, are an example of this technology, which provides a means to form high reflectivity micron-scale mirrors and nanoscale high-Q cavities. Other miniaturized technologies with different tradeoffs in quality of confinement compared to size of resonator also exist, including microdisks[28], microrings[29, 30], microspheres[31], etc. Many of these technologies confine light in all three dimensions by total internal reflection by forming the nanophotonic structure inside a higher refractive index than the surrounding medium. Here, we discuss photonic crystal technologies, which use distributed Bragg reflection for confinement in at least one dimension.

3.1 Distributed Bragg reflection

If we consider the interface between two materials with different refractive indices, we can calculate the reflection and transmission for light impinging on the interface. For a single interface at normal incidence, this leads to an intensity reflection coefficient $R = |\frac{n_2 - n_1}{n_2 + n_1}|^2$ where n_1 and n_2 are the refractive indices of the two materials. If we then stack a set of these interfaces, we must consider how the phases of the reflected light at successive surfaces add up. In general, by carefully choosing the thicknesses and refractive indices of the two materials, the phases of the reflected light can interfere constructively leading to greater reflection, or destructivity leading to reduced reflection. This principle, known as distributed Bragg reflection (DBR), provides a straightforward method for creating very high reflectivity or low reflectivity mirrors with a geometry that is simple to understand. A one-dimensional DBR, also known as a Bragg stack, is shown in Fig. 3.1. In one dimension, at normal incidence, very high reflectivity can be achieved by choosing the thicknesses of the materials to be equal to a quarter of the optical wavelength in the material, $\frac{\lambda}{4n}$. The reflectivity of the such a structure will increase as the number of periods and can have bandwidth of a few hundred nanometers. The dielectric constant for the one dimensionally periodic structure can be simply described if the dielectric constant for a single period is known: $\epsilon(y) = \epsilon(y + a)$. Such a structure can also be described not only by the periodicity in real space, but also by the periodicity in the Fourier domain, or the k-space vectors that can be used to create the perfectly periodic lattice. The 1D Bragg stack in Fig. 3.1 could be described by the reciprocal lattice vector $k_y = 2\pi/a$ where a is the periodicity.

3.2 Planar photonic crystal cavities

This periodic tiling of refractive index and principle of distributed Bragg reflection can also be implemented in multiple dimensions. To facilitate fabrication, it is helpul to use planar structures, resulting in distributed Bragg reflection in at most two dimensions. Many 2D periodic tilings in space exist; for photonic crystals, the most commonly used have been the square lattice and triangular lattice. A triangular lattice 2D photonic crystal is shown in Fig. 3.2. In this structure, for proper choice of hole size and periodicity, the structure can realize distributed Bragg reflection for all in-plane wavevectors over a broad range of frequencies; total internal reflection can

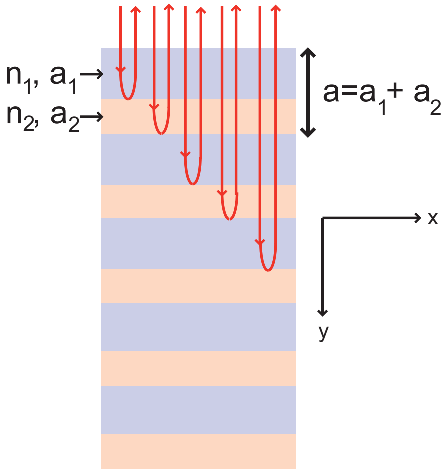

Figure 3.1: One-dimensional photonic crystal with periodicity a and two planar materials per period (pink and purple) with different refractive indices. For correct choice of thickness and refractive index in each period, reflections summed over all interfaces add coherently to produce very high reflection.

confine light to the slab in the out of plane direction.

The exact dispersion relation between wavevector and frequency can be found by solving Maxwell's equations for the structure. In practice, this is frequently done by discretizing Maxwell's equations and solving within a single unit cell, while applying periodic boundary conditions to represent the infinitely tiled structure. One popular approach is a finite difference frequency domain simulation, where Maxwell's equations are cast into the Hermitian eigenvalue form[32]

$$\nabla \times \frac{1}{\epsilon} \nabla \times \mathbf{H} = \frac{\omega^2}{c^2} \mathbf{H} \tag{3.1}$$

A second approach is known as finite difference time domain simulation, where an initial current source, dipole source, or field pattern is allowed to evolve in time according to Maxwell's equations; resonant modes are found by taking the Fourier transform of the time-evolved electromagnetic fields. The result of such a simulation is shown in Fig. 3.3. The white region indicates the area confined to the slab by total internal reflection; the gray region indicates modes in this area can couple to free space. The lowest frequency band of solutions is known as the "dielectric band", as

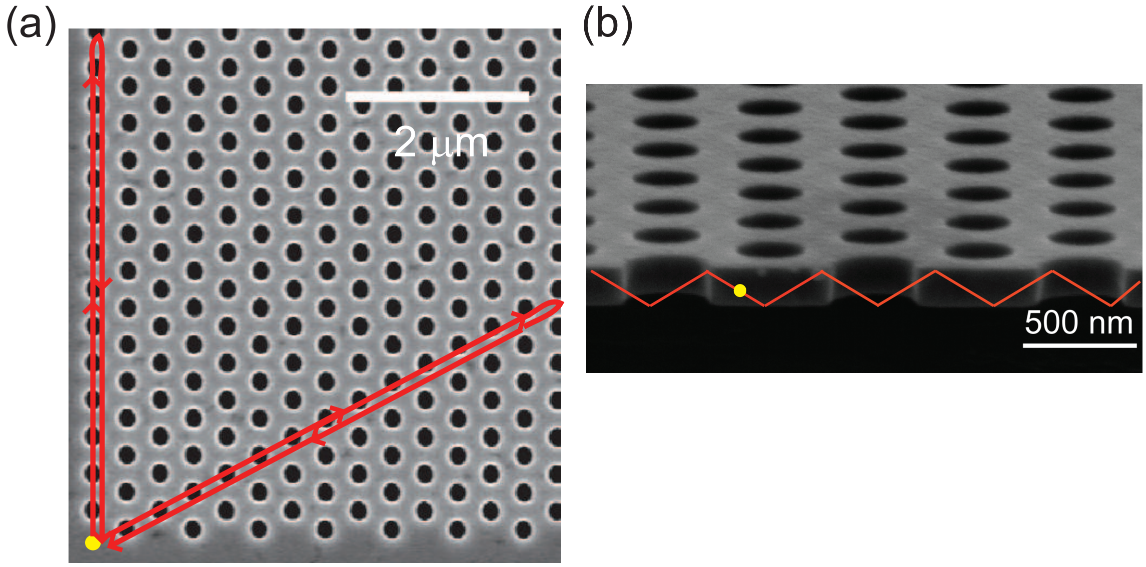

Figure 3.2: (a) Two dimensional distributed Bragg reflection in a triangular photonic crystal lattice of air holes in a high refractive index slab. Light is strongly reflected by the photonic crystal for all directions in the plane of the slab. (b) Light is confined inside the slab by total internal reflection between the high refractive index slab and surrounding low-index air.

electric field is concentrated in the higher dielectric constant material for these modes. At higher frequencies, there are additional bands of solutions, the first of which has electric field primarily concentrated in air, and is known as “air band”; higher bands have solutions orthogonal to the dielectric and air bands. In the frequencies between the dielectric and air band, there are no solutions to Maxwell’s equations; this region serves as a ”photonic band gap” preventing light from propagating inside the crystal.

3.3 Photonic crystal cavities

By making a small perturbation to the perfectly periodic photonic crystal, it is possible to create defects that can locally change the frequency of a mode and pull it into the band gap (similar to doping impurities into the electronic band structure of semiconductors). For a small increase in the size of a single hole (“acceptor” cavity), the frequency of the dielectric band is locally increased, forming a defect mode inside the band gap that cannot propagate through the crystal. On the other hand, decreasing the size of or eliminating a single hole locally decreases the frequency of the electromagnetic mode, pulling a mode down from the air band into the gap ("donor" cavity). In this way, it is possible to form localized cavities that can have high quality factor while approaching the small-volume limit of a dielectric cavity ($(\lambda/(2n))^3$).

In the first chapters of this thesis, we will use a donor-type cavity design, where three consecutive holes in a single row are removed (also known as the linear three hole defect or L3 cavity, developed by Susumu Noda's group[33]), and the adjacent holes are slightly shifted to increase the Q (which can be thought of as adjusting the boundaries of the cavity to match the phase[34]). The dielectric constant for the cavity and local electromagnetic field intensity localized by the mode are shown in Fig. 3.4.

It is also possible to form planar photonic crystals and cavities using distributed Bragg reflection in one dimensional and total internal reflection in two dimensions, for example, by forming a narrow beam with holes[35]; the central region of the beam can then be locally perturbed to form a cavity, as shown in Fig. 3.5.

3.4 Figures of merit for photonic crystal cavities

3.4.1 Quality factor

The measure of the quality of the optical cavity resonance, $Q = \frac{\omega W}{P}$, is proportional to the ratio of energy stored in the cavity W to the power radiated by the cavity P. The Q can also be written in terms of the photon lifetime τ_{ph}, which can be thought of as the amount of time the photon spends in the cavity before it leaks out, where $Q = \omega\tau_{ph}$. Experimentally, it is often more practical to measure the spectrum to find the Q, rather than the lifetime; this can neatly be expressed by rewriting $Q = \frac{\omega}{\Delta\omega} = \frac{\lambda}{\delta\lambda}$. Therefore,

$$Q = \frac{\omega W}{P} = \omega\tau_{ph} = \frac{\omega}{\Delta\omega} = \frac{\lambda}{\delta\lambda} \tag{3.2}$$

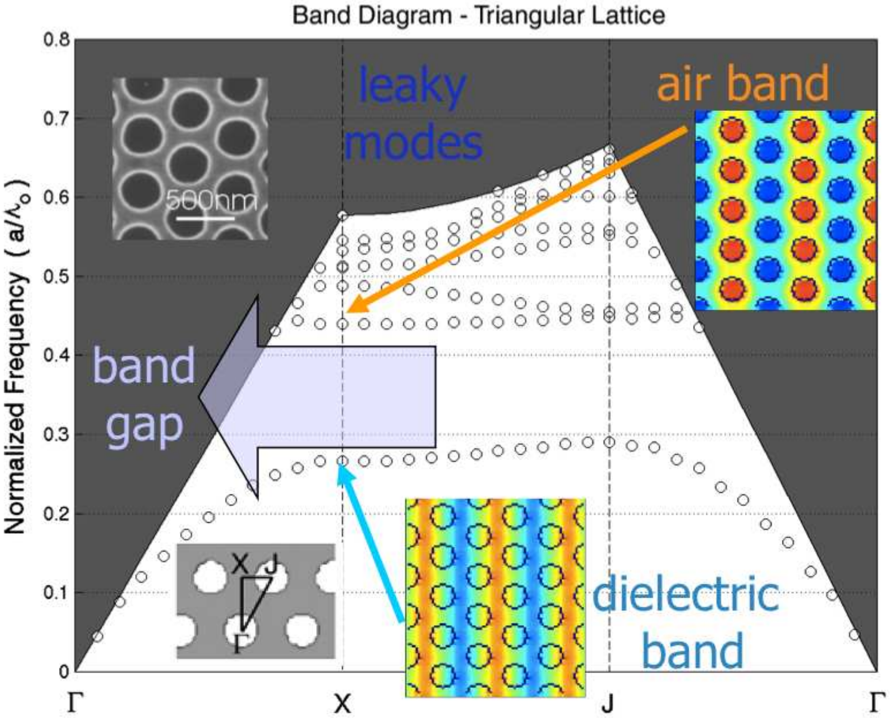

Figure 3.3: Solutions to Maxwell's Equations (black circles) for light polarized in the plane of the slab in the infinite triangular photonic crystal lattice (scanning electron microscope (SEM) of fabricated structure shown in top left). Lowest frequency set of solutions forms the dielectric band; next higher frequency set of solutions forms the air band (electric fields are plotted at the X point). Between the frequencies of the dielectric band and air band, there are no guided modes in the slab. Boundary between gray and white regions indicates the light line. Image courtesy of Jelena Vučković.

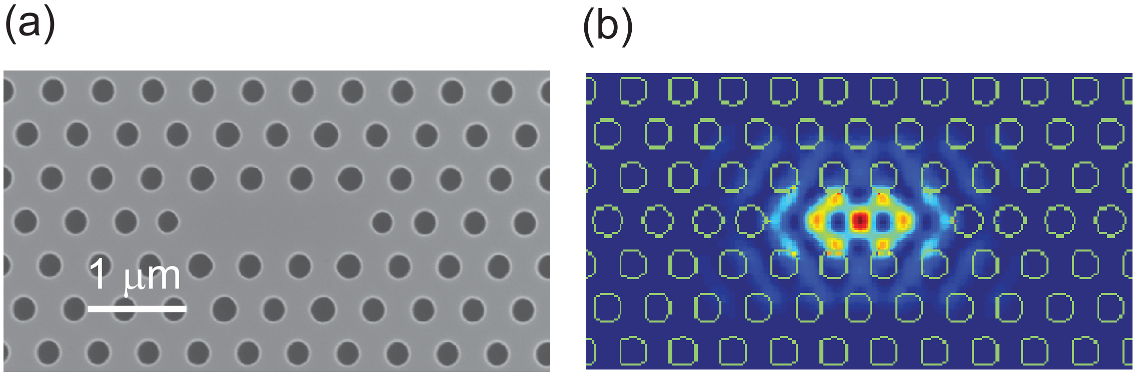

Figure 3.4: (a) SEM image of an L3 cavity. (b) Local electric field intensity inside the cavity at the resonant frequency.

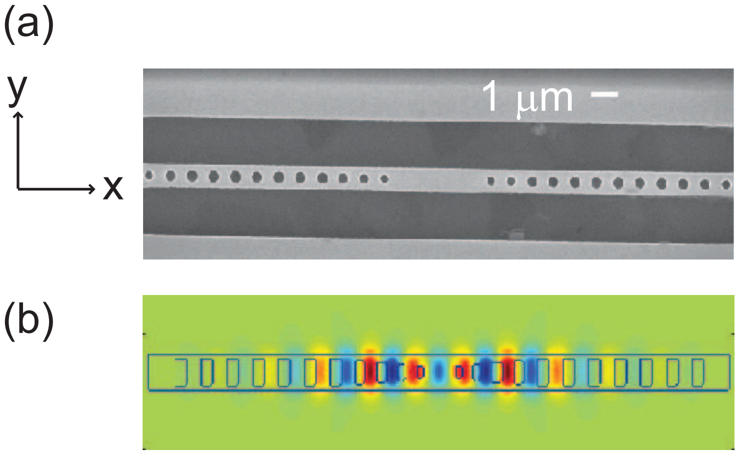

Figure 3.5: (a) SEM image of an nanobeam cavity. (b) E_y inside the beam cavity.

The quality factor of the L3 cavity for index contrast of 3.5:1 (e.g. semiconductor:air) is approximately 50,000. Higher quality factor designs using smaller critical dimensions can also be engineered[36, 37]. The nanobeam cavity can also be designed to yield Q of more than 1 million[38, 39].

3.4.2 Mode volume

The mode volume can be defined as the physical space over which the mode would extend if the energy was uniformly distributed, or alternatively:

$$V_{\text{mode}} = \frac{\int \epsilon(\mathbf{r})|\mathbf{E}(\mathbf{r})|^{\mathbf{2}}}{\max\left[\epsilon(\mathbf{r})|\mathbf{E}(\mathbf{r})|^{\mathbf{2}}\right]} \tag{3.3}$$

This L3 cavity and nanobeam cavity both have mode volume on the order of $(\lambda/n)^3$.

3.4.3 Nonlinear frequency conversion

In general, higher quality factor cavities are desirable for maximizing the photon storage time and enhancing the interaction between light and the material forming the cavity. Higher Q however, does ultimately limit the speed of any cavity-based device, as well as the bandwidth of pulses that can be coupled into the cavity, so an ultrahigh-Q is not always desirable. The strongest interaction will also be obtained for smallest mode volumes, as the concentration of light is enhanced.

For each field in nonlinear three-wave mixing, there will be an enhancement of the nonlinear optical interaction proportional to the quality factor of the mode at that frequency. That is, for second harmonic generation at $\omega_2 = 2\omega_1$, there would be a $Q_1^2 Q_2$ enhancement; for sum-frequency generation the enhancement would be proportional to $Q_1 Q_2 Q_3$. A smaller mode volume will also enhance the nonlinear optical interaction. As the electromagnetic field strength is proportional to $1/\sqrt{V_{\text{mode}}}$, the electromagnetic energy concentration will be enhanced by a factor related to $1/V_{\text{mode}}$. However, this enhancement will only be realized if the spatial mode profiles of the electromagnetic field are identical (as described by γ and β in Chap. 2); alternatively, an effective mode volume can be defined[40].

Chapter 4

GaP photonic crystal cavities

4.1 Motivation

As described in Chap. 3, photonic crystal nanocavities confine light in ultrasmall volumes, making them ideal for low-power, on-chip optoelectronic devices[41, 42, 43] as well as for exploring fundamental light-matter interactions[44, 45]. Most experimental work in photonic crystal cavities has been done in telecom bands[45]. This has been facilitated by well established fabrication procedures for semiconductors such as silicon and gallium arsenide, which have band gaps in the infrared. Photonic crystal devices operating (via linear or nonlinear processes) in the visible part of the spectrum, however, could serve as light sources and spectroscopic devices operating below 750 nm. Additionally, for devices operating at higher optical powers, such as nonlinear optical processes where the desired output is superlinearly dependent on incident power, a material with an electronic band gap in the visible minimizes two photon absorption of telecom wavelength inputs. Furthermore, photonic crystal cavities with resonances in the visible could also be coupled to novel light emitters such as nitrogen vacancy centers[46, 47], fluorescent molecules[48], and visible colloidal quantum dots[49].

To date, most photonic crystal devices operating in the visible have been fabricated in one of three material systems: gallium nitride, silicon nitride, and AlGaInP. While devices with wavelengths as short as blue can be fabricated in gallium nitride[50, 51], fabrication processes in this system are difficult, and the low refractive index of gallium nitride (n=2.4) limits the device quality factors[52]. Low refractive index is also a drawback of the silicon nitride system[53, 54], as is the lack of a second-order optical nonlinear coefficient. Two groups have fabricated AlGaInP-based photonic crystals in the red[55, 56] with InGaP quantum wells. This system, however, requires precise control over the fraction of each material in the quaternary system to obtain the proper band gap and lattice constant, and is lattice matched to a GaAs substrate, which is absorbing in the visible.

In this chapter, we show that photonic crystal devices at visible wavelengths, which could be used as linear and nonlinear optical light sources, can be fabricated in gallium phosphide. Gallium phosphide is a high refractive index (n=3.25 at 700 nm, n=3.44 at 555 nm at room temperature[57]) III-V semiconductor with an indirect band gap at 555 nm at room temperature. Although gallium phosphide is not typically used for devices requiring very high brightness because of its indirect band gap, incorporating InP quantum dots or quantum wells [58], or colloidal quantum dots should greatly increase the quantum efficiency. Additionally, gallium phosphide has a relatively high thermal conductivity (see Chap. 2) and a low surface recombination rate, estimated to be roughly an order of magnitude less than that of gallium arsenide[59] because of its high phosphorus content, which has a passivating effect[60]. Surface recombination is particularly important for photonic crystal devices because of the additional exposed surface area from etched air holes.

4.2 Cavity design and fabrication

Linear three hole defect (L3)[33] cavities were first simulated and then fabricated in a 140 nm thick GaP membrane (Fig. 4.1). Simulation results indicate that quality factors above 10,000 can be obtained for this type of cavity (three holes removed, holes next to cavity displaced outward by $0.15a$) using a triangular lattice of lattice constant a with slab thickness d/a=0.55 and hole radius r/a=0.3 with no other design modifications. The electric field profile for the fundamental L3 cavity mode is shown in Fig. 4.1b.

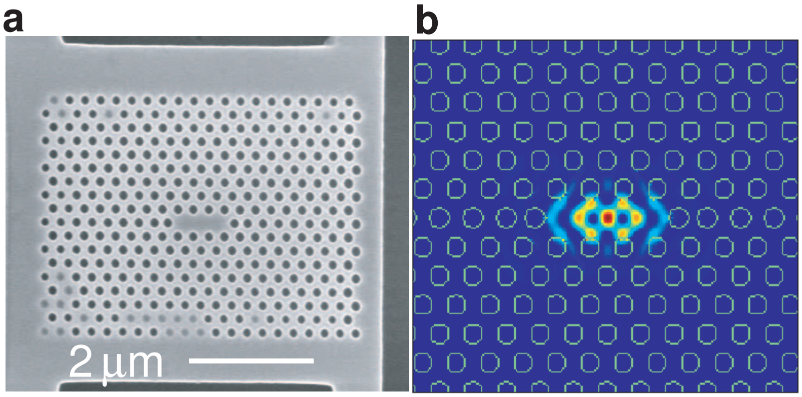

Figure 4.1: (a) Scanning electron microscope image of a fabricated GaP photonic crystal membrane after undercut of sacrificial layer with lattice constant a=246 nm, hole radius, r/a=0.32, slab thickness d/a=0.57. (b) Finite difference time domain simulation of electric field intensity inside the cavity for the high Q mode.

To fabricate these structures, the 140 nm thick GaP membrane was grown on the top of a 1 μm thick sacrificial $\mathrm{Al_xGa_{1-x}P}$ layer. Patterns were first defined in ZEP520A resist by electron-beam lithography and then transferred into the GaP membrane by a chlorine-based reactive ion etch. The recipe used was similar to the one listed in Appendix A. To calibrate the dry etch rate of small features in GaP, trenches of various widths were etched and then cleaved and measured in a scanning electron microscope (SEM), as shown in Fig. 4.2. As evidenced in the SEM images, smaller features have less vertical etching profiles. Excess photoresist was removed with oxygen plasma, and the sacrificial layer was undercut with hydrofluoric acid to yield suspended membrane structures with high index contrast. For this value of aluminum content (x=0.6) in AlGaP, the selectivity of the wet etch was insufficient to remove the sacrificial AlGaP layer without some effect on the GaP membrane as well. Scanning electron microscope images of one of the fabricated membranes can be seen in Fig. 4.1; in this case, wet etch time is minimized so the effect on GaP photonic crystal is not readily visible. For other samples fabricated with slightly longer wet etch times, the circular photonic crystal holes etch to squares along the crystallographic directions of the GaP, as shown in Fig. 4.2. High aluminum content

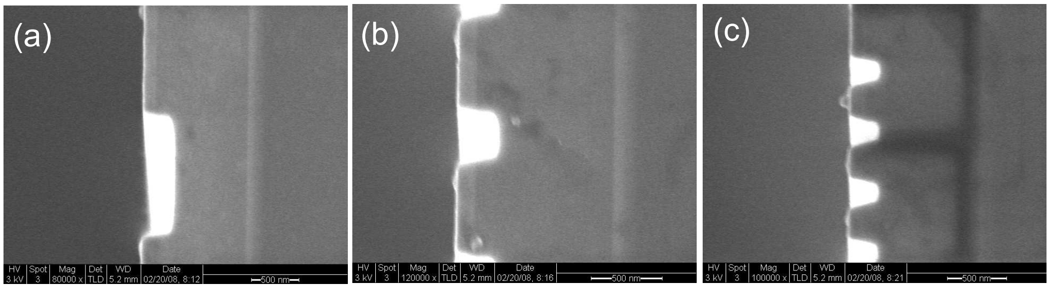

Figure 4.2: (a) Scanning electron microscope image of a 1 μm-wide trench etched in GaP. (b) SEM of 200 nm-wide trenches. (c) SEM of 100 nm-wide trenches.

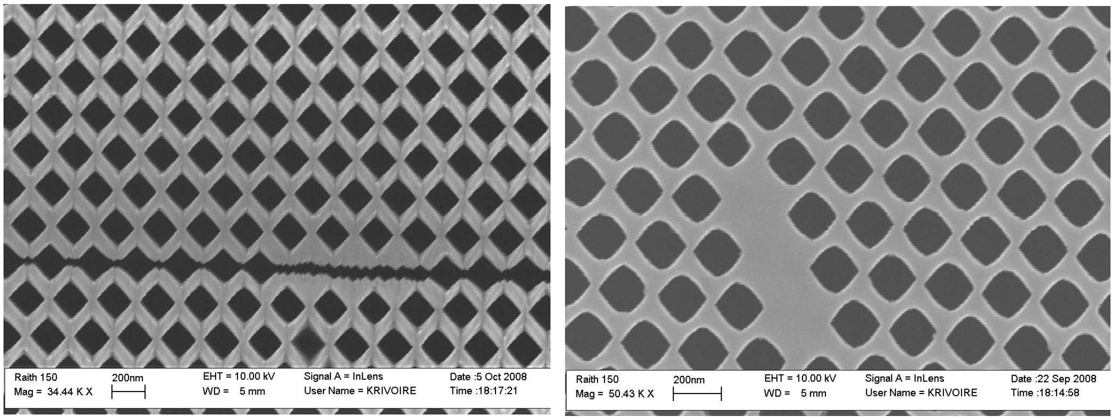

Figure 4.3: SEM images of chips undercut a sufficient amount of time to also etch GaP membrane photonic crystal holes, transforming circular photonic crystal holes into squares.

(x>0.8) was subsequently found to eliminate this problem by increasing the selectivity of the undercut.

4.3 Reflectivity measurement of cavity resonances

The fabricated photonic crystal resonators were probed using a confocal cross-polarized reflectivity measurement[61, 62] technique as depicted in Fig. 4.4a. This technique uses polarization control to achieve a high signal-to-noise ratio and allows probing of cavities with no internal light source. A vertically polarized (V) probe is directed

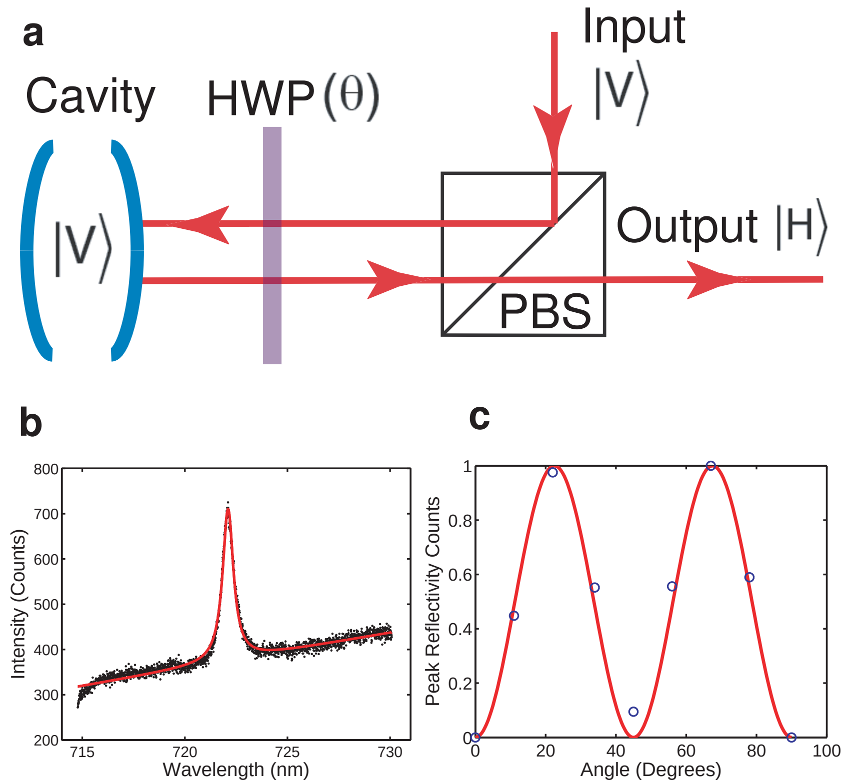

Figure 4.4: (a) Experimental setup. The V-polarized cavity is probed in a cross-polarized setup using a PBS and a HWP. The cavity signal observed at the output follows a sin(4θ) dependence where theta is the HWP setting (θ=0 corresponds to V polarization). (b) Spectrum of a cavity measured with configuration of Fig. 4.4(a) with HWP at $\theta = 67°$. The cavity resonance is at 722 nm at room temperature. A fit to a Lorentzian (solid line) gives Q=1100. (d) (Circles) Normalized counts in cavity peak as a function of HWP angle (background subtracted). (Line) Fit with sin(4θ).

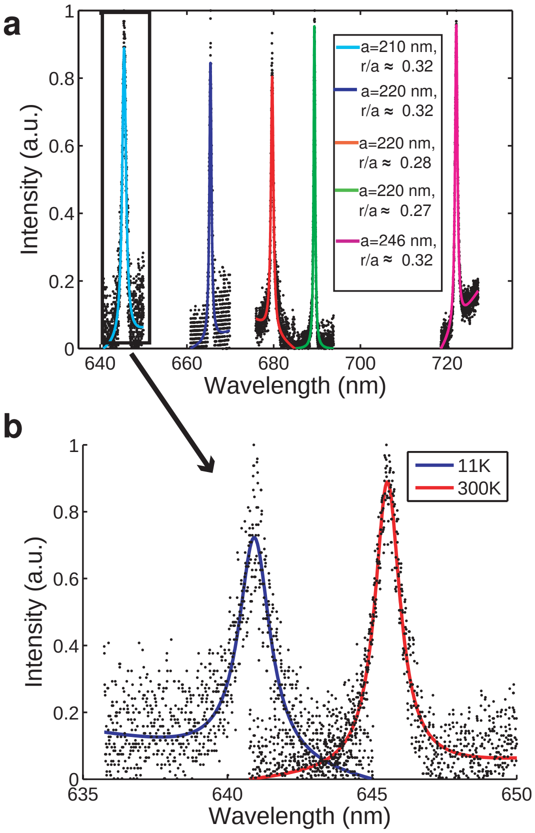

Figure 4.5: (a) Shift of photonic crystal resonance at room temperature as a and r/a are changed. Solid lines are fits to Lorentzians. (b) Cavity resonance measured at room temperature (blue) and low temperature (red). Solid lines indicate fits to Lorentzians.

through a polarizing beam splitter (PBS) and a half wave plate (HWP) onto the photonic crystal cavity, which has a mode that is also vertically polarized (V). The reflected output is observed through the PBS, which acts as a horizontal (H) polarizer. The primary polarization of the cavity mode is vertical (V). When the angle between the HWP fast axis and the vertical direction (θ) is set to zero, the cavity coupled light is reflected with V-polarization and does not transmit through the beamsplitter. Rotation of the HWP allows part of the cavity-coupled light to be transmitted at the PBS into the output port with intensity following a $\sin(4\theta)$ dependence (Fig. 4.4(b,c)). A tungsten halogen lamp source was used as a wide broadband signal at the input. The output field was measured using a spectrometer with a liquid nitrogen cooled CCD.

To fabricate cavities with resonant wavelengths spanning a large interval, lattice constant a (210 nm$<a<$246 nm) and hole radius (0.25$<r/a<$0.35) were modified. These changes in the fabrication parameters resulted in cavities with resonance wavelength spanning from 645 nm to 750 nm as shown in Fig. 4.5. (Plots in Fig. 4.5 are shown with background subtracted.) The measured resonances have shorter wavelengths than predicted from finite difference time domain simulations (by about $0.05a/\lambda$). We believe this difference is a result of imperfect selectivity between the sacrificial layer and membrane during the wet etch step, which reduces the membrane thickness. Quality factors measured experimentally are between 500 and 1700. This is about one order of magnitude smaller than predicted by simulations because of imperfections introduced in the fabrication process.

The shortest resonant cavity wavelength observed at room temperature was 645 nm with quality factor 610. The resonance wavelength depends on the temperature-dependent refractive index of the membrane. To shift the cavity resonance to lower wavelengths, the sample was cooled to 11K in a continuous flow liquid helium cryostat. The change in temperature caused the resonance to shift from 645 nm to 641 nm (in the red wavelenth range) and the quality factor to decrease to 490 as shown in Fig. 4.5. With improved fabrication, devices operating close the 555 nm band gap of gallium phosphide could be made; such devices could be used as green LEDs and lasers in combination with embedded light emitters at these wavelengths. Quality factors could also be improved by using modified designs with simulated Q values more than a order of magnitude higher[63]. However, these Qs can still enable a significant Purcell effect, up to 185, as mode volume is only $0.7(\lambda/n)^3$.

4.4 Conclusions

In summary, in this chapter, we demonstrate a new GaP-based materials system for photonic crystals in the visible. We probe linear three-hole defect cavities in reflectivity and observe resonances from 645 nm to 750 nm at room temperature with quality factors as high as 1700. To our knowledge, these are the shortest wavelength photonic crystal cavities fabricated in a high-index material.

We expect this materials system to allow access to a new range of photonic crystal devices in the visible, including LEDs and lasers. Additionally, the gallium phosphide system will provide opportunities to couple photonic crystal cavities to emitters in the visible such as colloidal quantum dots, nitrogen vacancy centers, biomolecules, or organic molecules.

Chapter 5

Three wave mixing in GaP photonic crystals

This chapter presents three experiments in three wave mixing using GaP photonic crystals. In the first, we demonstrate record efficiency second harmonic generation using photonic crystal cavities; we then employ a similar approach to demonstrate sum-frequency generation. Finally, we demonstrate a broadband enhancement of second harmonic generation by using a photonic crystal waveguide.

5.1 Motivation

III-V semiconductors such as GaAs and GaP are considered promising candidates for nonlinear optical devices [22, 21, 64] because of their large second order nonlinearity [65], transparency over a wide wavelength range (870 nm-17 μm for GaAs and 550 nm-11 μm for GaP), and ease of integration with semiconductor processing. The cubic symmetry of the zincblende lattice of III-V semiconductors, however, does not exhibit birefringence, so achieving phase matching of the two different frequencies typically requires employing quasi-phase matching techniques or an additional birefringent material [20, 66, 67, 68]. In addition to the challenges posed by phase matching, nonlinear optical devices are also constrained by the bulky, macroscopic resonant cavities typically used to enhance conversion efficiency and reduce the required input power[69]. High quality factor microcavities have the potential to achieve similar conversion efficiencies with a vastly reduced size, and could be integrated with nanophotonic technology. In these microcavities, the phase matching condition is satisfied by the spatial overlap between the fundamental and second harmonic field patterns [24, 70, 71]. Experimentally, this resonant enhancement has been demonstrated in silica microdisks [72], where green third harmonic radiation was observable with hundreds of microwatts incident continuous wave IR power. Enhanced second harmonic generation in photonic crystal cavities [7] and third harmonic generation in photonic crystal waveguides [73] have also been demonstrated. However, these experiments suffered from poor conversion efficiency, in part because the second harmonic was above the band gap of the employed semiconductor and therefore strongly absorbed in it (where efficiency is defined as the ratio of the output second harmonic to the coupled input power at 1550 nm, third harmonic $P_{\text{out}}/P_{\text{in,coupled}} = 5 \times 10^{-10}$ for peak $P_{\text{in}} = 1W$ [73]; second harmonic $P_{\text{out}}/P_{\text{in}} = 10^{-13}$ for CW $P_{\text{in}} = 300\ \mu\text{W}$ [7]).

5.2 Second harmonic generation in GaP photonic crystal cavities

In this section, we show that photonic crystal nanocavities resonant with the pump wavelength can be used to generate second harmonic radiation with input power orders of magnitude smaller than previously demonstrated.

5.2.1 Experimental setup and fabrication of cavities

The experiment is described in Fig. 5.1(a). Our resonator is a modified linear three hole defect photonic crystal cavity [33]. A scanning electron microscope (SEM) image is shown in Fig. 5.1(b). A tunable infrared laser (Agilent 81680A) with wavelength range around 1500 nm at normal incidence is spatially aligned to the cavity location and spectrally aligned to the cavity resonance; the laser polarization is also aligned to

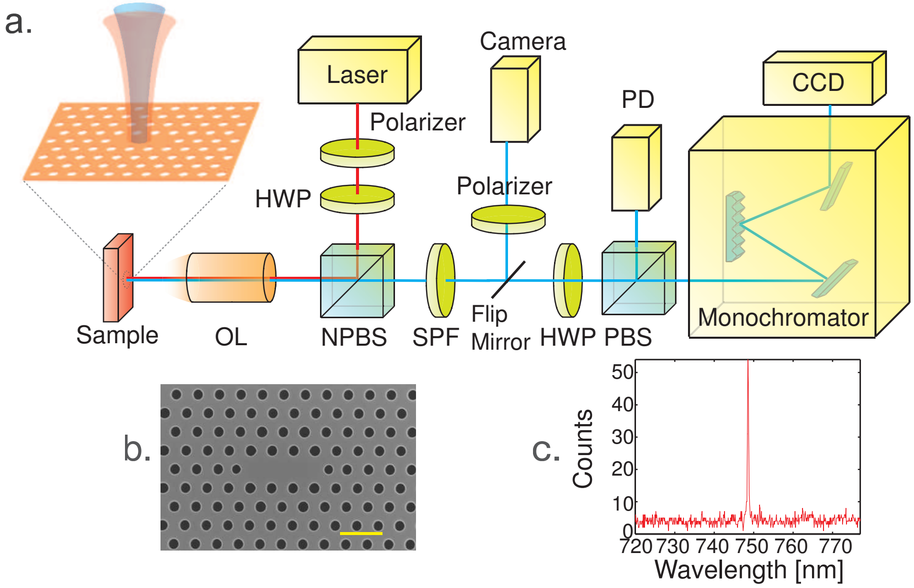

Figure 5.1: (a) Microscope-based setup for second harmonic generation. HWP: half wave plate, NPBS: nonpolarizing beamsplitter, OL: objective lens, PBS: polarizing beamsplitter, SPF: short pass filter, PD: photodiode. The incident light traces the red line into the cavity sample. The second harmonic light follows the blue line into the spectrometer, photodiode, or camera. The polarization of the incident light is controlled by the polarizer and HWP; the polarization of the second harmonic radiation is measured using HWP and PBS. (b) SEM image of a fabricated structure. Scale bar indicates 1 μm. (c) Spectrum of generated second harmonic light with 8 nW power at 1497.4 nm coupled to the cavity (160 nW incident).

match that of the cavity mode. In this configuration, enhanced second harmonic radiation is generated; this radiation is either analyzed by a spectrometer, measured by a femto-Watt photodetector, or imaged onto a camera. A second harmonic spectrum with 8 nW power coupled to the cavity (160 nW incident on the sample) is shown in Fig. 5.1(c). The electronic band gap of GaP minimizes both absorption of the harmonic radiation at 750 nm and two photon absorption at the fundamental wavelength 1500 nm. The samples were grown by gas-source molecular beam epitaxy on a (100)-oriented GaP wafer. A 160 nm thick GaP membrane was grown on the top of a 1 μm thick sacrificial AlGaP layer. Structures were fabricated with e-beam lithography and etching, as described in [8]. The photonic crystal cavities are three hole linear defects [33] with lattice constant a=500-560 nm, hole radius $r/a \approx 0.2-0.25$, and slab thickness $d/a \approx 0.3$. We use a perturbation design for our photonic crystal cavities [74] to increase the coupling efficiency between the cavity and objective lens.

5.2.2 Simulation of second harmonic inside photonic crystal cavities

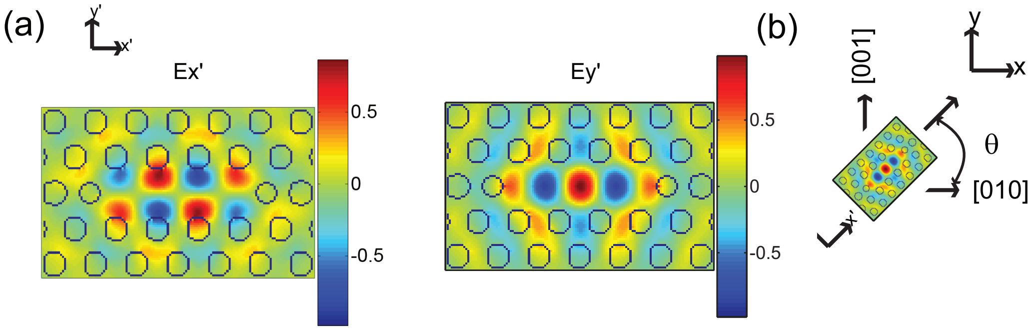

Figure 5.2: (a) Finite difference time domain (FDTD) simulation of electric field inside the cavity for the fundamental TE-like cavity resonance in the center of the slab. Cavity field axes are E'_x and E'_y (b) Illustration of orientation of cavity relative to crystal axes. Cavities axes E'_x, E'_y are rotated from crystal axes E_x, E_y by an angle θ. Fields along crystal axes are determined by projection.

To efficiently radiate power at the second harmonic, the field patterns at the fundamental and second harmonic frequency must have constructive overlap. In our experiment, the fundamental frequency is set to that of the cavity mode, which dictates the field pattern at this frequency. The second harmonic frequency is matched to a higher order photonic band edge mode, which determines the second harmonic field pattern. We simulate the field patterns inside the structure at the fundamental and second harmonic wavelengths using 3D finite difference time domain methods. The in-plane electric field profile in the center of the slab for the fundamental transverse electric-like (TE-like) cavity mode is shown in Fig. 5.2(a). In the far-field, this cavity radiates primarily with $\hat{y}'$ polarization, and therefore incident light with this polarization can couple into the cavity. GaP has a noncentrosymmetric cubic crystal

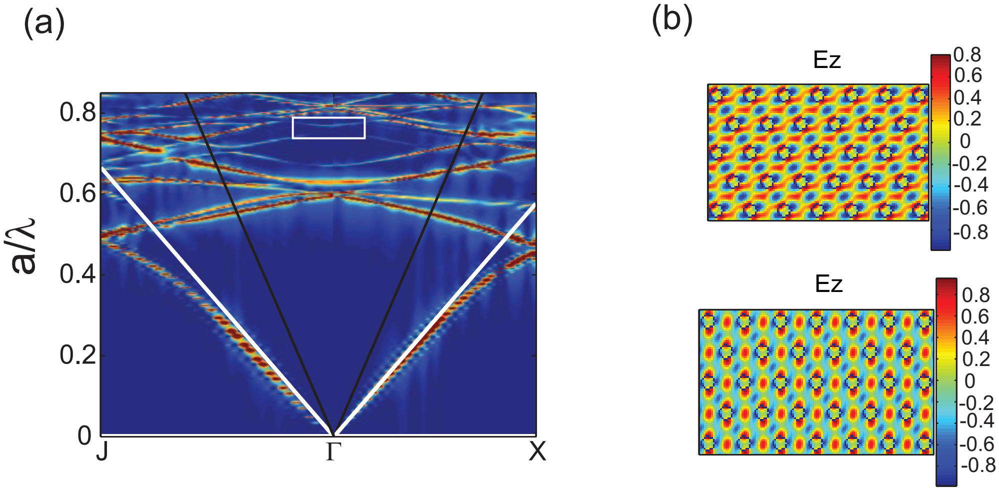

Figure 5.3: (a) FDTD simulation of TM-like photonic bands for the same triangular lattice photonic crystal. Red indicates band positions. White solid lines indicate light line; black solid lines indicate numerical aperture of lens. White box indicates mode at second harmonic frequency. a: lattice constant of photonic crystal. (b) E_z field patterns of degenerate TM-like mode at second harmonic frequency at the Γ point.

structure; the only non-zero elements of the bulk $\chi^{(2)}_{ijk}$ have $i \neq j \neq k$. Since the input signal in our experiment couples to the TE-like photonic crystal cavity mode [with dominant E'_x and E'_y in-plane field components defined in Figs. 5.2(a), 5.2(b)], the output second harmonic signal will then be primarily $\hat{z}$-polarized, i.e., transverse magnetic-like (TM-like) mode. The bulk second harmonic nonlinear polarization generated takes the form $P^{(2)}_z = 2\epsilon_0 d_{14} E_x E_y$ where x, y are the crystal axes, E_x, E_y are the corresponding components of electric field of the coupled input signal (pump), ϵ_0 is the permittivity of free space, and d_{14} is the second-order nonlinear coefficient in contracted notation. The photonic band diagram for TM-like modes is shown in Fig. 5.3(a). Modes near the Γ point ($k_x = k_y = 0$) at the second harmonic wavelength can efficiently radiate into the numerical aperture of our objective lens (indicated by black solid lines). The mode with frequency closest to the second harmonic is indicated. The field patterns for this doubly degenerate mode [Fig. 5.3(b)] indicate that spatial overlap between the fundamental and second harmonic fields is best (i.e.

with the E_z field pattern that best matches $P_z^{(2)}$ described by the previous expression, maximizing $|\int dV E_z P_z|)$ for cavities oriented at $\theta = 0°$, in agreement with our experimental observations for cavities with different θ. The fundamental and second harmonic field patterns have imperfect spatial overlap; future optimization of this overlap, or introduction of a TM cavity mode at the second harmonic frequency [27], would improve conversion efficiency.

5.2.3 Experimental characterization of cavity-enhanced second harmonic generation

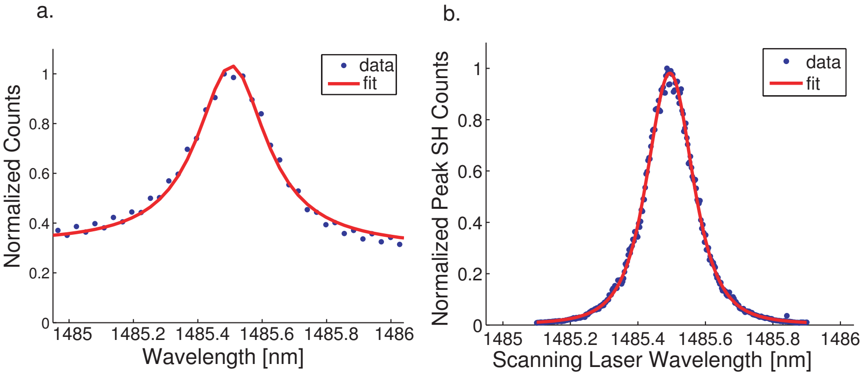

Figure 5.4: (a) Spectrum of fundamental resonance probed in cross-polarized reflectivity with a broadband source. Lorentzian fit gives a quality factor of 5600. (b) Spectrum at second harmonic as exciting laser frequency is tuned across the cavity resonance. Solid line shows fit to Lorentzian squared with cavity quality factor of 6000.

We first characterize the fundamental resonance of the cavities by probing them from vertical incidence using cross-polarized reflectivity with a broadband lamp [8] and a tunable laser. The cross-polarized configuration is used to obtain sufficient signal-to-noise to observe the resonance above the reflected background uncoupled to the cavity. We select cavities with fundamental TE-like modes at 1480 nm-1560 nm, within the range of our tunable laser. We estimate the coupling efficiency into the cavity to be approximately 5% by measuring the reflected and incident light power, in agreement with simulations for this type of cavity [74]. (For higher input coupling efficiency, the cavity could be integrated with photonic crystal waveguide couplers [75].) A typical reflectivity spectrum measured with a tungsten halogen white light source is shown in Fig. 5.2.3(a); the measured quality factor is 5600. Finite difference time domain (FDTD) simulations indicate that the Q-factor in this structure is limited to 15000 because of the thin slab. The spectral profile we observe is governed by the Lorentzian density of states of the cavity $\rho_c(\omega) = \frac{1}{\pi}\frac{\omega/2Q}{(\omega/2Q)^2+(\omega-\omega_c)^2}$ where ω_c and Q are the cavity frequency and quality factor respectively. Once we locate the fundamental resonance of the cavity, we use the continuous wave tunable infrared laser to generate second harmonic radiation, as depicted in Fig. 5.1. A typical spectrum of the second harmonic signal as we scan the laser through the cavity resonance is shown in Fig. 5.2.3(b). The cavity enhances the coupled input power by a factor proportional to Q^2 on resonance; away from resonance, this enhancement drops off like a Lorentzian squared. On resonance, the total second harmonic power P_{out} emitted depends on the square of the input power coupled to the cavity $P^2_{\text{in,coupled}}$, the square of the quality factor Q of the cavity, and the overlap between fundamental and second harmonic mode field profiles, $P_{\text{out}} \propto P^2_{\text{in,coupled}} Q^2 |\int \chi^{(2)}_{xyz} E_{x,\omega} E_{y,\omega} E_{z,2\omega} dV|^2$. From the second harmonic spectrum [Fig. 5.2.3(c)], we can extract the quality factor of the cavity mode equal to 6000, in good agreement with the Q observed in the reflectivity measurements at the fundamental wavelength (1500 nm).

To measure the absolute second harmonic power radiated, we send the second harmonic signal to a femto-Watt photodetector. Figure 5.5 shows the measured output power as a function of the incident power coupled into the cavity, assuming an input coupling to the cavity of 5%. The data show a good fit to a quadratic dependence on input power. We measure a normalized conversion efficiency $P_{\text{out}}/P^2_{\text{in,coupled}}$ of 430%/W, or $P_{\text{out}}/P_{\text{in,coupled}} = 5 \times 10^{-5}$ for 11 μW coupled input power ($P_{\text{out}}/P_{\text{in}} = 2 \times 10^{-6}$ for 220 μW power through the objective lens). The measured value is an underestimate of the second harmonic power generated inside the cavity, as we only measure radiation that is directed vertically and collected with our objective lens.

We also investigate the dependence of the second harmonic signal on the polarization of the incident light [Fig. 5.6(a)]. To couple power into the cavity and generate

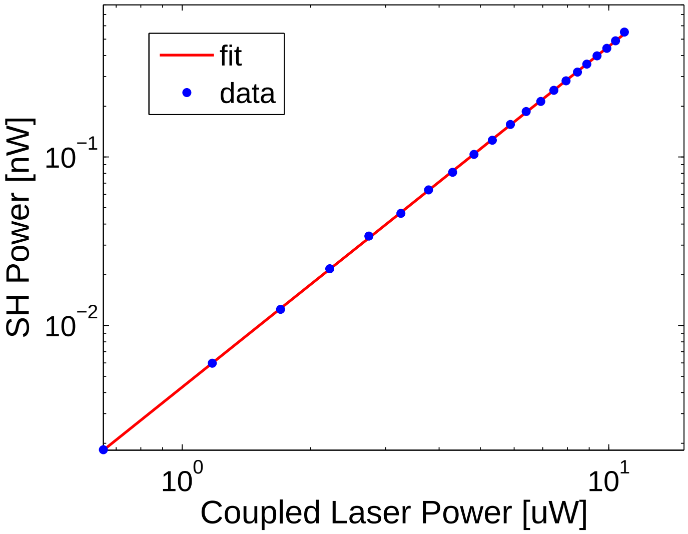

Figure 5.5: (a) Second harmonic power as a function of fundamental wavelength power coupled into the cavity. We estimate coupling efficiency into the cavity to be 5%. Solid line indicates fit, with slope 2.02, indicating quadratic power dependence. Output power measurements are corrected for measured losses from optics, but do not include corrections for collection efficiency into the objective lens.

resonantly enhanced second harmonic radiation, the incident light must have polarization aligned to the polarization the cavity radiates. For a cavity oriented at 45° relative to the crystal axes, we see maximum second harmonic signal when the input polarization is aligned to the cavity mode polarization, and a reduction from this maximum by a factor of $\cos^4(\theta)$ as the incidence angle is rotated away from the cavity, as expected for a quadratic process. We observe a similar angular dependence for cavities oriented at other angles to the crystal axes. Figures 5.6(b) and 5.6(c) show images of second harmonic radiation recorded on a camera (DVC 710M, 10s integration time), imaged through the objective lens, as indicated in Fig. 5.1(a). The radiation shows similar intensities for x' and y' polarizations, as expected for the TM band edge mode.

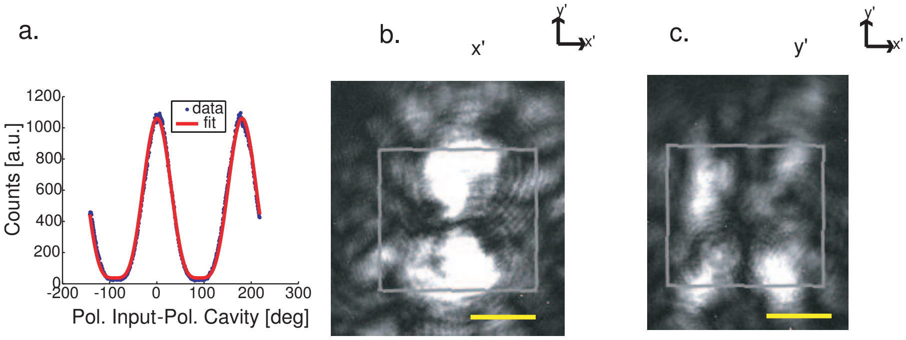

Figure 5.6: (a) Dependence of second harmonic power on incident light polarization. The horizontal axis corresponds to the angle between the input polarization and the polarization of the cavity mode. Solid line shows fit to $\cos^4(\theta)$. (b) and (c) Second harmonic radiation imaged on a camera with polarizer oriented in x' (b) and y' (c) direction [the orientation of cavity relative to the axes is shown in Fig. 5.2(b)]. The gray box indicates the approximate location of the photonic crystal structure, with scale bar indicating approximately 5 μm. Camera integration time for the same for both images.

5.3 Sum-frequency generation in GaP photonic crystal cavities

In this section, we demonstrate continuous wave (CW) sum frequency generation (SFG) using two modes of a photonic crystal cavity.

5.3.1 Cavity design and characterization

Our structures are fabricated in a 160-nm thick GaP membrane, which is grown on top of 1 μm $Al_{0.85}Ga_{0.15}P$ on a (100)-oriented GaP wafer by gas-source molecular beam epitaxy. Photonic crystals are defined by e-beam lithography and Cl_2-based dry etching[8], followed by a hydrofluoric acid undercut of the sacrificial AlGaP layer. The cavity is a modified three-hole linear defect[33] with lattice constant a =560 nm, $r/a \approx 0.25$, and slab thickness $d/a \approx 0.3$. We use a perturbation design for our photonic crystal cavities [74] to increase the coupling efficiency between the cavity and objective lens to 5% (verified experimentally by measurements of incident and reflected power). A scanning electron microscope (SEM) image of a fabricated structure is shown in Fig. 5.7a. The cavity axes are oriented parallel to the crystal axes.

We characterize the cavity resonances by normal-incidence cross-polarized white light reflectivity, using a tungsten halogen lamp as a source[8]. The cross-polarized configuration is used to obtain sufficient signal-to-noise ratio to observe the Lorentzian resonance above the reflected background uncoupled to the cavity. The white light reflectivity spectrum (Fig. 5.7b) shows several resonant modes (all with transverse-electric polarization), as expected for this cavity design[76], as well as the electric field intensities for the two modes used in our experiment. Fig. 5.7c shows a fit of the fundamental cavity mode to a Lorentzian, giving a quality factor of 3800. A Lorentzian fit of the higher order mode gives a Q of 220. (From finite difference time domain (FDTD) simulations, the expected quality factor of the fundamental mode is 10,000, limited by the thinness of the membrane. The expected quality factor of the higher order mode is 400.) The fundamental mode is primarily polarized along the y-axis (Fig. 5.7a); the second mode is polarized primarily along the x-axis.

5.3.2 Cavity-enhanced sum frequency generation

The experimental setup and principle of the experiment are shown in Figs. 5.8a, 5.8b. We use two continuous wave lasers, one matched to the wavelength and polarization of the fundamental mode (1565 nm), and one matched to the higher order mode (1504 nm); the nonlinear polarization generates sum frequency generation at 767 nm, as well as some second harmonic generation at 752 nm and 782.5 nm. Light from the two lasers is combined on a beamsplitter and passed through an objective lens (NA=0.5) and focused onto the sample; sum frequency and second harmonic signals are collected by the same objective and sent to a spectrometer.

Sum-frequency generation requires field components along x, y, and z axes (since only $\chi^{(2)}_{xyz} \neq 0$ for (100) GaP). For input beams, we use the two resonant modes of the cavity to provide the x and y oriented components. As in our previous experiments on second harmonic generation (SHG) in these cavities[9], we use a transverse magnetic-like (TM-like) Bloch mode of the photonic crystal (Fig. 5.8c) with electric field primarily along the z-axis to outcouple SFG light. Phase matching in the cavity geometry requires strong spatial overlap of modes at all three frequencies $P_{\text{out}} \propto P_{\text{in,coupled,1}} P_{\text{in,coupled,2}} Q_1 Q_2 | \int \chi^{(2)}_{xyz} E_{y,\omega_1} E_{x,\omega_2} E_{z,\omega_3} dV|^2$, where P_{out} is the generated sum frequency radiation, $P_{\text{in,coupled}}$ is the power coupled into the structure at ω_1 or ω_2, and Q_1 and Q_2 are the quality factors of the resonances at ω_1 and ω_2, assuming no depletion of the incident beams. Poor overlap of these three modes limits the measured conversion efficiency ($P_{\text{SFG}}/P_{\text{coupled,cavity}}$ to approximately 10^{-8}, where $P_{coupled,cavity}$) is the coupled laser power in the fundamental mode (coupled power in the higher order mode is an order of magnitude higher).

Fig. 5.9a shows a spectrum when both lasers are incident on the cavity; there are three peaks, two due to second harmonic of each laser at the cavity wavelength; the central peak is sum frequency generation. We characterize the sum frequency radiation by studying its dependence on the wavelength and power of a single laser, in this case the laser aligned to the fundamental mode of the cavity (black box shows second harmonic from this mode). Fig. 5.9b shows the power dependence of sum frequency generation counts (sum of counts in green box) and counts from second harmonic at the fundamental wavelength (sum inside red box). A polynomial fit of second harmonic counts shows a power dependence of 1.8, close to the expected 2.0; a fit to the sum frequency counts shows a power dependence of 0.9, close to the expected 1.0. By adjusting the power, we can also control whether we observe more light from sum frequency generation or second harmonic generation. Fig. 5.9c shows the dependence of sum frequency and second harmonic counts (green and red boxes respectively) on the wavelength of the laser tuned near the fundamental cavity mode. The density of states at the output wavelength is determined by the product of the Lorentzian densities of states for each of the participating input modes ($\rho_c\left(\lambda\right) = \frac{Q\lambda}{\pi^2 c}\frac{1}{1+4Q^2\left(1-\frac{\lambda}{\lambda_c}\right)^2}$ where λ_c and Q are the cavity wavelength and quality factor respectively for each mode). We observe this spectral profile by detuning the laser from the fundamental wavelength of the cavity, while keeping the input beam at the higher order mode fixed. For second harmonic generation, we fit the data to a Lorentzian squared, which gives a Q of 4100. For the sum frequency radiation, we fit the data to a Lorenztian, giving a Q of 4300. These Q's are in good agreement with the value measured from cross-polarized reflectivity. To increase the tunable range of the output light, we can alternatively scan the laser at the wavelength of the higher order cavity mode, which has a lower Q (Fig. 5.9d). Finally, we believe the sum frequency and second harmonic of both cavity modes outcouple through the same TM Bloch mode of the crystal (Fig. 5.8c), as the radiation pattern collected through the objective and imaged onto a camera looks similar at all three wavelengths.

5.4 Second harmonic generation in GaP photonic crystal waveguides

Previous work in $\chi^{(2)}$ nanophotonic nonlinear frequency conversion[7, 9, 10] has focused on using nanophotonic cavities with high quality factor (Q) to generate a resonant enhancement in conversion efficiency at the wavelength of the cavity mode; however, the narrow bandwidth of a high-Q cavity would be unsuitable for frequency conversion of quantum emitters with a broadband spectrum (such as the nitrogen vacancy (NV) center) or frequency conversion of ultrashort pulses. Photonic crystal

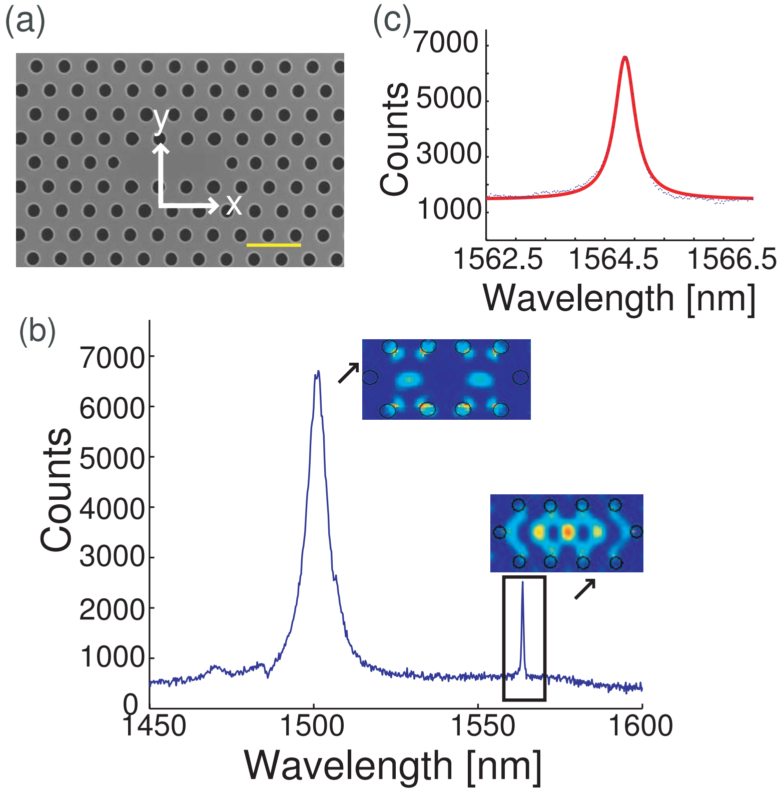

Figure 5.7: (a) Scanning electron microscope image of a fabricated photonic crystal membrane after undercut of sacrificial layer. Scale bar indicates 1 μm. (b) White light reflectivity from cavity, with FDTD simulations showing electric field of modes of interest. The two modes, both transverse electric-like (TE-like) are polarized orthogonally: the fundamental mode is y-polarized; the higher order mode is x-polarized. (c) Fit to Lorentzian of fundamental mode (peak indicated by black box) with Q=3800.

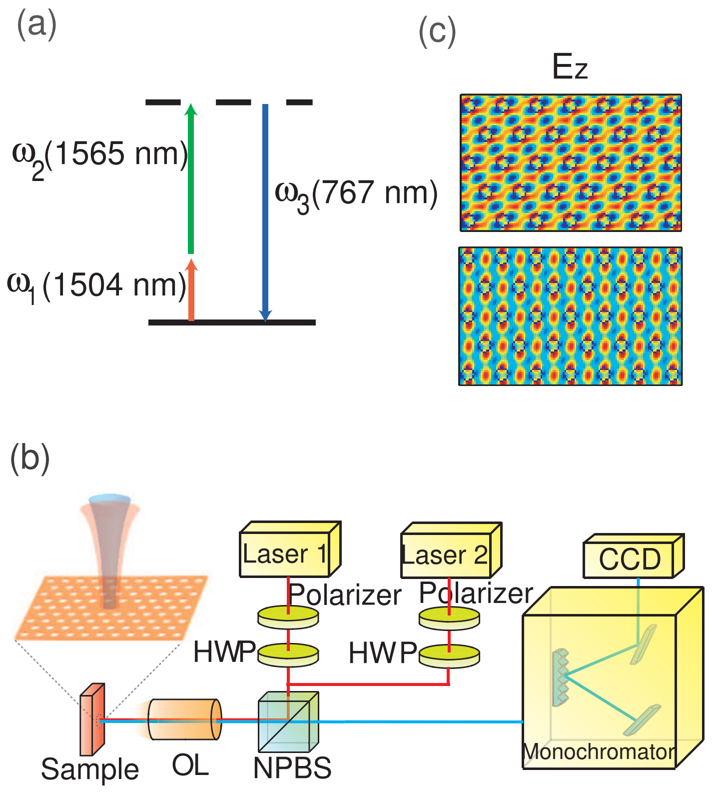

Figure 5.8: (a) Schematic of sum frequency generation process. Incident photons with frequencies ω_1 and ω_2 are converted to frequency ω_3. (b) Experimental setup for SFG. HWP: half wave plate, NPBS: nonpolarizing beamsplitter, OL: objective lens. The incident light traces the red line into the cavity sample; the sum frequency light follows the blue line into the spectrometer. The polarization of the incident light is controlled by a polarizer and HWP. (c) Simulated electric field pattern of degenerate TM-like Bloch modes of the crystal at wavelength of sum frequency.

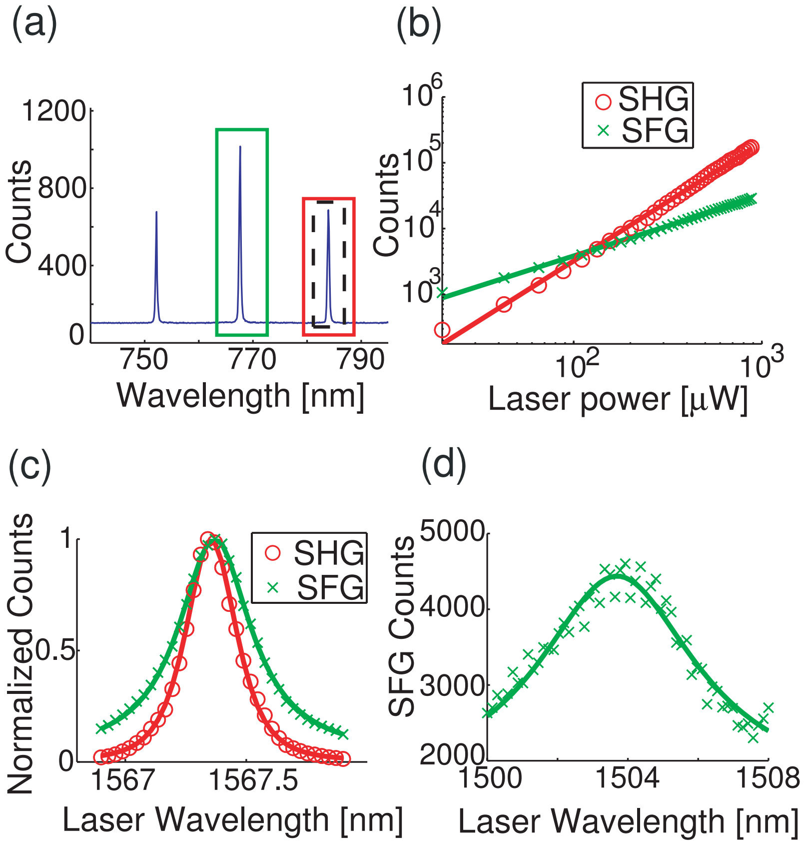

,

Figure 5.9: (a) Sum-frequency generation and second harmonic generation when two lasers are used to couple into modes shown in Fig. 5.7. Middle peak (green box) is sum frequency generation; right (black dotted and red boxes) and left peaks are second harmonic generation from each mode. Black box indicates second harmonic from fundamental mode over which laser is scanned to measure power and wavelength dependence in Fig. 5.9b and 5.9c. (b) Power dependence of second harmonic and sum frequency generation as a function of incident laser power at wavelength of fundamental cavity mode. A polynomial fit (plotted on log-log scale) gives a coefficient of 0.9 for sum-frequency generation (green squares) and 1.8 for second harmonic (red circles). The incident power of the second laser at higher order cavity mode wavelength is 6 mW. (c) Wavelength dependence of sum frequency (green squares) and second harmonic counts (red circles) as a function of scanning laser wavelength at fundamental cavity mode. Fit to Lorentzian of SFG counts gives Q of 4300; fit to Lorentzian squared of SHG counts gives Q of 4100, both matching Q of the fundamental mode in Fig. 5.7, as expected. The other laser is at 1504 nm. (d) Wavelength dependence of sum frequency counts as a function of scanning laser wavelength at higher order cavity mode. Fit to Lorentzian of SFG counts gives Q of 272, matching Q of the higher order mode. Second laser is at 1567.4 nm.

waveguides offer an alternative to cavities; the waveguide photonic dispersion can produce large slow-down factors greatly increasing the effective nonlinear interaction length over a broad wavelength range[73, 77]. Third harmonic frequency conversion has been previously demonstrated in a silicon photonic crystal waveguide[73]; however, the efficiency is limited by the weak $\chi^{(3)}$ nonlinearity of the material, linear absorption of the third harmonic, and two-photon absorption of the fundamental frequency. Here, we demonstrate second harmonic generation using the $\chi^{(2)}$ nonlinearity of gallium phosphide, which has a large electronic band gap (∼550 nm) minimizing absorption. The circulating intensity in the waveguide is enhanced by the group index n_g, providing a factor of n_g^2 enhancement in conversion efficiency compared to a conventional waveguide with similar size. This material is compatible with quantum emitters including InP[78] and InGaAs quantum dots[79], NV centers[80], and fluorescent molecules[15].

5.4.1 Design and fabrication of photonic crystal waveguide

Fig. 5.10 shows the dispersion diagram of transverse electric (TE)-like modes (in-plane E field component only at the center of the slab) of the W1 waveguide. The W1 waveguide is formed by removing one row of holes from the triangular lattice[81]. The photonic band gap is indicated by the white region between the shaded gray areas. The structure supports two guided modes inside the band gap with even (mode of interest) and odd symmetry of the B_z field component relative to the xz-plane containing the waveguide axis. The inset shows the field component B_z of the photonic crystal waveguide mode calculated from 3D finite difference time domain (FDTD) simulation at the $k_x=\pi/a$ point for the green band (even mirror symmetry). Here, no other changes to the photonic crystal have been made, although the group velocity dispersion could be decreased by using modified designs shifting the first two rows of holes relative to the defect[82].

Fig. 5.10b shows a scanning electron microscope (SEM) image of a photonic crystal waveguide fabricated in a 164 nm thick gallium phosphide membrane. The membrane is grown by gas-source molecular beam epitaxy on top of a 1 μm thick layer of $Al_{0.85}Ga_{0.15}P$ on a (100)-oriented gallium phosphide wafer. The structures are fabricated by e-beam lithography and dry etching through the GaP membrane followed by a wet etch to remove the sacrificial layer yielding a suspended membrane. The W1 waveguide is fabricated with lattice constant a=560 nm, hole radius $r/a \approx 0.25$, and is 30 periods (17 μm) long. To access wavevectors of the dispersion lying below the light line (which have low loss and large group index) from normal incidence, the structure includes two grating couplers: a circular $\lambda/2n$ grating on the left[83] and a coupler on the right formed by perturbing the lattice with periodicity $2a$ using enlarged holes[84] (used only for transmission measurements). The structures are oriented with the waveguide along a [011] crystal direction. For transmission measurements, an objective lens with numerical aperture of 0.5 is positioned above right grating; the light source is focused slightly off-center onto the left grating. Fig. 5.11a shows transmission measurements using a tungsten halogen white light source. Periodic peaks in transmission result from the finite length of the waveguide (30 periods) which supports Fabry Perot (FP)-like reflections with peaks separated by $\lambda^2/(2Ln_g)$ where L is the length of the waveguide and n_g is the group index[85]. The linewidths of the peaks become narrower as the wavelength increases into the part of the dispersion below the light line. The derived group index is shown in Fig. 5.11b. The maximum group index measured is 25, lower than expected from simulation (Fig. 5.11), but still much larger than in a conventional waveguide.

5.4.2 Experimental characterization of waveguide transmission and enhanced second harmonic generation

To measure second harmonic generation, we couple light from a tunable continuous wave telecommunications-wavelength laser (Agilent 81989A) into the left grating. Second harmonic generated inside the waveguide scatters out of plane and is collected by the same objective placed above the center of the structure from the entire field of view onto a camera for imaging or a monochromator and CCD for spectral analysis. The collected second harmonic radiation as a function of incident laser wavelength is shown in Fig. 5.11c for a different structure with slightly larger r/a that better matched the range of our tunable laser. Conversion is observed over a range of incident wavelengths, with periodic peaks again observed from Fabry Perot (FP) reflections at the fundamental wavelength. The inset shows the close match between the second harmonic counts at the FP peaks and the expected n_g^2 enhancement, where n_g is calculated from the experimentally measured spacing between FP peaks in the second harmonic data. Fig. 5.11d shows the second harmonic counts measured as a function of incident laser power transmitted through the objective. The laser wavelength is 1561.5 nm; the calculated group index for this structure at this wavelength is 30. A log-log fit of the data yields a slope of 1.9, close to what is expected for a second-order process. The estimated external conversion efficiency, calculated from the maximum second harmonic intensity is 10^{-9} for 2 mW transmitted through the objective, or 5×10^{-7}/W. The power at second harmonic wavelength was measured by separately calibrating the spectrometer counts with a laser at the second harmonic wavelength using a power meter. This conversion efficiency is four orders of magnitude less than that measured for photonic crystal cavities in GaP[9]. As a comparison to previous work on frequency conversion in III-V semiconductors, we note that our device, which has not been optimized for incoupling or outcoupling efficiency, has only $70,000$ times lower second harmonic external conversion efficiency for 1.5 μm light than past experiments (using GaAs/AlGaAs waveguides phase matched by orientation patterning[86] that require significantly more complicated MBE growth) that used a ridge waveguide 300 times longer.

5.4.3 Measurement and simulation of second harmonic in the far field

Because the only nonzero elements of the $\chi^{(2)}_{xyz}$ tensor for (100)-grown GaP have $x \neq y \neq z$ and the guided mode of the photonic crystal waveguide at the fundamental wavelength has electric field in-plane only, the second harmonic must have electric field out-of-plane, e.g. couple to transverse magnetic-like (TM-like) mode. A 3D FDTD simulation of electric field at the second harmonic frequency in a periodic triangular photonic crystal lattice is shown in Fig. 5.12a; the symmetry of the electric fields indicates a monopole mode with far-field radiation pattern (calculated from the Fourier transform of the field immediately above the slab[87]) shown in Fig. 5.12b. The removal of a row of holes to form the W1 photonic crystal waveguide perturbs this mode; the resulting electric field is shown in Fig. 3c, with far field patterns in Figs. 5.12d-f. The simulated quality factor of the mode is 200, more than an order of magnitude lower than for the same mode unperturbed by the waveguide. To verify experimentally that we collect second harmonic through this mode, we image the radiation pattern from the waveguide onto a camera (Figs. 5.12g-i) using a Glan Thompson polarizer to resolve different polarizations; the resulting images show very good agreement with the simulations. The wavelength of the incident laser for these measurements is 1561.5 nm ($a/\lambda = 0.359$, in good agreement with simulations (Fig. 5.10)).

5.4.4 Conclusions

In summary, we demonstrate efficient second harmonic generation in the visible from photonic crystal cavities with incident powers well below 1 μW as a result of resonant recirculation of the pump (1500 nm) light in the GaP nanocavity. By using a GaP membrane for our structures, we minimize absorption losses at the output wavelength of 750 nm. Additionally, our device can be integrated with a tapered optical fiber (which creates near-field as well as mechanical perturbatons) to create a frequency-tunable second harmonic source with bandwidth of >10 nm as described in Ref. [88]. We have also shown continuous wave sum frequency generation using two modes of a photonic crystal cavity, which provides a nonlinear optics-based on-chip source that can easily be tuned by changing the frequencies of the cavity resonances. By matching a high Q mode with a low Q mode, we create a source that is tunable over $\approx$ 10 nm range. Finally, we demonstrate enhancement of second harmonic generation in GaP in a photonic crystal waveguide with maximum group index of 30. We measure an external conversion efficiency of 5×10^{-7}/W or 10^{-9} for 2 mW incident power.

Our structures could serve as on-chip, low-power sources compatible with semiconductor fabrication processing. These results also indicate the potential of microcavities for significantly reducing the required input powers for other experiments in nonlinear optics, such as sum/difference frequency generation and parametric down-conversion, as well as for on-chip upconversion of weak infrared signals to visible wavelengths[89, 90]. Our results using the waveguide geometry are promising for frequency conversion of on-chip integrated emitters having broad spectra (e.g., NV centers) or large inhomogeneous broadening (e.g., InAs/GaAs quantum dots), as well as for frequency conversion of ultrashort pulses.

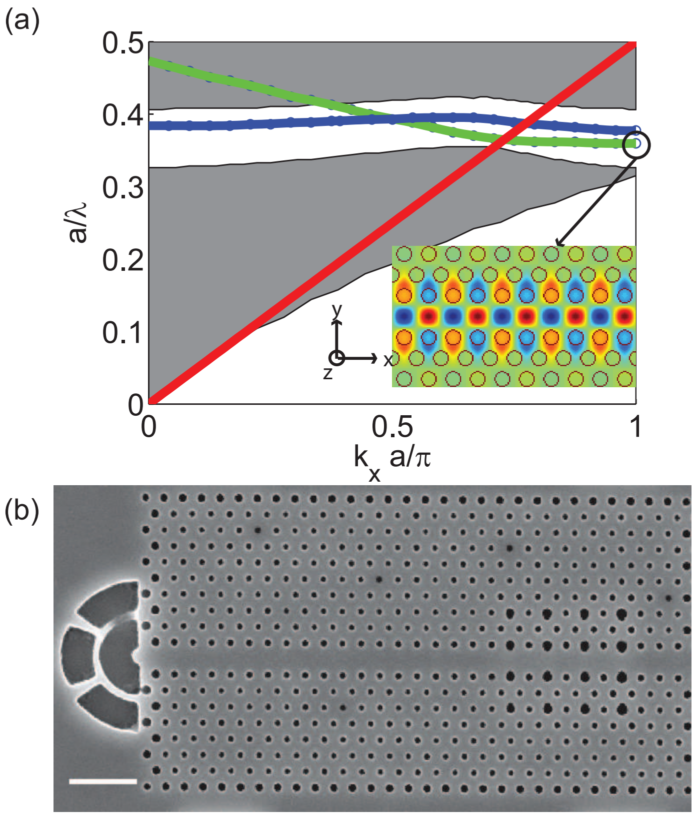

Figure 5.10: (a) Dispersion diagram for TE-like modes (E-field at the center of the slab in plane) for W1 waveguide. Parameters are: hole radius r/a=0.25 and thickness d/a=0.25 where a is periodicity in $\hat{x}$ direction. The white area between the gray shaded regions indicates the photonic band gap of the triangular lattice photonic crystal. The green line indicates the waveguide mode with even symmetry of the B_z field component relative to the x-z plane (including waveguide axis). The blue line indicates waveguide mode with odd symmetry. Circles indicate FDTD-calculated solutions, and solid lines indicate interpolated bands. Red line indicates light line. The inset shows the FDTD simulation of the B_z field component at the center of the slab for the band plotted in green at the $k_x = \pi/a$ point (circled) with frequency a/λ=0.36. (b) SEM image of 30-periodic PC photonic crystal waveguide fabricated in 160 nm thick GaP membrane with a=560 nm. Scale bar indicates 2 μm. Circular grating at left or modified holes forming coupler (right) can be used to couple into waveguide modes from free space.

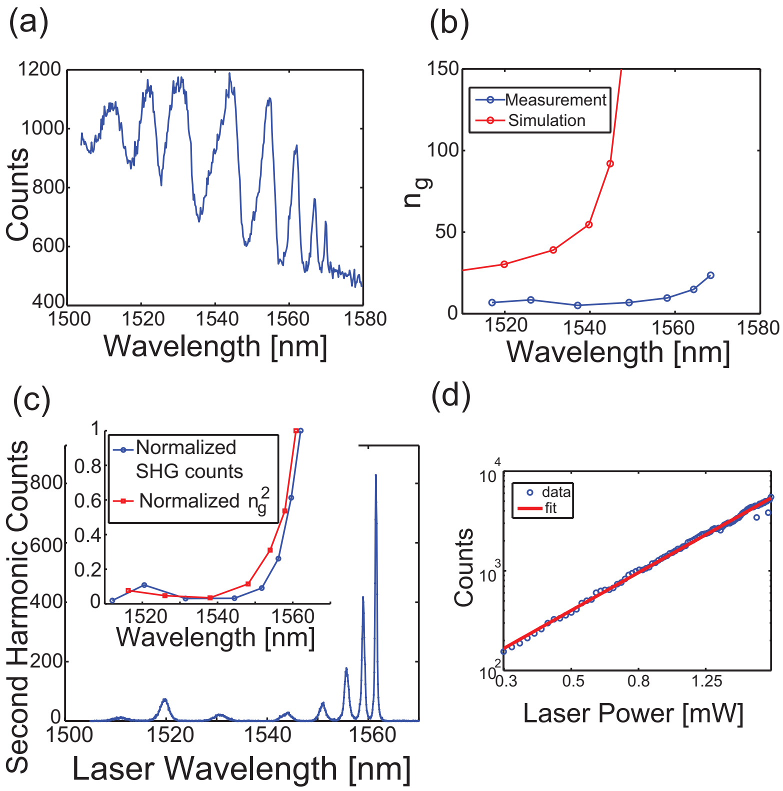

Figure 5.11: (a) Transmission measurement through photonic crystal waveguide using white light source. (b) Group index calculated from FDTD simulation (Fig. 5.10a) and experimental data (Fig. 5.11a). Maximum group index measurement experimentally is 25. (c) Second harmonic intensity measured from a different structure as a function of incident laser wavelength. Inset: second harmonic counts at the FP peaks and calculated n_g^2 as a function of wavelength. (d) Second harmonic counts measured as a function of incident laser power. Red line indicates linear fit of log-log data with slope 1.9. The laser wavelength is 1561.5 nm; the calculated group index at this wavelength is 30.

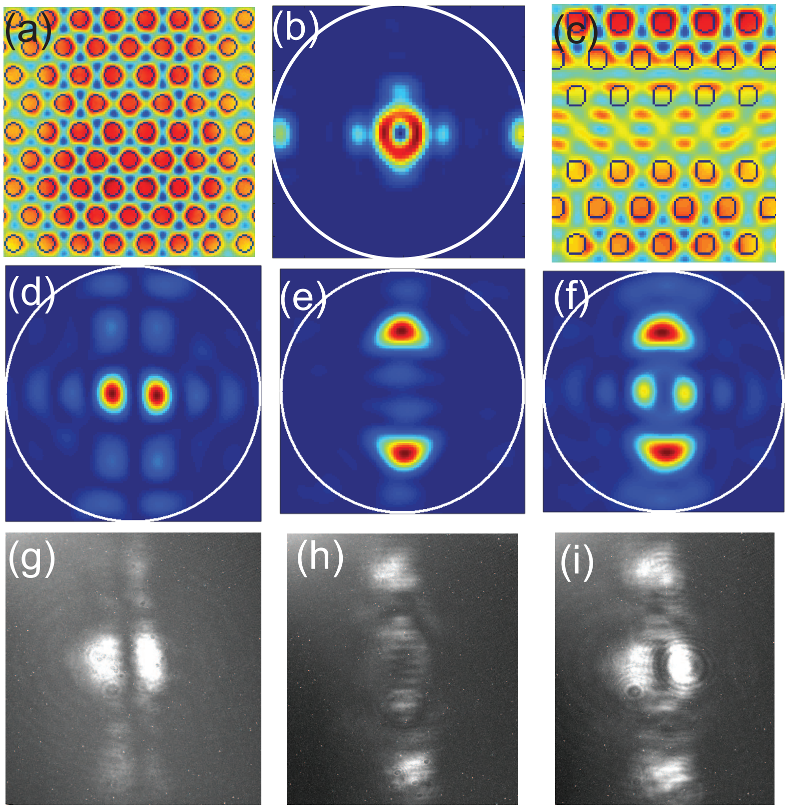

Figure 5.12: (a) FDTD simulation of E_z field component of the monopole TM-like mode near frequency of second harmonic in triangular photonic crystal lattice. (a/λ=0.67) (b) Calculated far-field radiation pattern of mode in (a). White circle indicates numerical aperture of lens. (c) FDTD simulation of E_z in photonic crystal waveguide at second harmonic frequency (a/λ=0.71). (d) Calculated far-field radiation pattern of $|E_x|^2$ for mode in (c). (e) Calculated far-field radiation pattern of $|E_y|^2$ for mode in (c). (f) Calculated far-field radiation pattern of $|E|^2$ for mode in (c). (g) Measured radiation pattern for $|E_x|^2$. (h) Measured radiation pattern for $|E_y|^2$. (i) Measured radiation pattern $|E|^2$.

Chapter 6

Fast quantum dot single photon source triggered at telecommunications wavelength

This chapter presents the demonstration of the fastest optically pumped single photon source by using intracavity second harmonic generation enhanced by a GaAs photonic crystal cavity. This configuration is simpler and faster than conventional optically pumped quantum dot single photon sources, which rely on Ti:Sapphire lasers that operate at a fixed repetition rate of ≈80 MHz.

6.1 Motivation

Single quantum emitters such as nitrogen vacancy centers [91], molecules [48], semiconductor quantum dots [92], and atoms [93] emit antibunched light suitable for communications requiring single photons[94, 95]. Among these systems, semiconductor quantum dots have the highest emission rates and can be most easily integrated with semiconductor technology, including microcavities with high quality factor, small volume, and directional emission that increase the emission rate, efficiency, and indistinguishability of the generated single photons.[96, 92]

However, the generation rate of demonstrated optically triggered quantum dot single photon sources has been limited by excitation (Ti:Sapphire) lasers to around 80 MHz [92]. Electrical excitation [97, 98] can circumvent this; however, resonant optical excitation [96] improves the indistinguishability of output photons, and many desirable microcavity structures such as photonic crystal cavities have geometries that are challenging to pump electrically [99]. Furthermore, while telecommunications wavelengths are desirable for transporting photons over long distances, excitation and emission in many quantum dot materials systems, determined by material parameters, occurs at much shorter wavelengths.

As described in the previous chapter[9, 10], we demonstrated that photonic crystal cavities fabricated in III-V semiconductors with large $\chi^{(2)}$ nonlinearities can greatly enhance nonlinear frequency conversion efficiency, as a result of light recirculation inside an ultrasmall volume. Here, we apply a similar approach to excite a single InAs quantum dot (with transitions ∼900 nm) using a commercially available telecommunications wavelength (∼1550 nm) laser that can serve as a trigger at GHz speeds when paired with a lithium niobate electro-optic modulator.

6.2 Cavity design and fabrication

A scanning electron microscope image of the three-hole linear defect photonic crystal cavity[33] is shown in Fig. 6.1a. The structures are fabricated in a 164 nm thick GaAs membrane using e-beam lithography, dry etching, and HF wet etching of the sacrificial layer beneath the membrane, as described previously [62]. Quantum dots are grown by molecular beam epitaxy in the center of the membrane. The cavity axis is oriented along a [011] crystal direction.The quantum dot density is <10 quantum dots/μm^2, and the quantum dot inhomogeneous broadening is around 40 nm, preventing multiple quantum dots from having resonances at the same frequency.

6.3 Continuous wave excitation of quantum dot

Finite difference time domain simulations of the electric field components (TE-like resonance with electric field primarily in the plane of the photonic crystal slab) are

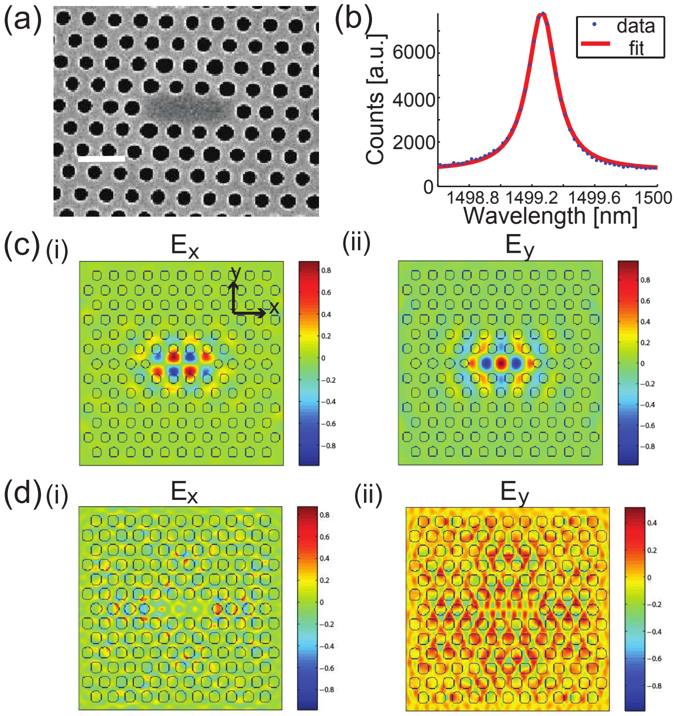

Figure 6.1: Photonic crystal cavity design and fabrication. (a) SEM image of fabricated suspended membrane photonic crystal cavity. Scale bar indicates 1 μm. (b) Reflectivity measurement of fundamental cavity mode. Lorentzian fit gives Q of 7000. (c) (i) and (ii) Simulated electric field components for fundamental mode of L3 photonic crystal cavity, used for resonantly enhanced upconversion. (d) (i) and (ii) Electric field patterns for TE mode closest to emission frequency of quantum dot. The low Q (<100) mode is formed through weak confinement of an air band mode.

shown in Fig. 6.1c. A reflectivity spectrum of the cavity showing a resonance at ∼1500 nm, measured with a broadband source in the cross-polarized configuration (as in our previous work [8]) to maximize signal to noise, is shown in Fig. 6.1b. A Lorentzian fit gives a cavity Q of 7,000. GaAs has a noncentrosymmetric cubic crystal lattice with $4\overline{3}$m symmetry; the only non-zero elements of the bulk $\chi^{(2)}_{ijk}$ tensor have $i \neq j \neq k$. Since normally incident light couples to the TE-like photonic crystal cavity mode (Fig. 6.1c, with dominant E_x and E_y in-plane field components), the generated nonlinear polarization (and accordingly second harmonic, as described in [9]) is $\hat{z}$-polarized, i.e., transverse magnetic-like (TM-like) mode. For a photonic crystal, this corresponds to guided resonances in the TM-like air-band [9]. The second harmonic at 750 nm is used to excite the quantum dot above the GaAs band gap. Anisotropy of the quantum dot causes the dot to emit with TE polarization; at the quantum dot wavelength (∼900 nm), the photonic crystal supports an optical (air-band) TE-like mode (Fig. 6.1d), weakly localized by the perturbation from removing and shifting holes near the cavity.

6.4 Pulsed excitation triggered single photon source

A tunable telecommunications wavelength continuous wave laser (Agilent 81989A, 1463 nm - 1577 nm) is coupled into the fundamental high-Q mode of the cavity. Photons upconverted in the cavity through second harmonic generation excite the quantum dot above band; the emitted single photons from the quantum dot are spectrally filtered and sent to a spectrometer or Hanbury Brown-Twiss (HBT) setup, in which photons are split by a 50/50 beamsplitter to two single photon counters[92], for photon statistics analysis. The telecom wavelength laser can also be modulated for triggered single photon source operation. For direct recombination lifetime measurements of the quantum dot, we alternatively use an ultrashort pulse (3 ps) Ti:Sapphire laser to excite the dot and a streak camera for detection.

Continuous wave (CW) excitation is shown in Figure 6.2. Fig. 6.2a shows the photoluminescence spectrum measured when the continuous wave tunable laser, on resonance with the cavity mode (at ∼1500 nm), is normally incident on the structure. Spectral filters are used to create an effective bandpass filter (∼5 nm FWHM) centered at 898 nm. The measured counts from the two strongest lines (red box, Fig. 6.2a) both show linear dependence on pump power at low optical power; we believe these may be different charge states of the single-exciton[100].

To determine the maximum speed at which the system can be modulated, we perform an independent experiment directly measuring the quantum dot lifetime with a streak camera (2 ps timing resolution), using a Ti:Sapphire laser at 750 nm with 80 MHz repetition rate and 3 ps pulses to excite the dot (Fig. 6.2a, inset). To accumulate sufficient counts, data from peaks shown in the red box in Fig. 6.2a were summed. The data were fit to a monoexponential decay with time constant 2.4±0.1 ns (where given error is one standard deviation).

To verify that the upconverted light from the CW tunable laser could be used to efficiently excite a single quantum dot, we perform a photon correlation measurement of the signal collected through our spectral filter (Fig. 6.1a) at ~898 nm (QD emission wavelength) using the HBT setup. Figure 6.2b shows the histogram of coincidence counts as a function of time delay τ between the two detectors. The data were fit to the unnormalized correlation function $G^{(2)}(\tau) =< I(t+\tau)I(t) >= A[1-(1-g^{(2)}(0))e^{-|\tau|/\tau_0}]$ [100], where A, τ_0 and $g^{(2)}(0)$ are fitting parameters, and $1/\tau_0 = \Gamma + r_p$ where Γ is the spontaneous emission lifetime and r_p is the pump rate. The symmetric antibunching in coincidence counts at zero time delay $\mathrm{g}^{(2)}(0)$=0.43±0.04, normalized such that $\mathrm{g}^{(2)}(\infty)$=1, indicates emission primarily from the same initial state of a single quantum dot (since $\mathrm{g}^{(2)}(0) < 0.5$)[100]. Background subtraction for a signal to noise ratio of $S/N \approx 10$ gives $\mathrm{g}^{(2)}(0)$=0.31±0.05. An exponential fit to the central antibunching dip gives a decay rate of 2.3±0.2 ns; by comparison with independent lifetime measurements, this indicates that the quantum dot is pumped in the low power regime, far below saturation.

To realize a triggered single photon source, the telecom tunable laser is modulated by a gigahertz electro-optic modulator (JDSU), which is driven by a pulse pattern generator (Anritsu 1800A) that receives an external clock signal from a synthesizer sweeper (Agilent) (Fig. 6.3). Photon correlation measurements were performed with the same HBT setup as in the CW experiment (Fig. 6.2). The repetition rate of the source was varied between 100 and 300 MHz, with duty cycle 20-50% (minimum duty cycle for which the experiment could be performed was limited by background from the modulator during the off portion of the cycle; the finite excitation duration likely increases $\mathrm{g}^{(2)}(0)$), as a result of the quantum dot re-excitation. A schematic of the pulsed excitation single photon source measurement is shown in Fig 6.4.

Fig. 6.5a shows the measured photon statistics for a repetition rate of 100 MHz. The peaks were fit to exponentials with a single decay rate, and the ratio of the areas of the fitted peaks was used to determine $\mathrm{g}^{(2)}(0)$=0.49±0.07 ($\mathrm{g}^{(2)}(0)$=0.38±0.08 with background subtraction, indicating multi-photon probability suppression to 38% relative to an attenuated laser of the same power). We observe a reduction in $g^{(2)}$ for the immediately adjacent peaks (up to two repetition periods) to the $\tau = 0$ peak to a value intermediate between the value for the central peak and the saturated value. This long timescale negative correlation may be caused by memory effects resulting from long-lived charged states in the quantum dot [101]. Fig. 6.5b shows photon correlation measurements for repetition rate of 300 MHz; $g^{(2)}(0)=0.40\pm0.09$ ($g^{(2)}(0)=0.3\pm0.1$ with background subtraction). At 300 MHz, coincidences from consecutive pulses begin to overlap, as a result of the excitation repetition period approaching the quantum dot lifetime.

6.5 Conclusions

In conclusion, we have demonstrated an optically triggered single photon source operating at 100 MHz (with suppression of $g^{(2)}(0)$ visible up to 300 MHz), excited with a telecommunications wavelength (∼1500 nm) laser followed by an electro-optic modulator. In our system, the rate of single photons is limited primarily by the spontaneous emission rate of the quantum dot. A doubly resonant cavity with resonances at both telecommunications frequency and the frequency of the dot would increase the spontaneous emission rate of the dot via the Purcell effect[102], and enable the realization of a significantly faster (e.g. >1 GHz) triggered single photon source. Photons emitted from the quantum dot could also be frequency converted back to telecommunications wavelengths via difference frequency generation using the nonlinearity of the surrounding GaAs material [103] providing a full interface between the ∼900 nm quantum node and the optical fiber network.

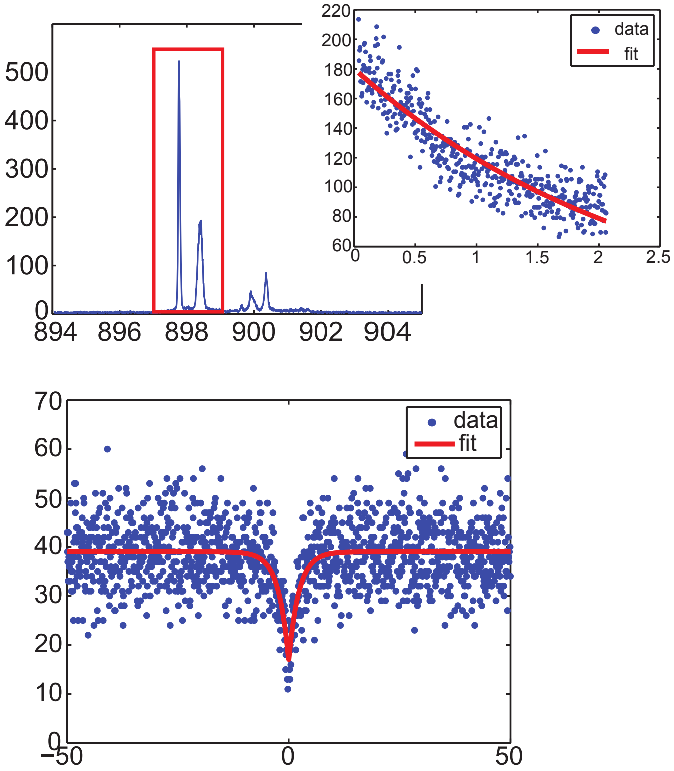

Figure 6.2: Characterization of single quantum dot excited with on-chip-upconverted 1500 nm laser. (a) Spectrum measured from CW second harmonic excitation of quantum dot. Inset: Streak camera measurement of quantum dot lifetime. Counts were summed over spectral window indicated by box. (b) Photon correlation measurement of quantum dot emission under frequency doubled CW 1550nm excitation. Fit gives $g^{(2)}(0)=0.43\pm0.04$.

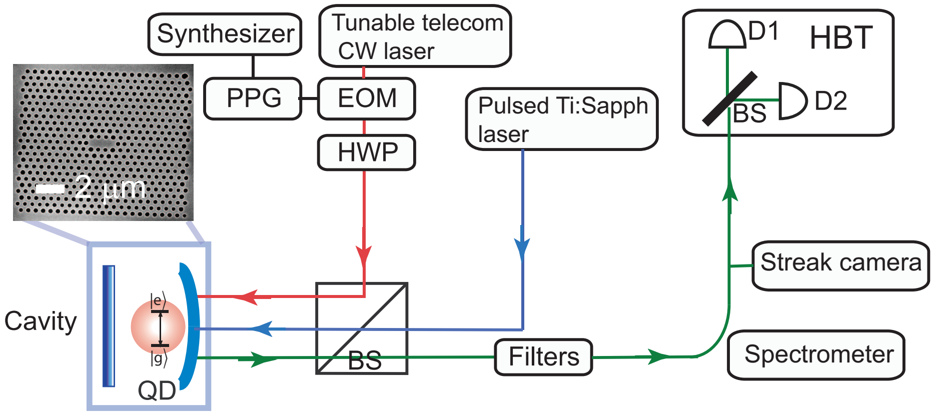

Figure 6.3: Experimental setup. A tunable C-band laser (red excitation path) is modulated by an electro-optic modulator (EOM) driven by a pulse pattern generator (PPG), which receives an external clock signal from a synthesizer. The laser polarization is adjusted to match that of the cavity by a half wave plate (HWP). Pulses incident on the cavity via a non-polarizing beamsplitter (BS) excite quantum dots by above band absorption of laser pulses upconverted through second harmonic generation in the surrounding GaAs matrix. Emission from the quantum dot (green path) is spectrally filtered, then analyzed either by an HBT setup for photon correlation measurements or a spectrometer. For direct lifetime measurements of the quantum dot, an ultrashort pulse (3 ps) Ti:Sapphire laser at 80 MHz repetition rate excites the dot (blue excitation path); a streak camera is used for detection. Inset shows scanning electron microscope image of photonic crystal cavity.

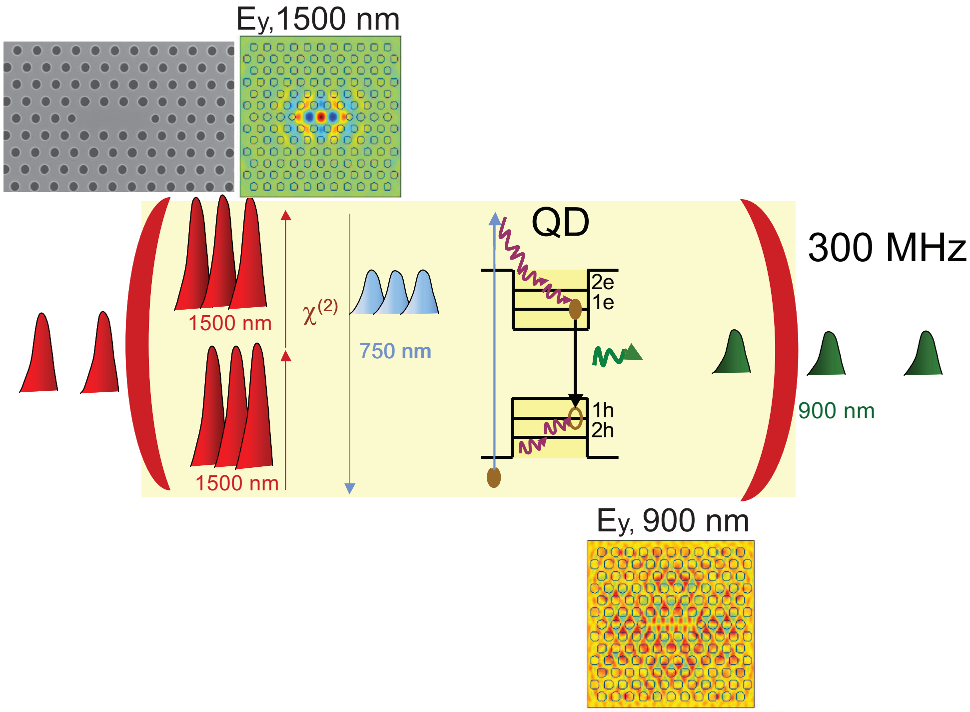

Figure 6.4: Schematic illustrating principle of fast upconversion-based telecom wavelength-triggered quantum dot single photon source. Pulses at 1500 nm are coupled into the cavity resonance, leading to strongly enhanced second harmonic generation. The light at the second harmonic frequency can create carriers in the GaAs membrane that relax into the quantum dot, which are then emitted as single photon pulses. The rate of single photon pulses is determined by the rate at which the laser is modulated.

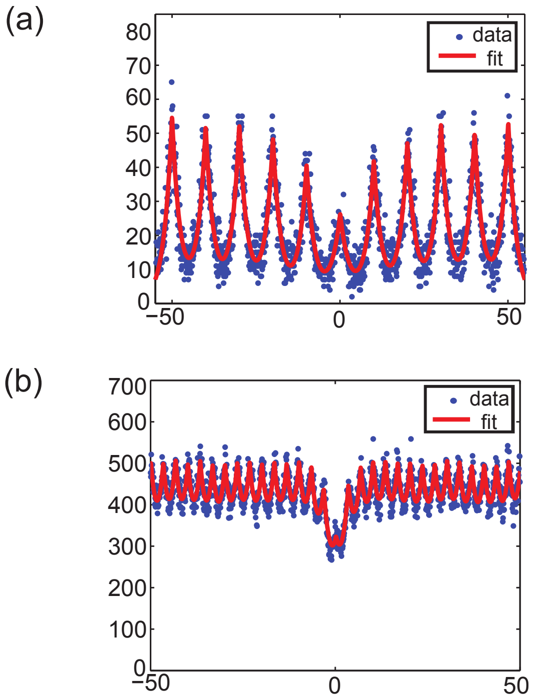

Figure 6.5: Photon correlation measurement of quantum dot emission when triggered with frequency doubled telecom wavelength laser pulses from an externally modulated telecom wavelength laser. (a) Second order autocorrelation function measurement for 100 MHz repetition rate with duty cycle 20%. $g^{(2)}(0) = 0.48 < 0.5$ indicates emission from a single quantum dot. (b) Second order autocorrelation measurement for repetition rate 300 MHz with duty cycle 50% and $g^{(2)}(0)=0.40$.

Chapter 7

Multiply resonant high quality photonic crystal nanocavities

This chapter presents the design, fabrication, and linear and nonlinear characterization of photonic crystal cavities with multiple resonances separated by large frequency, which are intended for use in frequency conversion devices.

7.1 Motivation

State of the art photonic crystal nanocavity designs[36, 38, 39, 37] can be optimized to generate quality factors exceeding one million for a single cavity resonance. For nonlinear optical interactions such as frequency conversion or stimulated Raman scattering, however, it is desirable to have multiply resonant nanostructures[24] with arbitrary frequency separation and with good spatial field overlap. To enable nonlinear coupling of cavity resonances, structures can be fabricated in a III-V semiconductor such as GaP or GaAs (for second or third order optical nonlinearity) or a group IV semiconductor such as silicon (for third order nonlinearities, such as Raman scattering or four wave mixing), as described previously in this thesis. Past experimental work in three and four-wave mixing in semiconductor photonic crystal nanocavities has been implemented using designs featuring a single photonic band gap [9, 10, 7, 104, 105]. Within a single photonic band gap, however, it is difficult to independently control their frequencies; moreover, field patterns of different resonances typically have minimal spatial overlap, and the absolute frequency separation between resonances is limited by the size of the photonic bandgap. Photonic crystals and quasicrystals[26] can have multiple photonic band gaps, but the size of the higher order band gaps greatly diminishes for finite thickness structures; in addition, in such planar structures, higher order band gaps are located above the light line, implying that the resonances at those frequencies would also have low quality factors (Q), resulting from the lack of total-internal reflection confinement. Band gaps for different polarizations (e.g. transverse magnetic (TM) and transverse electric (TE))[23, 27, 103, 106] can generate additional resonant modes; however, it is difficult to independently tune their frequencies, and TM resonances require relatively thick membranes that are more difficult to fabricate.

Recently[13], we proposed a crossed beam photonic crystal cavity suitable for nonlinear frequency conversion that allows at least two individually tunable resonances with a frequency separation larger than the size of the photonic bandgap in a single nanobeam. Here,

To summarize, for optimal performance in frequency conversion-based devices, a design must allow for:

- Independent tuning of individual cavity resonances with respect to each other through varying geometric parameters in the photonic crystal
- Large maximum separation between cavity frequencies
- High spatial overlap of electric fields in the nonlinear material
- High quality and small mode volume cavities
- Separate channels for waveguide coupling at each frequency
- Non-zero effective nonlinear tensor for the polarizations, material, and material crystal orientation of choice

In this chapter, we propose and experimentally demonstrate a crossed nanobeam photonic crystal cavity design that can satisfy these requirements allows at least two individually tunable resonances with a frequency separation larger than the size of the photonic bandgap in a single nanobeam. We also describe the experimental linear and nonlinear characterization of structures with resonances that are nearly degenerate with orthogonal polarization, as well as the design and linear characterization of structures with resonances separated by more than 500 nm.

7.2 Design of multiply resonant photonic crystals

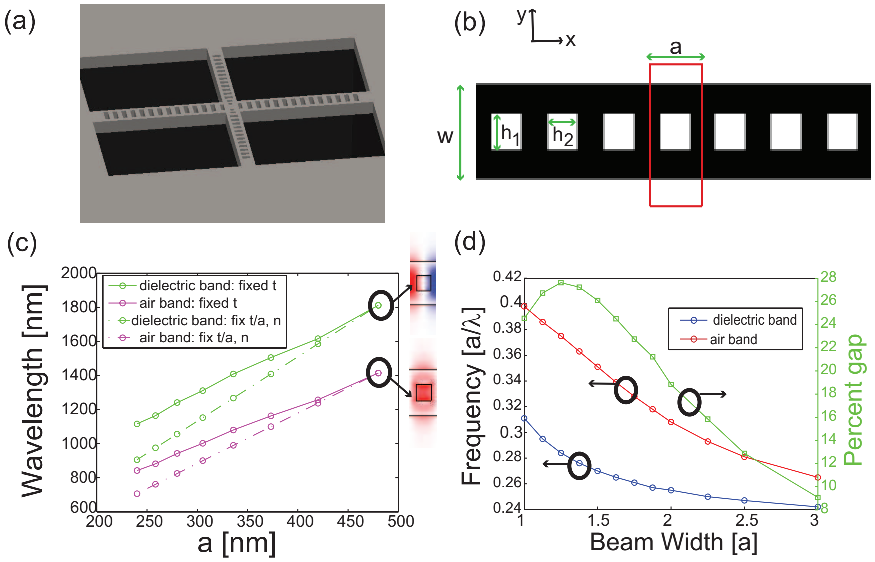

Figure 7.1: (a) Schematic illustration of multiply resonant orthogonal nanobeam cavity. (b) Illustration of photonic nanobeam. Red box shows unit cell, which is tiled periodically in the $\hat{x}$ direction. Parameters are periodicity a, width w, hole size h_x and h_y and thickness out-of-plane t (not shown). (c) Wavelengths of dielectric and air bands of GaAs nanobeam as lattice constant is varied. Parameters are w/a=1.65, h_1/w=0.6, h_2/a=0.5. Solid lines are plotted for t=160 nm (fixed absolute slab thickness) and wavelength-dependent index of refraction n; dotted lines are plotted for $t/a = 0.35$ (fixed relative slab thickness) and n=3.37. Field patterns of E_y at $k_x = \pi/a$ for dielectric (top) and air band (bottom) are indicated by black circles and arrows. (d) Normalized frequencies of dielectric and air bands (left axis) of GaAs nanobeam as beam width is varied. Parameters are h_1/w=0.6, h_2/a=0.5, t/a=0.35. Right axis shows change in size of photonic band gap with beam width.

An illustration of the design in shown in Fig. 7.1a. The basic element of our design is the nanobeam[38, 39, 35, 107, 34, 108], a 1D periodic photonic crystal waveguide clad in the other two directions by air, shown in Fig. 7.1b. A single unit cell of a single nanobeam, comprising a rectangular airhole with dimensions h_x and h_y in a high index dielectric slab of width w, is shown inside the red box (thickness t of the air-bridged membrane is out of the plane). The structure has periodicity a in the $\hat{x}$ direction; this periodicity produces a 1D TE photonic band gap with size determined by the difference in frequency between the first two bands (dielectric band and air band) at the wavevector $k_x = \pi/a$. We first investigate the periodicities required in a nanobeam structure to achieve different wavelength resonances using 3D simulations performed using plane wave expansion with supercell approach (MIT Photonic Bands (MPB))[109]. Fig. 7.1c plots the wavelengths of the dielectric and air bands obtained from simulations as a function of lattice constant a. Solid lines show wavelengths for fixed absolute thickness of the membrane and are calculated using the refractive index n of GaAs at each wavelength; dotted lines are calculated by scaling the result for wavelength 1550 nm (i.e. fixed t/a, fixed n). Because a real structure has a fixed membrane thickness, decreasing the periodicity in one beam relative to the other leads to larger relative thickness t/a, redshifting the wavelengths of the bands; therefore achieving resonances with relative frequency f_2/f_1 requires superlinear scaling of the feature size, e.g. $a_2/a_1 > f_2/f_1$, as shown by the divergence between solid and dotted lines. (There is a second less important contribution because refractive index increases for higher frequencies, from 3.37 to 3.53 for range plotted in Fig. 7.1c). Fig. 7.1d shows the frequencies of dielectric band and air band, as well the relative size of the band gap, as the width of the beam is changed.

A cavity is formed in each beam by introducing a central region with no holes (cavity length l) and tapering the lattice constant and hole size near the cavity region[34, 39]. In each beam, confinement along the periodic direction is provided by distributed Bragg reflection; confinement out of plane is provided by total internal reflection. Confinement in the in-plane direction orthogonal to the beam axis is provided by total internal reflection, and in the case of beams with overlapping photonic band gaps, also by distributed Bragg reflection (as in structures designed for minimizing crosstalk in waveguide intersections [110]). This structure allows nearly independent tuning of each resonant frequency by tuning the parameters (e.g. width, lattice constant, cavity length) of each beam. Additionally, the structure has natural channels for coupling through each beam to an access waveguide at each wavelength[111]. To optimize the design, parameters of cavity length, lattice constant (a), number of taper periods N, distance between holes in the taper region (a_i, $i = 1, 2, ...N$), hole size in the taper region (d_i, $i = 1, 2, ..., N$), and beam width (w) were varied in each beam. Fig. 7.2c shows the 3D finite difference time domain (FDTD)-simulated E_y field pattern for a resonance at 1.55 μm, with mode volume $0.35(\lambda/n)^3$ where n is the refractive index, and Q=19000, limited by loss in the vertical direction. Fig. 7.2d shows the field pattern of E_x for a resonance primarily localized by the vertical beam with wavelength 1.1 μm (also limited by vertical loss) and mode volume $0.47(\lambda/n)^3$. The shorter wavelength mode likely has a lower quality factor in part due to its narrower width than the horizontal beam and partly due to FDTD discretization error (12 points per period). Decreasing the vertical lattice constant further (10 points per lattice period) leads to resonances with separation of 574 nm (1550 nm and 976 nm).

Fig. 7.3a shows tuning of the quality factor of an individual resonance calculated by FDTD by adjusting the cavity length (a minimum cavity length is required to avoid overlap between the holes forming cavities in each beam). The resonant wavelength as well as quality factor of the beam can also be tuned by varying other parameters; Fig. 7.3b shows the change in resonant frequency and quality factor as width of the horizontal beam is varied. To study the overall effect f varying a single parameter, we plot a figure of merit (FOM) for nonlinear frequency conversion $FOM = Q_1 Q_2/\sqrt{V_1 V_2}$ in Fig. 7.3c (right axis), which is seen to depend primarily on Q_2. As mentioned previously, for large horizontal beamwidths, the quality factor of the higher frequency mode is limited by diffraction into the orthogonal beam; this principle is illustrated in Fig. 7.3(d) and Fig. 7.4.

For nonlinear frequency conversion applications, it is important for cavity field patterns to have large spatial overlap. Defining the nonlinear overlap, normalized to

1, as[27]

$$\gamma \equiv \frac{\epsilon_{NL} \int_{NL} dV \sum_{i,j,i\neq j} E_{1,i} E_{2,j}}{\sqrt{\int dV \epsilon |E_1|^2} \sqrt{\int dV \epsilon |E_2|^2}} \tag{7.1}$$

where NL indicates nonlinear material only, we calculate γ=0.02 for the structures shown in Fig. 7.2. This number could be increased to 0.07 by decreasing the number of taper periods from 5 to 3 to further localize the field to the central region; however, the quality factors are reduced to 1440 and 1077 respectively, although this could likely be increased by reoptimization of other parameters.

7.3 Degenerate frequency orthogonal polarization photonic crystal cavities

A cavity with orthogonally polarized resonances degenerate in frequency can be formed by using the same parameters for each beam. This could be used for applications such as coupling to spin states of embedded quantum emitters[112] or for building polarizaton entangled photon sources based on a bi-excitonic cascade from a single quantum dot[113, 114]. Figs. 7.5c, 7.5d show the field patterns from 3D finite difference time domain (FDTD) simulations for a doubly degenerate structure. The cavities also have several additional higher order modes the number of which is determined primarily by cavity length (two per beam for the structures shown in Fig. 7.5) with additional field pattern nodes. The design of a degenerate frequency cavity is shown in Fig. 7.5.

The value of γ for the degenerate cavity is 0.02. The value of γ for a single resonance of the degenerate structure overlapped with itself is 0.89 (i.e. γ is determined by the fraction of field in the nonlinear material), indicating the size of γ is limited by the amount of field concentrated in the central region. This overlap is smaller than that for TE_{00} and TM_{00} modes in a single nanobeam[27]; however, our design uses a thinner membrane which is easier to fabricate and can support larger frequency separations.

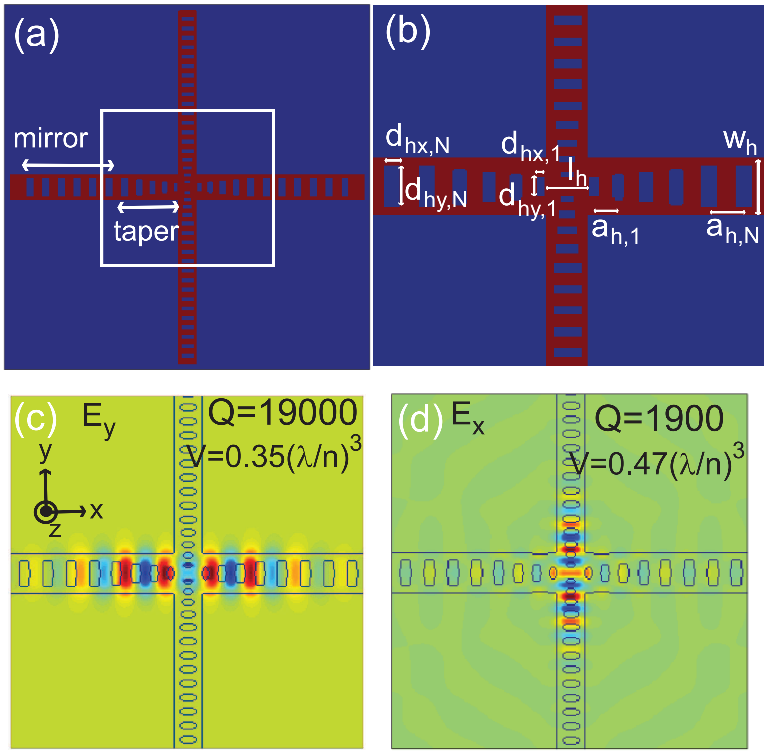

Figure 7.2: (a) Illustration of cavity design, showing intersecting orthogonal nanobeams with taper and mirror regions, as well as central cavity. (b) Detail of white box in (a). Parameters used to form resonance, shown for cavity in horizontal (subscript h) beam: l_h indicates cavity length; $d_{hx,N}$ and $d_{hy,N}$ indicate hole sizes in mirror region; $d_{hx,1}$ and $d_{hy,1}$ indicate hole sizes in first taper period; $a_{h,N}$ indicates periodicity in mirror region; $a_{h,1}$ indicates periodicity in first taper period, w_h indicates beam width. The corresponding parameters are similarly introduced for the vertical beam (with subscript v). The thickness of both beams (in the z direction) is t. Parameters are changed linearly inside the taper. (c) Field pattern of E_y for cavity mode localized by horizontal beam. Parameters are: $a_{h,N}$=453 nm, $a_{v,N}$=272 nm, $d_{hx,1}/d_{hx,N} = d_{hy,1}/d_{hy,N}$=0.5, $a_{h,1}/a_{h,N} = a_{v,1}/a_{v,N}$=0.7, $l_h/a_{h,N} = 1.2$, $l_v/a_{v,N}$=0.83, $w_h/a_{h,N}$=1.65, $w_v/a_{v,N}$=1.8, $d_{hy,N}/w_h = d_{vx,N}/w_v$=0.7, $d_{hx,N}/a_h = d_{vy,N}/a_{v,N}$=0.5, refractive index $n = 3.37$, with slab thickness $t/a_{h,N}$=0.35, N=5, and 6 mirror periods for both beams. Resonant wavelength is 1.55 μm with Q=19,000 and V=0.35$(\lambda/n)^3$. (d) Field pattern of E_x for cavity localized by vertical beam. $n = 3.46$ and other parameters same as in (c). Resonant wavelength is 1103 nm with Q=1900 and V=0.47$(\lambda/n)^3$.

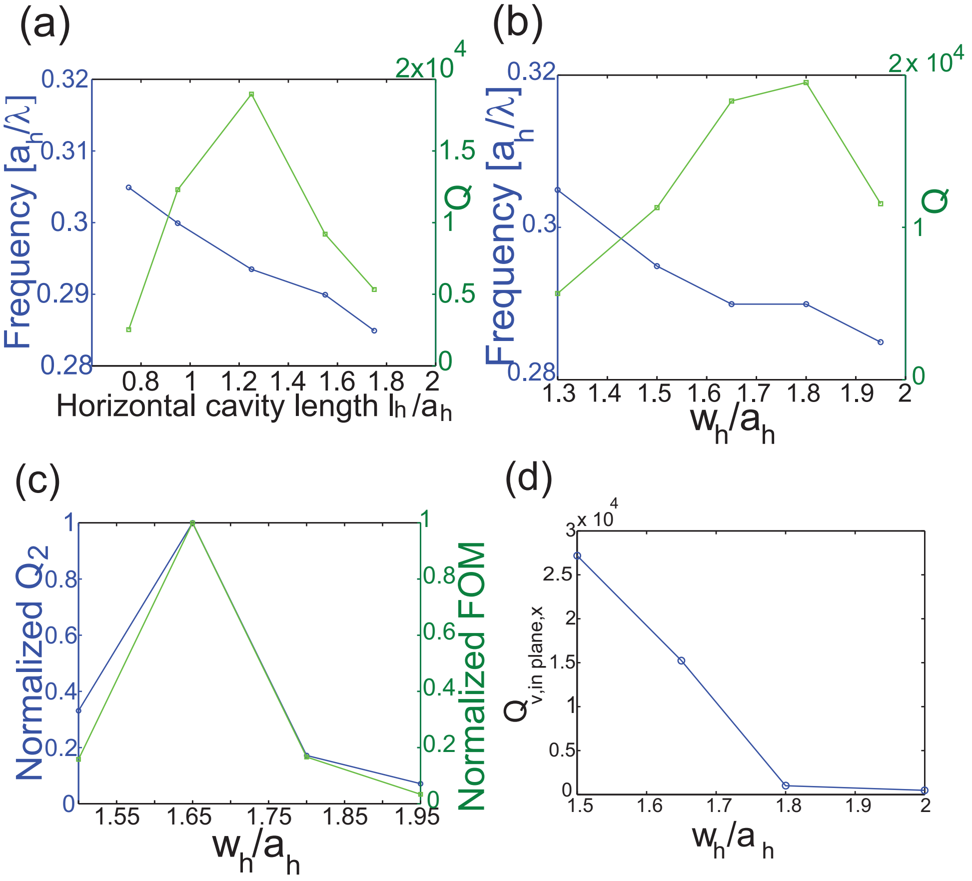

Figure 7.3: (a) Change in cavity resonant wavelength and Q in crossed beam structure for cavity mode localized in horizontal beam as cavity length is varied. Maximum Q occurs for l_h/a_h=1.25. (b) Change in horizontal (long wavelength) cavity resonant wavelength and Q in crossed beam structure as w_h is varied. (c) Change in vertical beam quality factor and frequency conversion figure of merit $FOM = Q_1Q_2/\sqrt{V_1V_2}$ as a function of w_h. (d) Change in in-plane quality factor in $\hat{x}$ direction (i.e. radiated power collected at x and -x edges of simulation space) for resonance localized by vertical beam as a function of w_h for structure shown in Fig. 7.2 (c)/(d).

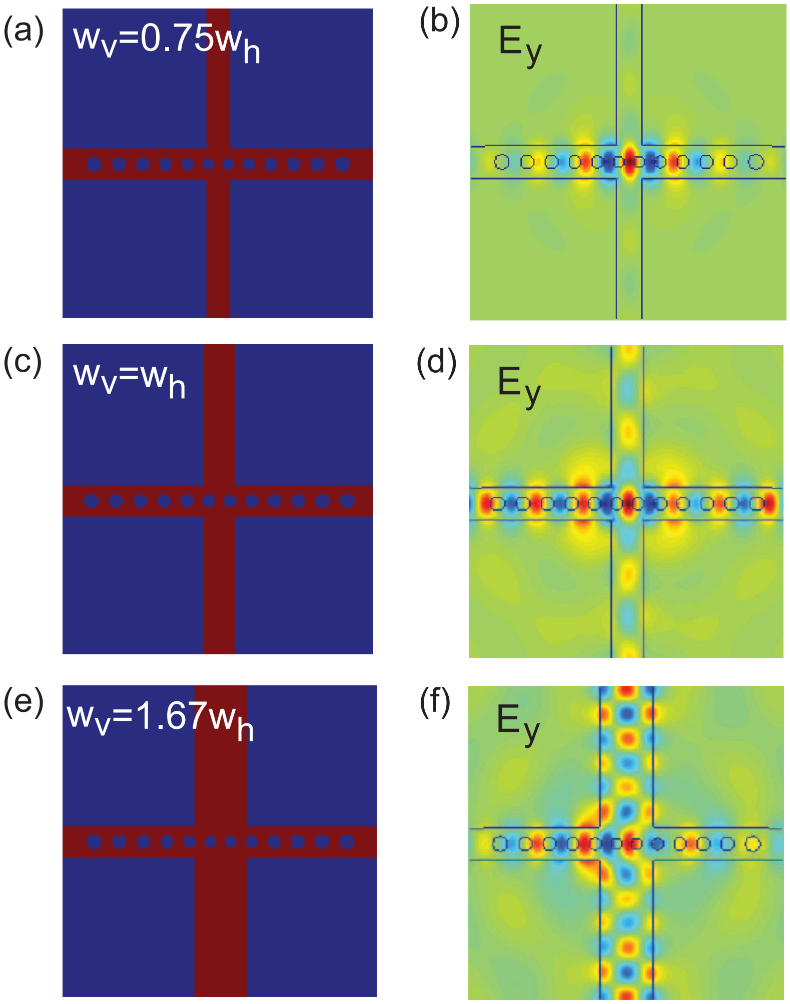

Figure 7.4: (a) Dielectric constant and (b) FDTD-simulated electric field E_y for nanobeam cavity crossed with orthogonal waveguide for $w_v = 0.75w_h$. (c)/(d) and (e)/(f) show the same for increasing width of the orthogonal waveguide, illustrating cavity confinement weakens as orthogonal waveguide width is increased. For (c)/(d), $w_v = w_h$, for (e)/(f) $w_v = 1.67w_h$.

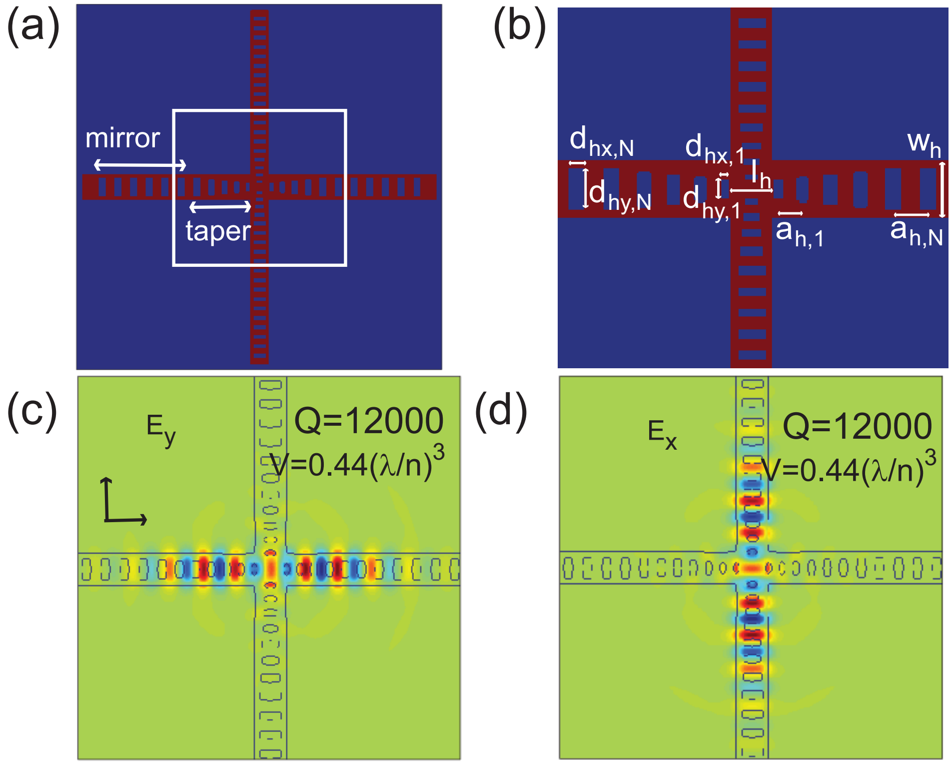

Figure 7.5: (a) Crossed nanobeam cavity design, showing intersecting orthogonal nanobeams with taper and mirror regions, as well as central cavity. (b) Detail of white box in (a). Parameters used to form resonance, shown for cavity in horizontal (subscript h) beam: l_h indicates cavity length; $d_{hx,N}$ and $d_{hy,N}$ indicate hole sizes in mirror region; $d_{hx,1}$ and $d_{hy,1}$ indicate hole sizes in first taper period; $a_{h,N}$ indicates periodicity in mirror region; $a_{h,1}$ indicates periodicity in first taper period, w_h indicates beam width. The corresponding parameters are similarly introduced for the vertical beam (with subscript v). The thickness of both beams (in the z direction) is t. Parameters are changed linearly inside the taper. (c) 3D FDTD simulation of field pattern of E_y for cavity localized in horizontal beam by tapering hole dimensions and lattice constant in central region. Parameters are: $a_{h,N} = a_{v,N}$=449 nm, $d_{hx,1}/d_{hx,N} = d_{hy,1}/d_{hy,N}$=0.5, $a_{h,1}/a_{h,N} = a_{v,1}/a_{v,N}$=0.7, $l_h/a_{h,N} = l_v/a_{v,N} = 1.4$, $w_h/a_{h,N} = w_v/a_{v,N}$=1.65, $d_{hy,N}/w_h = d_{vx,N}/w_v$=0.7, $d_{hx,N}/a_h = d_{vy,N}/a_{v,N}$=0.5, refractive index $n = 3.37$, with slab thickness $t/a_{h,N}$=0.35, N=8, and 6 mirror periods for both beams. Resonant wavelength is 1.55 μm with Q=12,000 and V=0.44$(\lambda/n)^3$. (d) Field pattern of E_x for cavity localized in vertical beam. Parameters are same as in (c).

7.3.1 Linear characterization of cavity resonances

We now present characterization of cavities with nearly degenerate resonant frequencies. A scanning electron microscope image of structure fabricated in GaAs is shown in Fig. 7.6a. The structures are defined by e-beam lithography and dry etching, as well as wet etching of a sacrificial AlGaAs layer underneath the 164 nm thick GaAs membrane. To characterize the resonant frequencies of the structures, we measure reflectivity, using vertical incidence through an objective lens and free space coupling, in the cross-polarized configuration using a tungsten halogen lamp as a broadband light source[8]. The principle of the measurement is illustrated in Fig. 7.6b. The input and measurement polarizations are orthogonal; the cavity polarization is oriented 45 degrees to both output and input. The cavity acts as a frequency-selective polarization rotator, filtering light at the frequencies of the cavity resonances, resulting in a high-signal to noise measurement of the cavity reflectivity from which the quality factor can be extracted. The result of this measurement for the structure in Fig. 7.6a is shown in Fig. 7.6c. There are two resonances visible at 1571.2 nm (Q=4700) and 1573.9 nm (Q=7200). The difference between the frequencies of the resonances is due to fabrication imperfections; improving fabrication or employing local tuning[114, 115, 116] could assist in yielding perfectly degenerate resonances. Quality factors are extracted by fitting the measured data to the sum of two Fano lineshapes[117], plus linear background (to account for the measured background from the white light source).

7.3.2 Nonlinear characterization of nearly frequency degenerate cavity resonances

This cross-polarized configuration, however, cannot easily distinguish between cavities with vertical and horizontal polarizations, and also cannot resolve resonances with frequencies separated by less than a linewidth. To more sensitively measure cavity resonances, we use intracavity second harmonic generation[9, 104]. This allows us to absolutely determine the far-field polarization of the cavity, since second harmonic generation is maximized when incident light is aligned to the polarization of

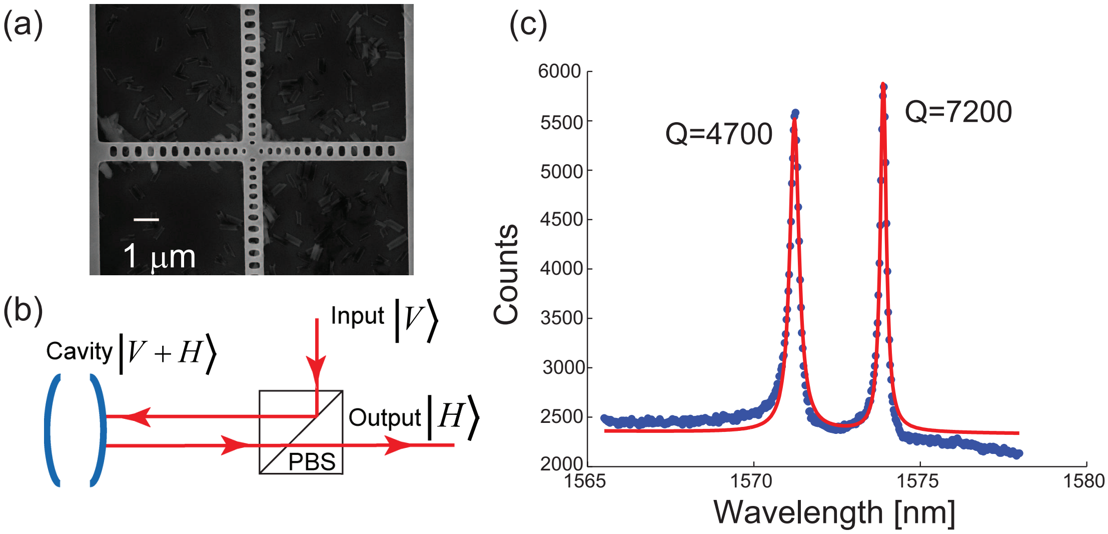

Figure 7.6: (a) Scanning electron microscope image of crossbeam structures with identical parameters in both beams. Structures are fabricated by e-beam lithography, dry etching, and wet etching. (b) Experimental setup for cross-polarized reflectivity measurements to characterize cavity resonances. PBS indicates polarizing beamsplitter. Cavity polarization is oriented 45 degrees ($|H+V\rangle$) from orthogonal input ($|V\rangle$) and measurement ($|H\rangle$) polarizations. (c) Cross-polarized reflectivity measurement of structure in (a), showing two resonances at 1571.2 nm (Q=4700) and 1573.9 nm (Q=7200). Solid line indicates fit to sum of two Fano lineshapes.

the cavity. Additionally, because the measured lineshape from the second harmonic is proportional to the square of the lineshape from the cavity, we can more easily distinguish cavities separated by small differences in frequency. A second harmonic measurement of a different structure with nearly degenerate resonances in shown in Fig. 7.7. Fig. 7.7a shows the second harmonic counts measured for three different incident laser polarizations as the laser wavelength is varied. The angle of alignment between input polarization and the polarization of each cavity mode determines the fraction of power coupled into the cavity, and accordingly affects the magnitude of second harmonic generated. The intensity of second harmonic generation for each mode also depends on the free space coupling efficiency, quality factor of the mode, spatial overlap of fundamental and second harmonic fields, and detuning of laser wavelength from the cavity resonance[9]. Two modes with orthogonal polarization (with resonant wavelengths 1541.75 nm and 1542.1 nm), as expected, are clearly visible. To further illustrate this, we scan additional incident polarizations and wavelengths, as shown in Figs. 7.7b, 7.7c. Fig. 7.7c shows 2D slices at three incident laser wavelengths. The red lines show fits for two resonances with polarization separated by exactly 90 degrees, in good agreement with the measured data.

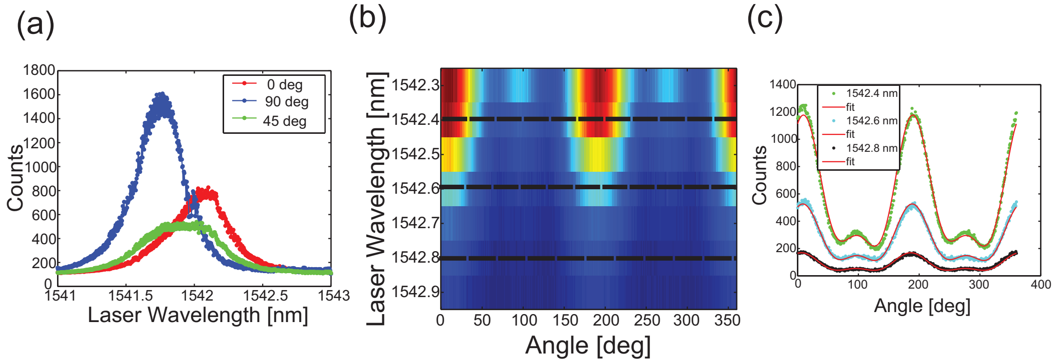

Figure 7.7: (a) Second harmonic characterization of structure with two resonances nearly degenerate in frequency as a function of laser wavelength for 3 polarizations. Two modes with orthogonal polarization are visible. (b) Second harmonic intensity as a function of incident laser polarization. Vertical axis indicates wavelength of laser; horizontal axis indicates angle of polarization. Color indicates second harmonic intensity. Dotted horizontal lines indicate traces in (c). (c) Line plots of second harmonic generation measured at different polarizations for three laser wavelengths shown in (b). Red lines indicate fits for two cavity modes with polarizations separated by exactly 90 degrees.

We also perform nonlinear mixing with two resonant modes detuned in frequency. Fig. 7.8 shows sum-frequency generation performed in a structure with resonances at 1552.8 nm and 1558.9 nm (selected to have two resonances overlapping with the high power range of our tunable lasers and large enough frequency separation to observe the SFG peak). The central sum-frequency peak is smaller due to the smaller spatial overlap between the two modes than with a single mode. There is no cavity resonance at either the second harmonic or sum frequency.

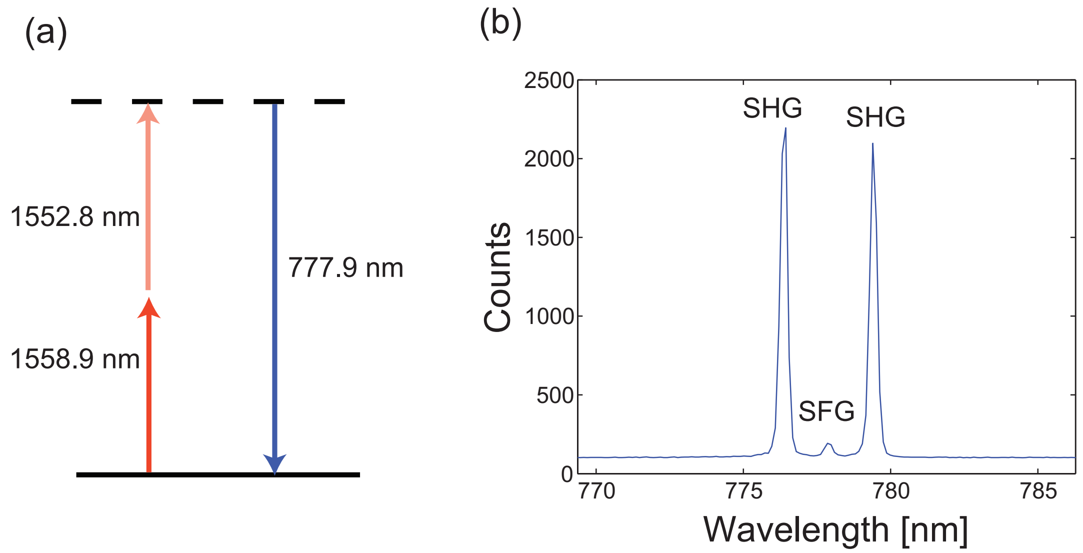

Figure 7.8: (a) Schematic of sum frequency generation. Light from two CW lasers is coupled into two cavity resonances at 1552.8 nm and 1558.9 nm. Nonlinear frequency conversion produces light at the second harmonic frequencies of each laser, as well as at the sum frequency, 777.9 nm. (b) Sum-frequency generation from structure with resonances as indicated in (a).

7.4 Fabrication and characterization of multiply resonant photonic crystals with large frequency separation

A scanning electron microscope (SEM) image of a fabricated structure is shown in Fig. 7.9a. The structures are defined by e-beam lithography and dry etching, as well as wet etching of a sacrificial AlGaAs layer underneath the 164 nm thick GaAs membrane. To compare the experimental structure with the proposed design, we simulate the fabricated structure by converting the SEM image to the binary refractive indices of air and GaAs[118]. The thresholded SEM image used for simulation is shown in Fig. 7.9b. Figs. 7.9c, 7.9d show the simulated electric field for the two resonances of the fabricated structure, with expected resonances at 1477 nm (Q=4100) and 1043 nm (Q=540). Finally, we experimentally characterize our design by performing a reflectivity measurement in the cross-polarized configuration[8] (Figs. 7.9e, 7.9f) using light from a tungsten halogen lamp which is linearly polarized using a Glan Thompson polarizer and polarizing beamsplitter. The cavity is oriented at 45 degrees to both the polarization of the incident light and orthogonal polarization used for measurement. We measure quality factors of 6600 at 1482.7 nm and 1000 at 1101 nm. Differences between simulation of fabricated structures and experimentally measured resonances are most likely due to computational error in binary thresholding of the refractive index. Experimentally, the largest separation between resonances we have measured is 506 nm.

Fig. 7.10 shows cross-polarized reflectivity measurements using a broadband source of structures with resonances at 1546.6 nm (Q=1600) and 1023 nm (Q=500), a frequency separation of 523.6 nm. We believe the experimental Q factors are limited by fabrication inaccuracies caused by the small feature size of the central holes in the vertical beam, which are located in regions of high field for both resonances. We could not perform nonlinear characterization of these structures due to lack of availability of a laser at 1023 nm.

7.5 Improving the crossbeam frequency conversion platform

For highly efficient three wave mixing, it would be desirable to have all three frequencies confined by cavity modes. This could be achieved by additionally using a higher order mode in one beam. However, all cavity resonances in our design have electric field primarily in plane (TE), while nonlinear frequency conversion in III-V semiconductors grown on (100)-oriented wafers requires at least one frequency to have out of plane (TM) polarization (because the only non-zero elements of the bulk $\chi^{(2)}_{ijk}$ have $i \neq j \neq k$[9]). This can be circumvented by using a wafer with different crystal orientation such as (111)[119, 26] so that the effective $\chi^{(2)}$ tensor is rotated to have more non-zero elements. Fig. 7.11 shows a concept illustration of highly efficient doubly resonant second harmonic generation using the crossbeam structure.

Our design is also interesting for integration with single semiconductor emitters, which is important for creating quantum photonic interfaces between different quantum emitters and telecommunications wavelength. As described in the previous chapter[12], we demonstrated second harmonic excitation of a InAs single quantum dot emitting at 900 nm, creating a fast single photon source triggered at telecommunication wavelengths (triggered single photons at 100 MHz, with nonclassical statistics visible at 300 MHz) . The speed of that source could be improved by using a second cavity resonance, as in our crossed beam design, to enhance the spontaneous emission rate of the quantum dot through the Purcell effect[120], with possible speeds exceeding 1 GHz. Finally, our design is also promising for intracavity frequency conversion of single photons from an integrated quantum emitter[103].

7.6 Conclusions

In conclusion, we have proposed and demonstrated the design of a photonic crystal cavity with multiple nearly independent resonances, with experimentally measured Q>1000 for both resonances. We demonstrate cavities with nearly-degenerate frequencies, as well as frequencies separated by more than 500 nm, which we characterize by linear and nonlinear spectroscopy. Finally, we propose extensions of this work to allow high efficiency frequency conversion, which might be used in conjunction with integrated single emitters. The design also features independent waveguide channels for two resonances, which facilitates their spatial separation, as is desirable in many applications. Our design is promising for resonantly enhancing on-chip nonlinear frequency interactions, such as stimulated Raman scattering (which could be achieved in semiconductors such as GaAs or Si by a slight detuning between the parameters of the two beams) and sum/difference frequency generation.

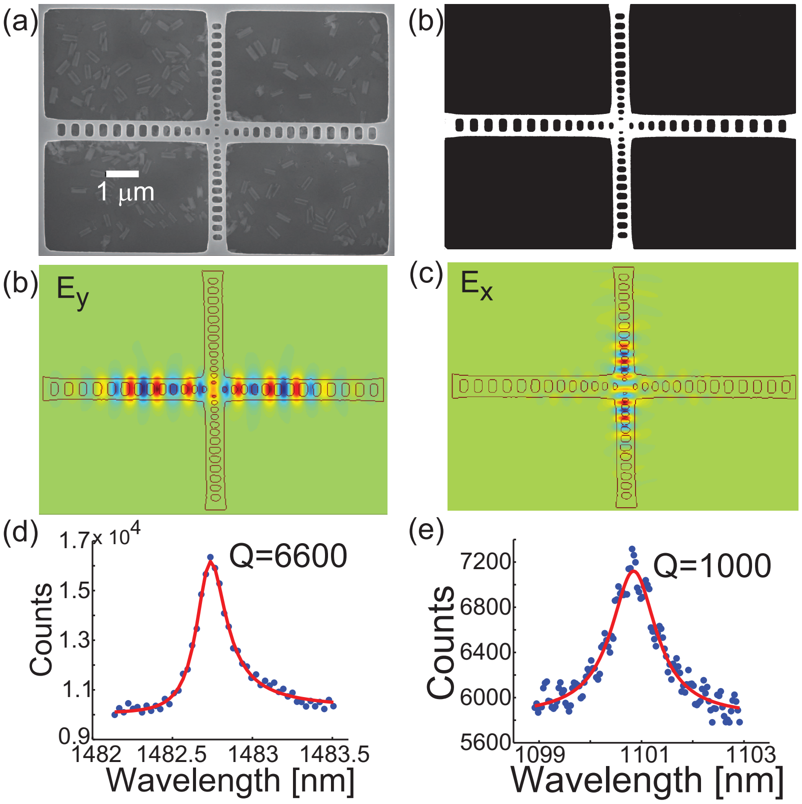

Figure 7.9: (a) SEM image of cross-beam structures fabricated in 164 nm thick GaAs membrane with $a_{h,N}$=470 nm and $a_{v,N}$=320 nm fabricated in 164 nm membrane. (b) Thresholded binary image of SEM used for simulating fabricated structure. (c) FDTD simulation of E_y for cavity resonance at 1477 nm. (d) Simulated E_x for cavity resonance at 1043 nm. (e) Reflectivity measurement of cavity mode at 1482.7 nm with Q=6600. (f) Reflectivity measurement of cavity resonance at 1101 nm with Q=1000.

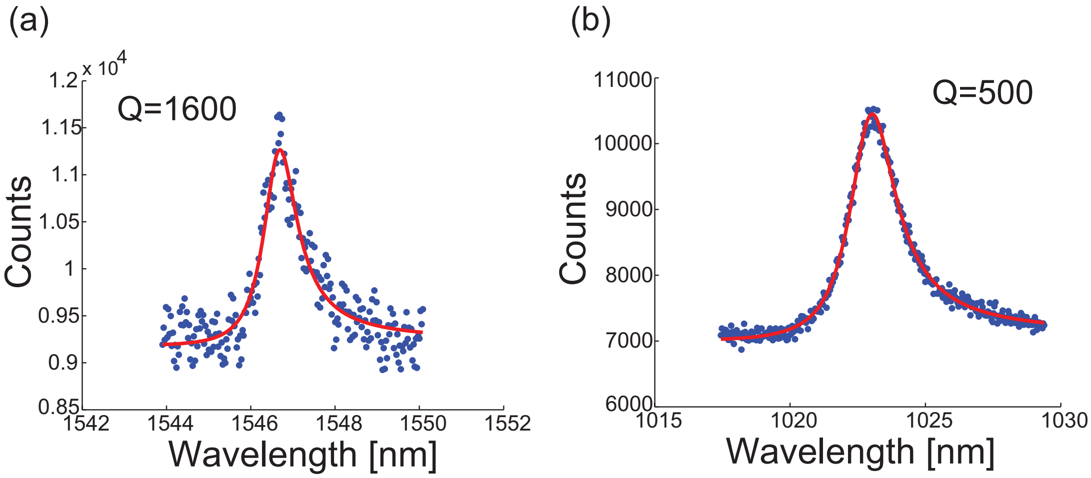

Figure 7.10: Cross-polarized reflectivity of crossbeam structure with resonances separated by 523 nm. (a) Resonance at 1546.6 nm (Q=1600). (b) Resonance at 1023 nm (Q=500).

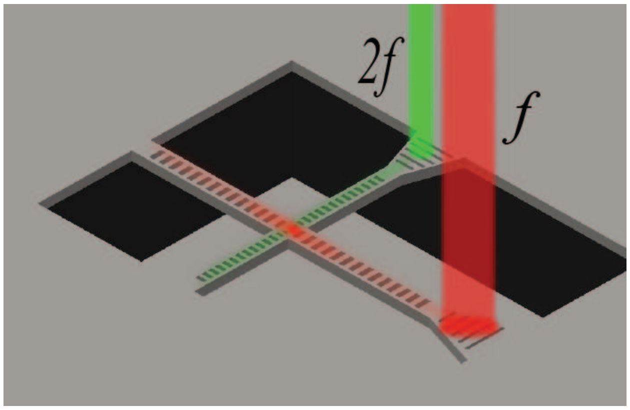

Figure 7.11: Concept illustration of doubly resonant second harmonic generation in photonic crystal crossbeam nanocavity. Incident light (red) is coupled into the structure via a grating, transmitted to the cavity, frequency converted, and outcoupled through a separate grating (green).

Chapter 8

Visible quantum emitters and GaP photonic crystal cavities

This chapter describes two such systems and their properties when coupled to GaP photonic crystal cavities, described in Chap. 4. The high refractive index of the material enables a large photonic band gap and cavities with high quality factor, while the large electronic band gap prevents absorption in the near-IR and part of the visible. The first system consists of dinaphthoquaterrylene diimide (DNQDI) molecules embedded in a PMMA thin film. This film can then be deposited on a GaP photonic crystal to couple molecules to cavity, and e-beam lithography techniques can be used to localize the molecule to the cavity spatial position. The second system is InGaAs/GaP quantum dots grown by molecular beam epitaxy; when coupled to a photonic crystal, the outcoupling is sufficiently enhanced to allow the observation of narrow spectral lines consisting of single quantum dot emission.

Beyond this thesis, the author has also collaborated on relevant work with other visible quantum emitters and GaP photonic crystals including nitrogen vacancy centers in nanocrystals [80], Cs atoms[121], and InP/InGaP quantum dots.

8.1 Motivation

Coupled photonic crystal cavity-emitter systems studied so far are primarily based on gallium arsenide and silicon materials, which absorb strongly at wavelengths shorter than the electronic band gap of the material. This precludes the use of emitters atoms, molecules, defect centers in crystals such as the nitrogen vacancy (NV^-) center, as well as many quantum dot systems having room temperature confinement, which typically have resonances at visible wavelengths. Some of these emitters have particular advantages for devices resulting from long electronic and spin coherence times and room temperature coherence. Second, emitters at these wavelengths are easily integrated with the frequency conversion techniques describing earlier, as the frequency of these emitters' transitions can be accessed by the sum frequency of telecom-wavelength lasers. Additionally, hybrid systems in which the emitter (such as free-space atoms or molecules embedded in thin fims) and cavity exist in separate materials allow deterministic positing of emitter with respect to cavity, which is not possible for self-assembled quantum dots grown by molecular beam epitaxy.

8.2 Lithographic positioning of molecules on high-Q photonic crystal cavities

As described previously in this thesis, photonic crystal nanocavities have been used to demonstrate nanoscale on-chip devices and to probe fundamental quantum interactions between light and matter[45, 62, 122, 41]. Experiments in this regime, however, are limited by the precision with which cavity and emitters can be spatially aligned and by the spectral range of emitters that can be coupled to cavity. Emitters are most often distributed randomly in the photonic crystal slab, and spatial alignment to the photonic crystal cavity occurs by chance. Recently, several techniques have been developed to position emitters with respect to cavities: these techniques rely primarily on either a mechanical transfer process to bring an emitter to the surface of the cavity[123, 124] or the fabrication of a cavity at the location of a previously detected emitter[125, 126]. Neither method is easily scalable to arrays of cavities and emitters, nor achievable with conventional semiconductor fabrication processes. In this section, we demonstrate cavities with quality factors above 10,000 at wavelengths compatible with near-IR fluorophores and show that we can selectively position these molecules on top of a nanocavity using conventional lithography techniques.

8.2.1 Fabrication of cavity and thin film of molecules

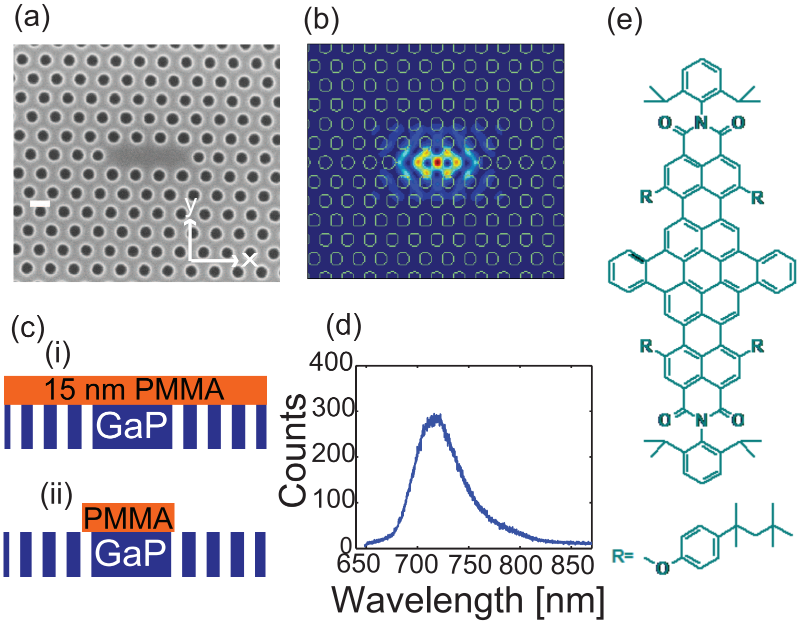

Figure 8.1: (a) SEM image of a fabricated photonic crystal cavity in GaP. Scale bar indicates 200 nm. (b) FDTD simulation of electric field intensity of the fundamental cavity mode. The mode is primarily $\hat{y}$-polarized (c) Schematic illustrating coupling of molecule to cavity. (i) DNQDI/PMMA is deposited over the entire structure. (ii) DNQDI/PMMA is lithographically defined on cavity region. (d) Bulk photoluminescence spectrum of DNQDI when excited with a 633 nm HeNe laser. The molecule has a peak in its absorption at this excitation wavelength. (e) Chemical structure of DNQDI molecule.

The cavity is a linear three-hole defect (L3)[33] fabricated in a 125-nm gallium phosphide membrane grown by gas-source molecular beam epitaxy. A scanning electron microscope (SEM) image of a fabricated cavity and the simulated electric field intensity of the fundamental high-Q cavity mode are shown in Fig. 8.1(a) and 8.1(b). Cavities are fabricated as described in Chap. 4. The molecule we use is dinaphthoquaterrylene diimide (DNQDI)[127], which was chosen for its broadband emission over the desired wavelength range (700-850 nm), good photostability, and high photoluminescence (PL) quantum yield (40%). The structure of the molecule and its emission spectrum are shown in Fig. 8.1. To couple DNQDI to photonic crystal cavities (Fig. 1(c)), the molecule was dissolved into a solution of 1% poly(methylmethacrylate) (PMMA) in distilled toluene. In standard lithographic processing, this solution is then spun onto a surface, leaving behind a smooth, thin film of dye-doped resist. However, spinning onto an uneven surface, such as a photonic crystal membrane, causes unwanted aggregation of the dye-doped PMMA. Instead, the solution was float-coated [128], whereby the photonic crystal sample is submerged into a water bath and a single drop of the dye-doped PMMA in toluene solution is dropped onto the surface of the water bath. The drop quickly disperses across the surface leaving a locally uniform layer of hydrophobic dye-doped resist floating on top of the water bath. The water is then pipetted away, allowing the PMMA layer to fall on top of the photonic crystal sample. The sample is baked at 90°C for 30 minutes to ensure that all the water is fully evaporated. The concentration of DNQDI in the PMMA layer is approximately 5 molecules/100 nm^2.

8.2.2 Characterization of cavity resonances

We first characterize cavities passively prior to depositing molecules. We probe cavity resonances using cross-polarized normal-incidence reflectivity, described in Ch. 4 with a tungsten halogen white light source[8]. The cross-polarization configuration is used to obtain a sufficient signal-to-noise ratio to observe the cavity resonance above the reflected background uncoupled to the cavity. A typical reflectivity spectrum is shown in Fig. 8.2(a), showing the multiple resonances of the L3 cavity; the fundamental mode is denoted with a black box. The spectrum of the fundamental mode (Fig. 8.2(b)) is fit to a Lorentzian, giving a quality factor of 10,000. (The improvement in quality factor from [8] is due to better fabrication.) After depositing the molecules over the entire structure, we measure photoluminescence of the molecule (Fig. 8.2(c)) using a 633-nm helium-neon excitation laser in a confocal microscope setup. Above the broad emission from molecules not coupled to the cavity, we observe sharp polarized resonances identical to those in our reflectivity measurements, demonstrating the molecules are coupled to the cavity modes. The quality factor of the fundamental mode is measured to be 10,000, indicating that deposition of molecules onto the membrane does not degrade the properties of the cavity, in agreement with finite difference time domain simulations for a thin (<40 nm-thick) layer of PMMA. After deposition of molecules, we observe a small (several nm) redshift in the cavity resonance, as expected from simulations. With no DNQDI/PMMA present, only background counts are detectable over the entire spectral range. We vary the spatial periodicity of the photonic crystal holes and hole radius to tune the fundamental cavity resonance through the photoluminescence spectrum of the molecule. We measure high cavity quality factors up to 12,000 via photoluminescence (Fig. 8.2(d)) across a range of more than 100 nm, from 735 nm-860 nm. The cavity Q is higher at longer wavelengths, where we fabricate most of our cavities, as fabrication imperfections are reduced because the feature size is larger. Small differences in cavity Q between reflectivity and photoluminescence measurements (Fig. 8.2(d)) are primarily due to fit error.

8.2.3 Lithographic localization of molecules to cavity region

Since the molecules are doped into PMMA, an electron-beam lithography resist, it is straightforward to selectivity expose and develop the resist using e-beam lithography[129] so molecules and PMMA remain only at the location of the photonic crystal cavity (Fig. 8.1(c)). The size of the unexposed region at the center of the photonic crystal cavity is approximately 700 nm by 400 nm. While float coating deposits resist uniformly over a small region, PMMA thickness variations were observed from one coating to the next, so electron beam doses were varied for different cavities on one sample. Fig. 8.3(a) shows a scanning confocal image of photoluminescence from a photonic crystal cavity coated with DNQDI-doped PMMA. The photoluminescence

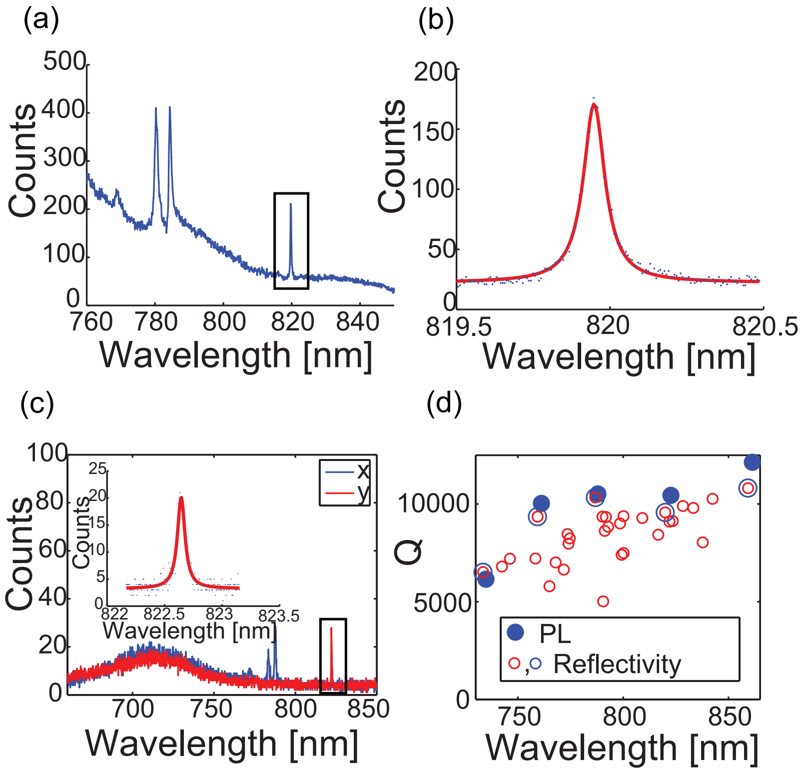

Figure 8.2: (a) Cross-polarized reflectivity measurement of a cavity. Box indicates fundamental cavity mode. (b) Reflectivity spectrum of high quality factor fundamental cavity mode (box in (a)). Spectrum shows additional peaks at shorter wavelengths from higher order cavity modes. Solid line shows Lorentzian fit with quality factor 10,000. (c) Photoluminescence collected from the same photonic crystal cavity in (a-b) after molecules are deposited on cavity. x-polarized emission is shown in blue; y-polarized emission is shown in red. Inset: PL measurement of fundamental cavity mode (black box). Line indicates Lorentzian fit with Q=10,000. (d) Quality factors measured from reflectivity before molecule deposition and photoluminescence after molecule deposition from the high Q cavity mode for structures with lattice constant a and hole radius r/a tuned so that the fundamental cavity resonance shifts across the photoluminescence spectrum of the molecule. Blue open circles indicate reflectivity measurements for the cavities that were also measured in PL (blue closed circles).

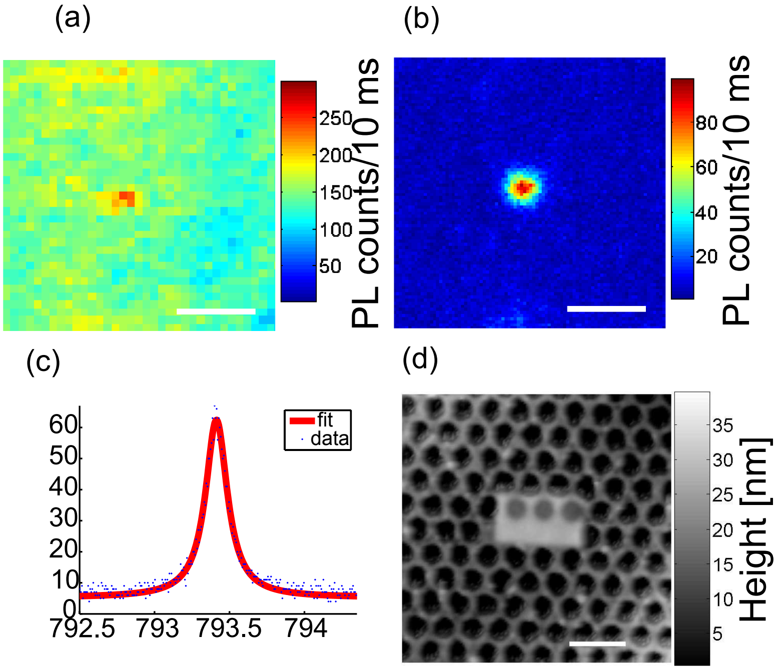

Figure 8.3: (a) Scanning confocal image of photoluminescence from DNQDI doped PMMA float-coated onto a photonic crystal membrane. Pixel size is 200 nm and scale bar indicates 2 μm. (b) Scanning confocal image of DNQDI PL after electron beam lithography is used to remove all molecules, except for the ones coating the cavity region at the center. The same imaging laser power as in (a) was used. Pixel size is 80 nm and scale bar indicates 2 μm. (c) PL spectrum from the fundamental mode of photonic crystal cavity after selective removal of molecules by e-beam lithography. (d) Atomic force microscopy image showing localization of DNQDI-doped PMMA to the cavity region. PMMA thickness is 12 nm. Scale bar indicates 500 nm.

is flat to within 3.5%, with slightly more emission from the cavity region, likely a result of enhanced outcoupling from molecules coupled to the cavity mode. Fig. 8.3(b) shows photoluminescence from the same cavity, measured with the same excitation power, after electron beam exposure and removal of the resist surrounding the cavity. There is still strong emission, though diminished by the e-beam process, from the cavity region, but there is no emission from the nearby areas, so the contrast is much larger. Fig. 8.3(c) shows a PL spectrum (Q=4500) measured on the same cavity after localization of the resist to the cavity, demonstrating that molecules are spectrally coupled to photonic crystal cavity. An atomic force microscope image (Fig. 8.3d) confirms that DNQDI-doped PMMA is localized to the cavity and is 12 nm in height. The AFM image shows a misalignment of approximately 300 nm between the cavity region and the lithography defined DNQDI/PMMA region. With optimization of the overlay process, it should be possible to reduce this error to less than 50 nm.

8.2.4 Low temperature spectroscopy of DNQDI

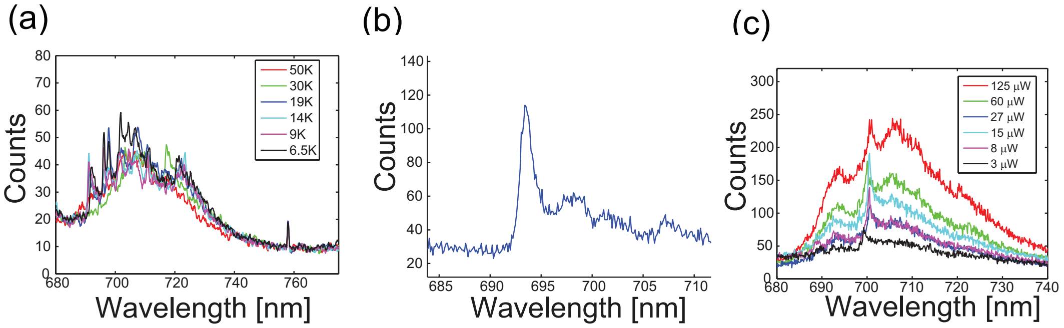

Figure 8.4: (a) DNQDI photoluminescence as a function of temperature. For temperatures below 50K, narrow lines appear. (b) Individual spectral features qualitatively match the expected emission from a zero phonon line and phonon wing. As much as 30% of molecule emission is measured to come from the narrow spectral line.

We also investigated the low temperature spectrum of the DNQDI molecules uncoupled to a cavity to assess the feasibility of achieving a stronger coupling between cavity and molecule. At room temperature, the linewidth of the molecule emission is increased due to phonons, resulting in a large emission bandwidth. On the other hand, if the spectral linewidth can be reduced to the cavity linewidth, the coupling can be enhanced if the molecule and cavity resonant frequencies are matched, enabling an increase in the fraction of emission into a particular spectral transition[130] and speedup of the emitter spontaneous emission rate [120]. If the coupling is sufficiently large, the strong coupling regime can be reached[62] where emitter and cavity form mixed eigenstates. Because of the rotational and vibrational structure of molecules, for coherent interactions, it is also important to access the zero phonon line of the molecule, which we hope to observe through these temperature-dependent studies. The results of these measurements are shown in Fig. 8.4. At low temperatures (<50K), we indeed observe narrow spectral lines (Fig. 8.4(a)). It is also possible in some cases to resolve individual narrow lines that appear to have the shape of a zero phonon line and phonon wing (Fig. 8.4(b)). In this case, it appears as much as 30% of the emission may come from the zero phonon line. We measure narrowest linewidths to be of the order of 100 Ghz at 10K, as expected for a molecule embedded in a polymer film [131]. We also observe power broadening of the spectral lines (Fig. 8.4(c)).

8.2.5 Spin-grown crystalline films containing DNQDI

To attempt to further narrow the linewidth[131], minimize spectral diffusion [132], and align the molecule polarization, we also investigated embedding the DNQDI molecules into spin-grown crystals [133, 134] tens microns in lateral extent and hundreds of nm in height. To form these crystals, we added a small amount of DNQDI in toluene to a 1% p-terphenyl (PT) in toluene solution. We investigated a range of experimental parameters including spin speed (500-3000 rpm), and substrate (Si, glass, gold, GaP). We also studied crystal height by AFM (Fig. 8.6(b)), as well as the crystal luminescence (Fig. 8.6).

The large variation in crystals formed (Figs. 8.5, 8.6) made this technique difficult to combine with nanophotonic structures.

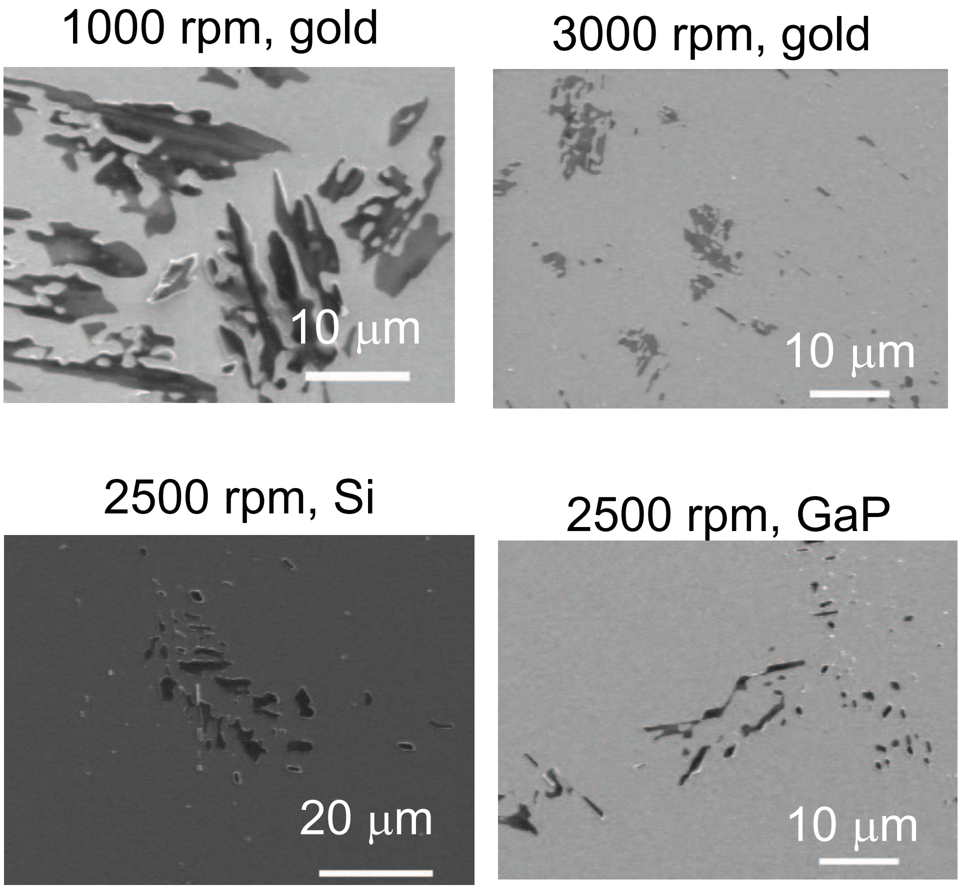

1000 rpm, gold

3000 rpm, gold

2500 rpm, Si

2500 rpm, GaP

Figure 8.5: Spin-grown thin-film crystals of DNQDI molecules on different substrates formed by using different spin speeds, as indicated. Scale bars all indicate 10 μm.

8.3 Photoluminescence from In$_{0.5}$Ga$_{0.5}$As/GaP quantum dots coupled to photonic crystal cavities

Semiconductor quantum dot (QD) emitters grown in gallium phosphide are important for both classical optoelectronic and quantum applications. The close match between the lattice constants of GaP and Si (0.37% at 300K [135]) is promising for monolithic integration with silicon[135, 136, 137], and the large electronic band gap of GaP allows light emission at visible wavelengths. Single quantum dots (QDs) at

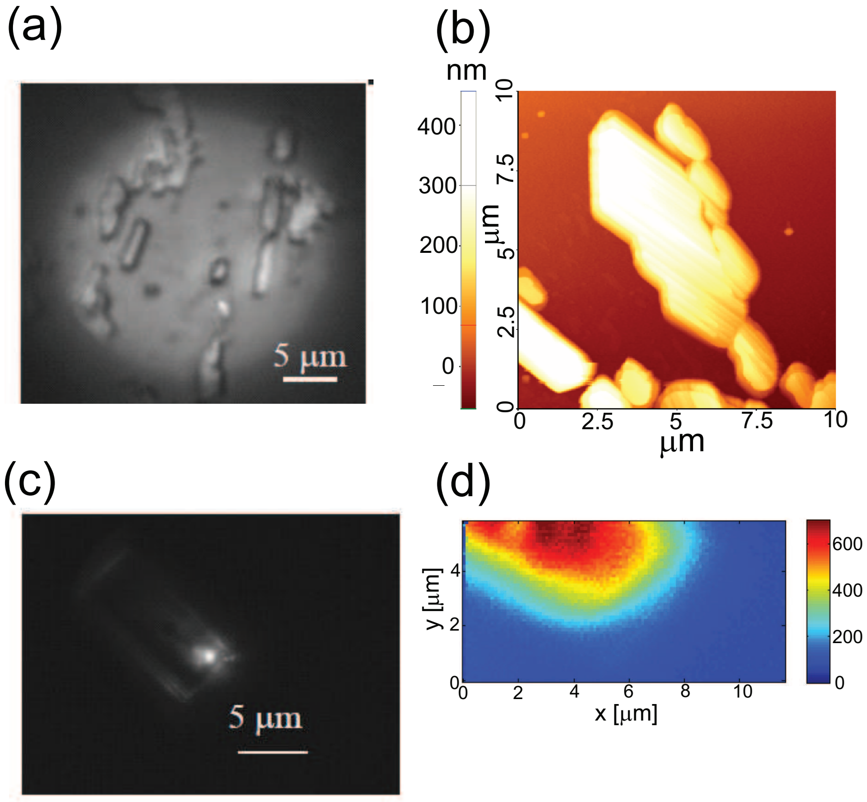

Figure 8.6: (a) Optical microscope image of a crystal formed by spinning at 3000 rpm on a glass substrate. (b) AFM image of crystal spun at 2500 rpm on glass, indicating crystal height of few hundred nm and lateral size of ≈1 μm. (c) Photoluminescence from a spun crystal excited by a 633 nm HeNe laser. (d) Confocal photoluminescence scan of region of crystal in (c) measured by a Si single photon counter. c-axis indicates photoluminescence counts.

visible wavelengths are beneficial for quantum applications since Si avalanche photodiodes (APDs) have maximum quantum efficiency in the red part of spectrum; additionally, emission in this part of the spectrum can be frequency downconverted to telecommunications wavelengths using readily available lasers[138, 139].

Quantum dots emitting in the red have been extensively studied over the past decade in materials systems including InP/InGaP[140, 141, 142, 143], InP/GaP[144, 145], InP/AlGaInP[146, 147], GaInP/GaP[148], InAs/GaP[149], and AlGaInP/GaP[150]. Of these systems, clear single quantum dots with narrow emission lines exhibiting antibunching have been observed only in the InP/InGaP and InP/AlGaInP systems. GaP-based materials, by contrast, allow either monolithic integration with Si or growth on a non-absorbing GaP substrate (due to the large indirect electronic band gap); additionally, the stronger second order optical nonlinearity of GaP compared to InGaP is preferable for on-chip frequency downconversion to telecom wavelengths. Recently[79], low temperature emission (80K) was measured from $In_{0.5}Ga_{0.5}As$ self-assembled QDs in GaP emitting in the red part of the spectrum. This system provides large wavelength tunability as the In fraction can be varied from 0.07-0.50 without introducing dislocations; additionally it should provide deeper confinement for carriers than InP/GaP. Subsequently, room temperature emission was measured from $In_{0.3}Ga_{0.7}As$/GaP QDs[151]; measured temperature dependence of emission and supporting tight binding calculations indicated good confinement of carriers and type-I emission. Here, we further characterize this materials system, integrate it with photonic nanostructures that enhance the emission of the QDs, and observe evidence indicative of emission from individual QDs.

8.3.1 Temperature-dependent QD luminescence

The QDs are grown by solid source molecular beam epitaxy in the center of a 200 nm thick GaP membrane grown on top of a 500 nm layer of $Al_{0.8}Ga_{0.2}P$ on a (001) GaP substrate. Fig. 8.7a shows the measured QD photoluminescence (PL) as a function of temperature from 25K to 300K in a continuous flow helium cryostat using 700 μW excitation power from a 405 nm continuous wave (CW) diode laser. (The power level was chosen to maintain a constant integration time on the spectrometer CCD for all temperatures.) The center wavelength of the QD emission redshifts by 30 nm from 25K to 300K. The large full width half maximum of the emission is expected to result from inhomogeneous broadening due to variation in the physical size of the QDs[79]. Fig. 8.7b shows that for higher pump powers, the QD spectrum broadens on the high energy side and the integrated intensity is nonlinear as a function of power, indicating the presence of excited states. To characterize the confinement of carriers in the QDs, we study the intensity of QD emission as a function of temperature. Fig. 8.7c shows the emission intensity integrated across the low energy half of QD PL spectrum (to minimize the contribution of excited states) from Fig. 8.7a. The emission intensity decreases by a factor of 4 from cryogenic temperatures to room temperature. Fig. 8.7d shows a fit of this integrated intensity to an Arrenhius model (assuming a temperature-independent radiative lifetime) with a single activation energy with form:

$$\frac{I(T)}{I_0} = \frac{1}{1 + C \times \exp \frac{-E_a}{kT}} \tag{8.1}$$

where $I(T)$ is the temperature-dependent intensity, I_0 is the intensity at 0K, C is a constant, k is Boltzmann's constant, and E_a is the activation energy indicating carrier confinement. We measure E_a=161 meV; this is slightly larger than the 134 meV measured by Tranh et al[151], most likely due to the larger indium content in our samples, which results in deeper confinement.

8.3.2 QD photoluminescence dynamics

We investigate the dynamics of the ensemble QD emission by studying the time-resolved photoluminescence on a streak camera when the quantum dots are excited at 400 nm by a frequency doubled Ti:Sapphire laser with a repetition rate of 80 MHz. The experimental setup is shown in Fig. 8.8a; the instrument response to the pump (12 ps) is shown in Fig. 8.8b inset. The time-resolved emission of the low energy half of the QD spectrum (Fig. 8.8b) for all temperatures shows a biexponential decay with a short component ($\tau_i \approx 250$ ps, averaged across all temperatures) followed by a decay with similar time constant ($\tau_f \approx 230$ ps) after a delay of ≈500 ps. The delay is most likely indicative of phonon-assisted transfer of carriers from the indirect GaP matrix[144]. Fig. 8.8c shows the time-resolved PL measured at 250K, indicating regions used for fitting initial and final time constants. The extracted time constants for each temperature are shown in Fig. 8.8d; error bars indicate error from fit. The short lifetime is consistent with a Type I system; the minimal temperature dependence of decay rates indicates the absence of temperature-dependent non-radiative processes.

8.3.3 Enhanced outcoupling of QD emission via photonic crystal cavities

To fabricate photonic crystal cavities, we used a different sample with a thinner 93 nm-thick GaP membrane for ease in fabrication. The photonic crystals were fabricated by top-down fabrication, including e-beam lithography, dry etching, and wet etching to remove the sacrificial AlGaP layer[8]. A scanning electron microscope (SEM) image of a fabricated sample is shown in Fig. 8.9a. Due to a difference in MBE growth parameters, the emission wavelength of the thinner sample was slightly blueshifted, as shown in Fig. 8.9b, and the QD density was lower. Fig. 8.9c shows photoluminescence, measured at 12K, from the quantum dots coupled into the linear three-hole defect photonic crystal cavity[33]. The fundamental mode of the cavity with highest quality factor (black circle) overlaps with the tail of the QD emission; the brighter higher order cavity modes[76] are more closely matched to the QD emission spectrum. Fig. 8.9d shows the fundamental cavity mode resonance at 681.7 nm; a Lorentzian fit indicates a quality factor of 2800; Fig. 8.9e shows a finite difference time domain (FDTD) simulation of the spatial distribution of the electric field intensity in the center of the membrane for this cavity mode.

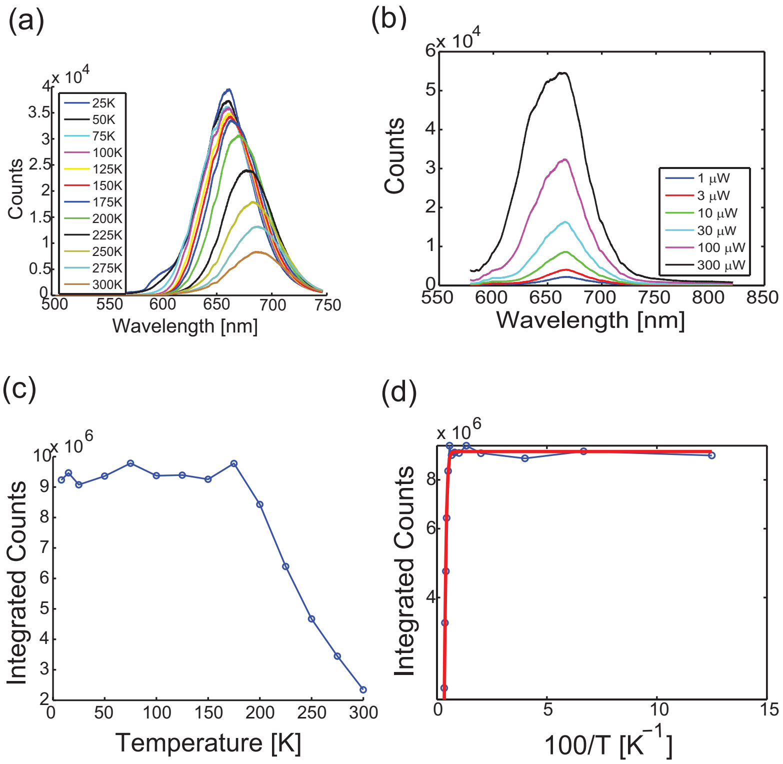

Figure 8.7: (a) QD PL from an unprocessed region of sample as temperature is varied between 25K and 300K. The pump is a 405 nm CW laser diode at 700 μW. (b) Photoluminescence as a function of pump power at 10K showing broadening at higher energies with increasing power, indicative of the presence of excited states. (c) Integrated counts of low energy half of PL spectrum (to minimize contribution of excited states, which varies with temperature). Intensity is decreased by a factor of 4 at 300K. (d) Semilog plot of integrated counts of low energy half of PL spectrum versus inverse temperature. Fit to exponential (red line) gives activation energy E_a=161 meV.

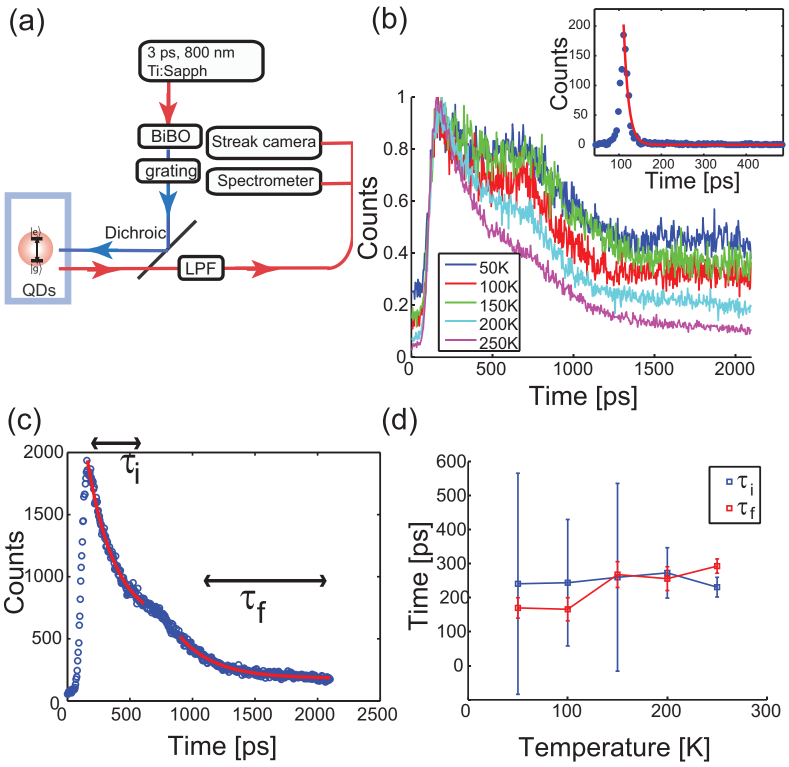

Figure 8.8: (a) Experimental setup for time-resolved measurements. 3 ps pulses at 800 nm from Ti:Sapphire laser are frequency doubled in a BiBO crystal. A grating is used to filter the 400 nm light, which is passed through a dichroic mirror onto the sample. The photoluminescence emitted by the quantum dots is transmitted through the dichroic, passed through a long-pass filter (LPF) to remove any residual pump, and sent to a spectrometer or streak camera (for time-resolved measurements). (b) Time-resolved streak camera measurements showing lifetime integrated across low energy half of PL spectrum for different temperatures. Inset: excitation pulse at 400 nm. Red line indicates fit with decay time 12 ps, limited by instrument resolution. (c) Exponential fits of time-resolved data at 250K, showing initial and final decay times τ_i and τ_f. (d) Measured lifetimes as a function of sample temperature.

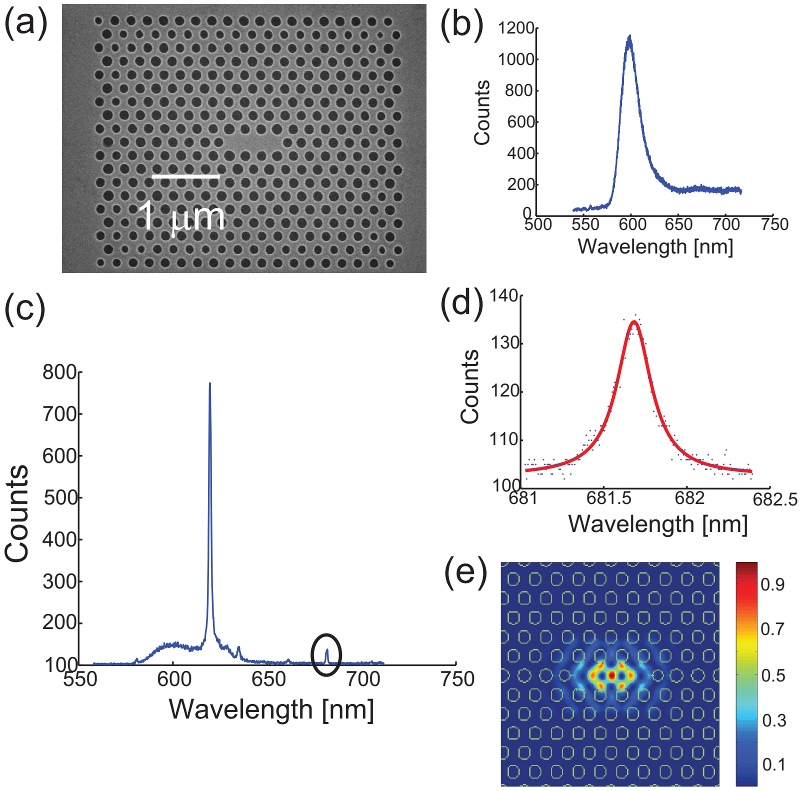

Figure 8.9: (a) SEM image of photonic crystal nanocavity. (b) PL measured at 12K with 405 nm CW pump from unprocessed region of thinner sample used for photonic crystal measurements. QD wavelength is slightly blueshifted from Fig. 1. (c) PL measurement indicating emission of quantum dots coupled into cavity modes. Fundamental cavity mode is indicated by black circle. (d) Lorenztian fit of fundamental cavity mode at 681.7 nm with Q=2800. (e) FDTD-simulated electric field intensity for fundamental cavity mode.

8.3.4 Spectral features indicative of single quantum dot emission

By measuring the cavity-enhanced QD emission, we are able to observe indications of single quantum dot emission lines at temperatures below 60K. Fig. 8.10a shows the low temperature PL spectrum with a CW pump from another photonic crystal cavity on the chip. The black circle indicates the higher order mode of interest which we use to enhance the quantum dot emission outcoupling. The inset shows the spatial profile of electric field intensity for the mode of interest, calculated by the FDTD method. Fig. 8.10b shows a high resolution spectrum measured at 10K of the QD and cavity mode at 610 nm (black circle in Fig. 8.10a). At low power, two narrow lines appear to saturate (as would be expected for single QDs) as power is increased above about 30 μW. At higher powers, we recover the Lorentzian lineshape of the photonic crystal cavity mode, as the intensity in the cavity mode continues to grow while intensity from the individual QD lines has saturated.

Fig. 8.10c shows the wavelength shift of quantum dots and cavity as a function of temperature, indicating a quadratic redshift in dot emission as temperature is increased, as expected due to the approximately quadratic shift in material band gaps in this temperature range[152]. Quantum dot lines are measured at 500 nW (far below QD saturation), while the cavity is measured at 100 μW (above QD saturation). The quantum dot emission wavelength changes at a different rate than the cavity emission, confirming that the narrow lines are not associated with a cavity mode. Fig. 8.10d shows the change in full width half max (FWHM) of the observed spectral lines at 1 μW power as a function of temperature measured. The narrow QD-like lines show an increase in linewidth as the temperature is raised, as expected for single quantum dots, while the cavity linewidth remains roughly unchanged in the same temperature range. Further confirmation of single QD behavior could be obtained from photon statistics measurements. We did not obtain sufficient signal-to-noise from the cavity to perform such measurements in this case. An improvement in the signal-to-noise, for example by improving the cavity quality factor, would also allow an investigation of the time-resolved dynamics of a single QD coupled to the cavity, where Purcell

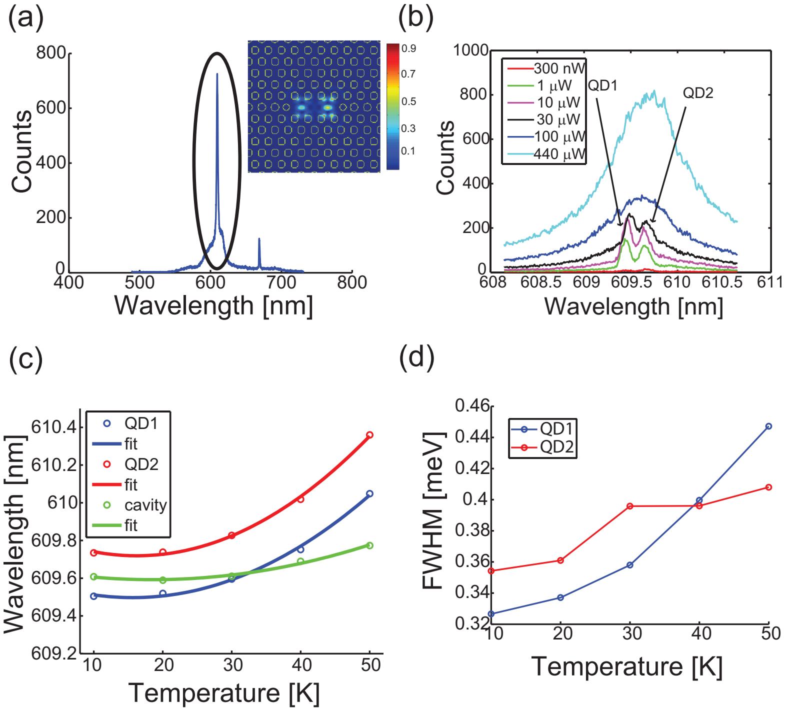

Figure 8.10: (a) PL from a different photonic crystal cavity structure with higher order cavity mode aligned to wavelength of strongest QD PL measured with 405 nm CW pump. Black circle indicates mode of interest. Inset: FDTD-simulated electric field intenstiy for higher order cavity mode indicated by circle in (a). (b) High resolution spectra of QD PL from cavity in (a). Measurements are taken at 10K. The two single lines at low power are indicative of single quantum dots. (c) Change in wavelength of quantum dots (measured at 500 nW) and cavity (measured at 100 μW) as a function of temperature. Solid lines indicate quadratic fits. (d) Change in QD linewidth as a function of temperature.

enhancement is expected[120] in this regime.

8.3.5 Conclusions

In conclusion, we have studied the properties of two photoluminescent quantum emitters (DNQDI molecules and InGaAs/GaP quantum dots) at visible wavelengths coupled to GaP photonic crystal cavities.

We have demonstrated the coupling of DNQDI fluorescent molecules and photonic crystal cavities with resonances in the far-red and near-infrared wavelengths and quality factors up to 12,000. By exposing and developing the molecule's polymer host using electron beam lithography, we localize the molecule to the cavity region. Our results show that molecules can be coupled to high quality factor photonic crystal cavities and easily localized to the spatial location of the nanoscale cavity using standard lithographic techniques. We also investigated the low-temperature photoluminescence of DNQDI and performed preliminary characterization of spin-grown thin film crystals with DNQDI embedded.

We have also measured the temperature-dependent photoluminescence emitted by $In_{0.5}Ga_{0.5}As$ quantum dots embedded in a GaP membrane, indicating good carrier confinement with only a four-fold decrease in emitted intensity from cryogenic to room temperature. We studied the temperature-dependent time-resolved photoluminescence, showing a biexponential decay with time constants of ≈ 200 ps. We observed enhanced emission into the modes of a photonic crystal cavity and narrow lines consistent with single quantum dot emission. The materials system is compatible with monolithic integration on Si and is also promising for quantum applications. The quantum dot wavelength is matched to the high efficiency region of silicon APDs and could be downconverted to telecommunication wavelengths through integration with photonic nanostructures[9, 11, 10, 103].

Chapter 9

Conclusions

This dissertation has presented a framework for three-wave mixing devices in III-V semiconductor photonic crystals. This enables miniaturization of nonlinear frequency conversion devices by reducing the required optical power and device size and allowing integration with semiconductor optoelectronic materials.

The main results presented were:

- The first demonstration photonic crystal cavities in gallium phosphide
- The demonstration of 430%/W (10^{-5} for 11 μW coupled power) continuous wave second harmonic generation in gallium phosphide photonic crystal cavities, an 8-orders of magnitude improvement on previous work in InP [7]
- The first demonstration of continuous wave sum-frequency generation in photonic crystal cavities, fabricated in GaP
- The first demonstration of second harmonic generation in photonic crystal waveguides, fabricated in GaP
- The demonstration of the fastest optically pumped single photon source, based on a quantum dot pumped by intracavity second harmonic generation from a telecom-wavelength laser

- The design, fabrication, and characterization of the largest frequency separation multiply resonant photonic crystal cavities (more than 600 nm resonant wavelength separation measured experimentally)
- The first demonstration of lithographic techniques to align thin films of molecules to high-Q photonic crystal cavities
- Spectral and temporal characterization of InGaAs/GaP quantum dot luminescence, including the first observation of narrow spectral lines indicative of single quantum dots

9.1 Outlook

This work could immediately be built upon primarily by integrating and extending the multiply resonant design presented in Chap. 7 to improve upon the work presented in earlier chapters. The design and fabrication of these structures could be extended to allow even larger frequency separation to enable triply-resonant three-wave mixing. By fabricating these multiply resonant structures on (111)-oriented GaAs or GaP, it should be possible to improve the efficiency of second harmonic and sum-frequency generation, and also allow the observation of difference frequency generation, which is a prerequisite to optical parametric oscillation and spontaneous parametric downconversion (which can generate entangled photon pairs). All the work presented in this dissertation could be scaled to longer wavelengths deep into the infrared to provide tunable light sources at frequencies critical for molecular and gas sensing[153] This cavity design is also promising for enhancing third-order nonlinear optical frequency conversion processes such as four-wave mixing and stimulated Raman scattering.

Furthermore, employing the multiply resonant cavity design with resonant frequencies at a frequency in the C-band and at the frequency of a single InAs quantum dot, could improve the rate of triggered single photon generation beyond 10 GHz for cavities with moderate Purcell factor, which would surpass the fastest electrically pumped single photon source[154, 155].

Finally, the quantum emitters at visible frequencies discussed in Chap. 8 are promising for downconversion of single photons to telecommunications wavelengths, which could also be integrated with single photon pulse shaping[156, 157].

Appendix A

Fabrication of photonic crystal structures

Photonic crystal structures were fabricated in an epitaxially grown structure on III-V wafer pieces. The process is as detailed below, and is illustrated schematically in Figure A.1. Starting in 2010, the details of each fabrication step for each sample were recorded in a spreadsheet accessible from the cleanroom as the process took place, facilitating detailed records as well as information transfer between collaborators. Fabrication in GaP and GaAs was performed using similar process; the main difference was a longer etch time for GaP compared to GaAs.

A.1 Wafer preparation

Prior to coating of wafer pieces with resist, samples were optically inspected using a microscope and then sonicated 5 minutes in acetone to remove organics.

A.2 Lithography

Photonic crystals were fabricated using a top-down approach starting with electron beam lithography. In some cases, an HDMS prime was applied first using a YES oven to enhance adhesion of resist to the samples. The positive e-beam resist used was

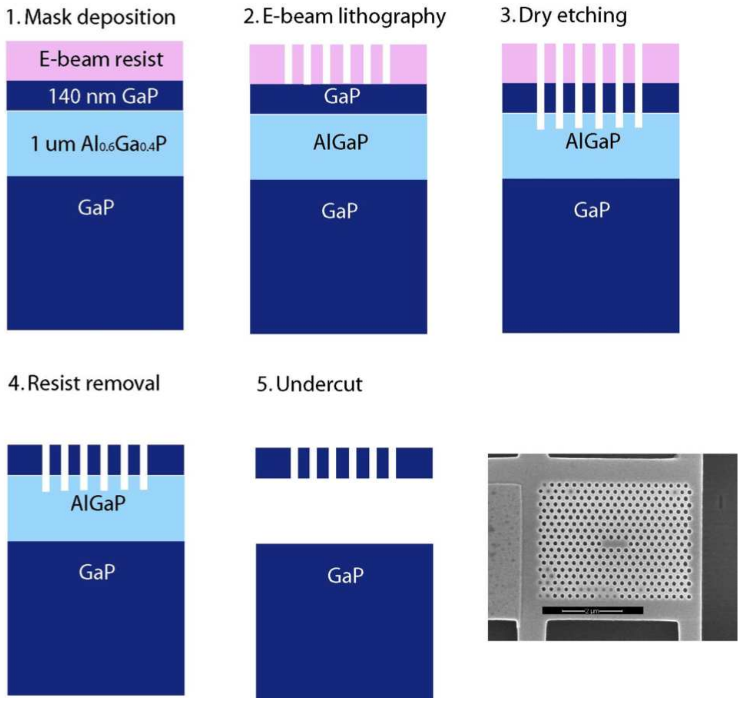

Figure A.1: Top down fabrication process for photonic crystal structures, including spinning e-beam resist, e-beam lithography, dry etching into III-V semiconductor membrane, and wet etch to remove sacrificial Al-containing layer and leave suspended high-index contrast membrane structures.

ZEP520 in an anisole solvent. The ZEP was removed from the refrigerator 30 minutes prior to spinning in order to warm to room temperature. The thickness of the layer was varied between 250 nm and 375 nm for different experiments, according to thickness and composition of the semiconductor membrane; this corresponds to a range of spin speeds from about 4000 rpm to 8000 rpm. Prior to spinning cleaved pieces of III-V wafer pieces containing layered epitaxy, a silicon piece was first coated with ZEP. The thickness of this silicon piece was then measured on a nanospec tool to confirm that the ZEP behaved according to the expected spin speed curve. The III-V wafer pieces were coated on the backside with blue sticky tape prior to spinning to prevent resist from accumulating on the backside of the wafer. Spun pieces of Si test pieces as well as III-V wafer piece samples were baked for 2 minutes at 200°C to evaporate the remaining solvent and then visually inspected using an optical microscope.

Exposure of the ZEP mask was performed using e-beam lithography. For most of the work in this thesis, a 10 kV e-beam with 7.5 μm aperture (Raith 150) was used; for later work (including parts of Chap. 7), a 100 kV e-beam tool (Jeol JBX 6300) was used to reduce lateral proximity effects. Each sample was cleaved to a size of a few mm per side, allowing hundreds of devices to be packed onto a single sample.

A standard development procedure was followed: 40 s in Xylenes, followed by a 40 s rinse in a mixture of 25% methyl iso butyl ketone and 75% isopropanol, followed by a 30 s rinse in isopropanol.

ZEP was used rather than the more standard PMMA due to its enhanced etch resistivity.

A.3 Dry Etching

Dry etching from exposed ZEP mask into GaP or GaAs membrane was performed using a Cl-based etch in a PlasmaQuest electron cyclotron resonance-reactive ion etcher (ECR-RIE). Prior to etching, the chip was glued to a Si carrier wafer using a drop of PMMA, then baked at 75°C for 2 minutes to remove remaining solvent. A standard recipe for etching is as follows:

	Step 1 (setup)	Step 2 (ignition)	Step 3
Ar (sccm)	15	15	15
BCl_3 (sccm)	10	10	10
Cl_2 (sccm)	3	3	3
Pressure (mT)	2	2	2
ECR Power (W)	0	400	200
RF Power (W)	0	40	40
He pressure (mT)	10	10	10
Temperature (°C)	13	13	13
Time (s)	70	10	250-600

The etch rate of GaP in this recipe was found to be $\approx$2 nm/s; the etch rate of GaAs was approximately 1.5 times larger.

As operating conditions varied in the PlasmaQuest varied over the years due to various state of cleaning and repairs, as well as different etches by users, a few etch parameters were adjusted to optimize etching. In particular, Cl_2 flow was varied from 1.5-3 sccm and RF power was varied in the range of 40-50W. This value of RF power corresponded to a DC bias of -50 to -40V. Starting from April 2010 (in measurements done with Sonia Buckley), prior to etching photonic crystal sample, a sample of ZEP spun on silicon was first etched for 100 s. The thickness of the ZEP was measured before and after this etch, and the average etch rate was calculated. A high ZEP etch rate would constitute a flag in the process, indicating a problem with the state of the machine. The backside helium cooling for the etches varied in the range of 3 sccm-10 sccm. Over the course of 1.5 years of measurement, the ZEP etch rate was found to be 0.3±0.2 nm/s (Fig. A.2); in general, a ZEP etch rate of >0.5 nm/s indicated a problem.

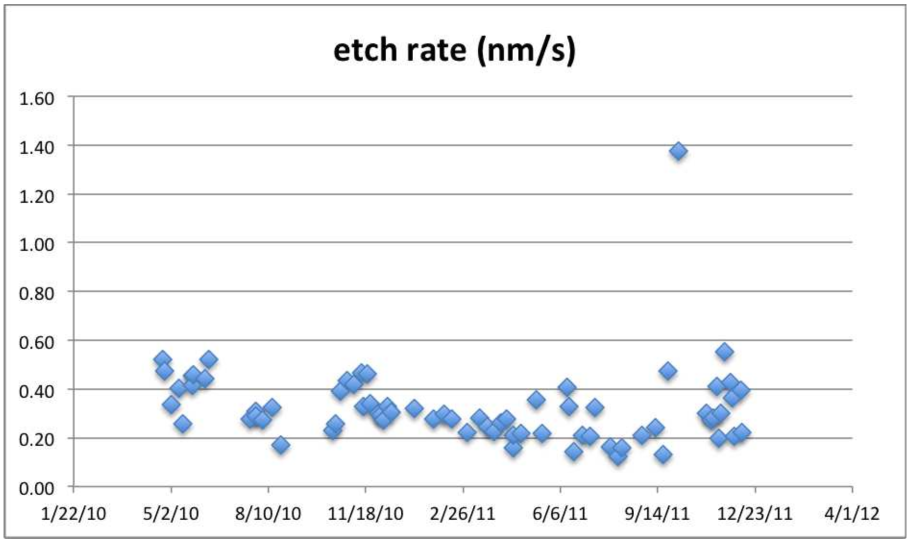

Figure A.2: Etch rate of ZEP on Si using PlasmaQuest GaP/GaAs etching recipe over 76 runs from April 2010 to December 2011. Etch rate was measured as 0.3±0.2 nm/s.

After etching, the remaining resist was removed by one of three methods: (1) sonication in acetone (2) oxygen plasma (3) overnight soak in 1165. We found option 3 (1165) to be the most robust and cause the least damage to structures.

A.4 Wet etch for undercutting

A hydrofluoric acid wet etch was used to remove the sacrificial aluminum-containing layer underneath the membrane containing the photonic crystal. For 80% Al in AlGaAs and 85% Al in AlGaP, a 7% HF etch was effective. For higher Al content, 1-2% HF was used. The HF wet etch was performed by alternating few second dips in HF and water, in order to keep Al from outgassing too quickly and breaking membrane structures. Occasionally a final 1% HF dip or citric acid dip was used to remove remaining Al crystals.

If a contaminant-free, clean surface was desired (as in experiments with DNQDI molecules in thin films in Chap. 8), a few-minute oxygen plasma clean using standard recipe oxygen.rcp was performed after wet etching.

Figure A.3 shows a single chip as it passes through each step of the process from spinning e-beam resist through undercutting.

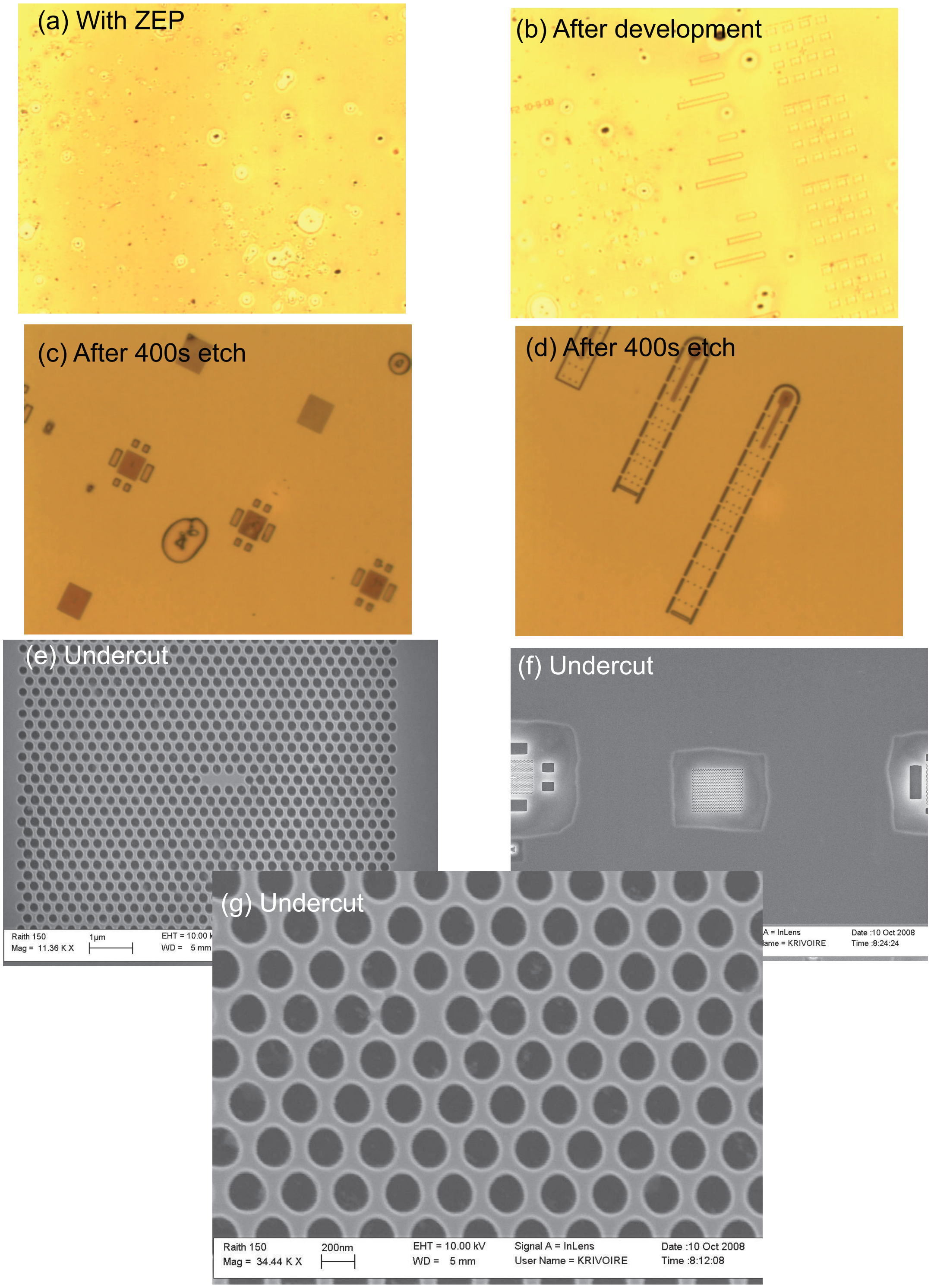

Figure A.3: (a) Optical microscope image of ZEP spun onto GaP. Defects from the original wafer propagate to the epitaxially grown layers and create perturbations in the ZEP film. (b) Optical microscope image of structures after e-beam exposure and development. (c)-(d) Optical microscope images of structures after 400s dry etch. (e)-(g) SEM images of structures after HF undercut.

Bibliography

[1] P. S. Kuo, "Thick film, orientation-patterned gallium arsenide for nonlinear optical frequency conversion," Ph.D. dissertation, Stanford University, 2008.

[2] E. Palik, *Handbook of Optical Constants.* Academic Press, 1985.

[3] P. Franken, A. Hill, C. Peters, and G. Weinreich, "Generation of optical harmonics," *Phys. Rev. Lett.*, vol. 7, pp. 118–119, 1961.

[4] T. Maiman, "Stimulated optical radiation in ruby," *Nature*, vol. 187, pp. 493–494, 1960.

[5] A. Politi, M. J. Cryan, J. G. Rarity, S. Yu, and J. L. O'Brien, "Silica-on-silicon waveguide quantum circuits," *Science*, vol. 320, no. 5876, pp. 646–696, 2008.

[6] J. S. Levy, A. Gondarenko, M. A. Foster, A. C. Turner-Foster, A. L. Gaeta, and M. Lipson, "CMOS-compatible multiple-wavelength oscillator for on-chip optical interconnects," *Opt. Express*, vol. 18, pp. 26 613–26 624, 2010.

[7] M. W. McCutcheon, J. F. Young, G. W. Rieger, D. Dalacu, S. Frédérick, P. J. Poole, and R. L. Williams, "Experimental demonstration of second-order processes in photonic crystal microcavities at submilliwatt excitation powers," *Phys. Rev. B*, vol. 76, no. 24, p. 245104, 2007.

[8] K. Rivoire, A. Faraon, and J. Vučković, "Gallium phosphide photonic crystal nanocavities in the visible," *Appl. Phys. Lett.*, vol. 93, no. 6, p. 063103, 2008.

[9] K. Rivoire, Z. Lin, F. Hatami, W. T. Masselink, and J. Vučković, "Second harmonic generation in gallium phosphide photonic crystal nanocavities with ultralow continuous wave pump power," *Opt. Express*, vol. 17, no. 25, pp. 22 609–22 615, 2009.

[10] K. Rivoire, Z. Lin, F. Hatami, and J. Vučković, "Sum-frequency generation in doubly resonant GaP photonic crystal nanocavities," *Appl. Phys. Lett.*, vol. 97, p. 043103, 2010.

[11] K. Rivoire, S. Buckley, F. Hatami, and J. Vučković, "Second harmonic generation in GaP photonic crystal waveguides," *Appl. Phys. Lett.*, vol. 98, p. 263113, 2011.

[12] K. Rivoire, S. Buckley, A. Majumdar, H. Kim, P. Petroff, and J. Vučković, "Fast quantum dot single photon source triggered at telecommunication wavelengths," *Appl. Phys. Lett.*, vol. 98, p. 083105, 2011.

[13] K. Rivoire, S. Buckley, and J. Vučković, "Multiply resonant high quality photonic crystal nanocavities," *Appl. Phys. Lett.*, vol. 99, p. 013114, 2011.

[14] ——, "Multiply resonant high quality photonic crystal nanocavities for nonlinear frequency conversion," *Opt. Express*, vol. 19, pp. 22 198–22 207, 2011.

[15] K. Rivoire, A. Kinkhabwala, F. Hatami, W. Masselink, Y. Avlasevich, K. Müllen, W. Moerner, and J. Vučković, "Lithographic positioning of fluroescent molecules on high-Q photonic crystal cavities," *Appl. Phys. Lett.*, vol. 95, p. 123113, 2009.

[16] K. Rivoire, S. Buckley, Y. Song, M. L. Lee, and J. Vučković, "Photoluminescence from $\mathrm{InGa_{0.5}As_{0.5}/GaP}$ quantum dots coupled to photonic crystal cavities," *Phys. Rev. B*, vol. 85, p. 045319, 2012.

[17] R. W. Boyd, *Nonlinear Optics.* Academic Press, 2003.

[18] Y. Shen, *The principles of nonlinear optics.* Wiley-Interscience, 1984.

[19] A. Yariv, *Quantum Electronics.* John Wiley and Sons Inc, 1975.

[20] L. A. Eyres, P. J. Tourreau, T. J. Pinguet, C. B. Ebert, J. S. Harris, M. M. Fejer, L. Becouarn, B. Gerard, and E. Lallier, "All-epitaxial fabrication of thick, orientation-patterned GaAs films for nonlinear optical frequency conversion," *Appl. Phys. Lett.*, vol. 79, no. 7, pp. 904–906, 2001.

[21] P. S. Kuo, K. L. Vodopyanov, M. M. Fejer, D. M. Simanovskii, X. Yu, J. S. Harris, D. Bliss, and D. Weyburne, "Optical parametric generation of a mid-infrared continuum in orientation-patterned GaAs," *Opt. Lett.*, vol. 31, no. 1, pp. 71–73, 2006.

[22] O. Levi, T. J. Pinguet, T. Skauli, L. A. Eyres, K. R. Parameswaran, J. J. S. Harris, M. M. Fejer, T. J. Kulp, S. E. Bisson, B. Gerard, E. Lallier, and L. Becouarn, "Difference frequency generation of 8-μm radiation in orientation-patterned GaAs," *Opt. Lett.*, vol. 27, no. 23, pp. 2091–2093, 2002.

[23] I. B. Burgess, Y. Zhang, M. W. McCutcheon, A. W. Rodriguez, J. Bravo-Abad, S. G. Johnson, and M. Loncar, "Design of an efficient terahertz sourceusing triply resonant nonlinear photonic crystal cavities," *Opt. Express*, vol. 17, no. 22, pp. 20 099–20 108, Oct 2009.

[24] A. Rodriguez, M. Soljacic, J. D. Joannopoulos, and S. G. Johnson, "$\chi^{(2)}$ and $\chi^{(3)}$ harmonic generation at a critical power in inhomogeneous doubly resonant cavities," *Opt. Express*, vol. 15, no. 12, pp. 7303–7318, 2007.

[25] H. A. Haus, *Waves and Fields in Optoelectronics.* Prentice Hall, 1983.

[26] S. M. Thon, W. T. M. Irvine, D. Kleckner, and D. Bouwmeester, "Polychromatic photonic quasicrystal cavities," *Phys. Rev. Lett.*, vol. 104, no. 24, p. 243901, Jun 2010.

[27] Y. Zhang, M. W. McCutcheon, I. B. Burgess, and M. Loncar, "Ultra-high-Q TE/TM dual-polarized photonic crystal nanocavities," *Opt. Lett.*, vol. 34, no. 17, pp. 2694–2696, 2009.

[28] S. L. McCall, A. F. J. Levi, R. E. Slusher, S. J. Pearton, and R. A. Logan, "Whispering-gallery mode microdisk lasers," *Applied Physics Letters*, vol. 60, no. 3, pp. 289–291, 1992.

[29] M. Kuwata-Gonokami, R. H. Jordan, A. Dodabalapur, H. E. Katz, M. L. Schilling, R. E. Slusher, and S. Ozawa, "Polymer microdisk and microring lasers," *Opt. Lett.*, vol. 20, no. 20, pp. 2093–2095, Oct 1995.

[30] B. Little, S. Chu, H. Haus, J. Foresi, and J.-P. Laine, "Microring resonator channel dropping filters," *Lightwave Technology, Journal of*, vol. 15, no. 6, pp. 998 –1005, 1997.

[31] M. L. Gorodetsky, A. A. Savchenkov, and V. S. Ilchenko, "Ultimate q of optical microsphere resonators," *Opt. Lett.*, vol. 21, no. 7, pp. 453–455, Apr 1996.

[32] J. D. Joannopoulos, S. G. Johnson, J. N. Winn, and R. D. Meade, *Photonic Crystals, Molding the Flow of Light.* Princeton University Press, 2008.

[33] Y. Akahane, T. Asano, B. Song, and S. Noda, "High-Q photonic nanocavity in a two-dimensional photonic crystal," *Nature*, vol. 425, no. 944, pp. 944–947, 2003.

[34] P. Lalanne, S. Mias, and J. Hugonin, "Two physical mechanisms for boosting the quality factor to cavity volume ratio of photonic crystal microcavities," *Opt. Express*, vol. 12, no. 3, pp. 458–467, Feb 2004.

[35] J. Foresi, P. Villeneuve, J. Ferra, E. Thoen, G. Steinmeyer, S. Fan, J. Joannopoulos, L. Kimerling, H. Smith, and E. Ippen, "Photonic-bandgap microcavities in optical waveguides," *Nature*, vol. 390, pp. 143–145, 1997.

[36] B. Song, S. Noda, T. Asano, and Y. Akahane, "Ultrahigh-Q photonic double heterostructure nanocavity," *Nat. Mat.*, vol. 4, pp. 207–210, 2005.

[37] Y. Tanaka, T. Asano, and S. Noda, "Design of photonic crystal nanocavity with Q-factor of $\sim 10^9$," *J. Lightwave Tech.*, vol. 26, pp. 1532–1539, 2008.

[38] M. Notomi, E. Kuramochi, and H. Taniyama, "Ultrahigh-Q nanocavity with 1d photonic gap," *Opt. Express*, vol. 16, no. 15, pp. 11 095–11 102, Jul 2008.

[39] P. B. Deotare, M. W. McCutcheon, I. W. Frank, M. Khan, and M. Lončar, "High quality factor photonic crystal nanobeam cavities," *Appl. Phys. Lett.*, vol. 94, no. 12, p. 121106, 2009.

[40] P. Barclay, K. Srinivasan, and O. Painter, "Nonlinear response of silicon photonic crystal microresonators excited via an integrated waveguide and fiber taper," *Opt. Express*, vol. 13, no. 3, pp. 801–820, Feb 2005.

[41] H. Altug, D. Englund, and J. Vuckovic, "Ultrafast photonic crystal nanocavity laser," *Nature Physics*, vol. 2, pp. 484–488, 2006.

[42] I. Fushman, E. Waks, D. Englund, N. Stoltz, P. Petroff, and J. Vuckovic, "Ultrafast nonlinear optical tuning of photonic crystal cavities," *Applied Physics Letters*, vol. 90, p. 091118, 2007.

[43] T. Tanabe, M. Notomi, S. Mitsugi, A. Shinya, and E. Kuramochi, "All-optical switches on a silicon chip realized using photonic crystal nanocavities," *Applied Physics Letters*, vol. 87, p. 151112, 2005.

[44] J. Vuckovic and Y. Yamamoto, "Photonic crystal microcavities for cavity quantum electrodynamics with a single quantum dot," *Applied Physics Letters*, vol. 82, pp. 2374–2376, 2003.

[45] S. Noda, M. Fujita, and T. Asano, "Spontaneous-emission control by photonic crystals and nanocavities," *Nature Photonics*, vol. 1, pp. 449–458, 2007.

[46] L. Childress, M. G. Dutt, J. Taylor, A. Zibrov, F. Jelezko, J. Wrachtrup, P. Hemmer, and M. Lukin, "Coherent dynamics of coupled electron and nuclear spin qubits in diamond," *Science*, vol. 314, no. 5797, pp. 281–285, 2006.

[47] A. Gruber, A. Drabenstedt, C. Tietz, L. Fleury, J. Wrachtrup, and C. von Borczyskowski, "Scanning confocal optical microscopy and magnetic resonance on single defect centers," *Science*, vol. 276, no. 5321, pp. 2012–2014, 1997.

[48] B. Lounis and W. E. Moerner, “Single photons on demand from a single molecule at room temperature,” *Nature*, vol. 407, no. 6803, pp. 491–493, 2000.

[49] B. Lounis, H. A. Bechtela, D. Gerionc, P. Alivisatos, and W. E. Moerner, “Photon antibunching in single cdse/zns quantum dot fluorescence,” *Chemical Physics Letters*, vol. 329, no. 5–6, pp. 399–404, 2000.

[50] Y. Choi, K. Hennessy, R. Sharma, E. Haberer, Y. Gao, S. DenBaars, S. Nakamura, and E. Hu, “GaN blue photonic crystal membrane nanocavities,” *Appl. Phys. Lett.*, vol. 87, p. 243101, 2005.

[51] C. Lai, P. Yu, T. Wang, H. Kuo, T. Lu, S. Wang, and C. Lee, “Lasing characteristics of a GaN photonic crystal nanocavity light source,” *Appl. Phys. Lett.*, vol. 91, p. 041101, 2007.

[52] A. Adawi, A. Chalcraft, D. Whittaker, and D. Lidzey, “Refractive index dependence of l3 photonic crystal nano-cavities,” *Optics Express*, vol. 15, no. 22, pp. 14 299–14 305, 2007.

[53] M. Barth, J. Kouba, J. Stingl, B. Lochel, and O. Benson, “Modification of visible spontaneous emission with silicon nitride photonic crystal nanocavities,” *Opt. Exp.*, vol. 15, no. 25, pp. 17 231–17 240, 2007.

[54] M. Makarova, J. Vuckovic, H. Sanda, and Y. Nishi, “Silicon-based photonic crystal nanocavity light emitters,” *Appl. Phys. Lett.*, vol. 89, p. 221101, 2006.

[55] A. Chen, S. Chua, G. Xing, W. Ji, X. Zhang, J. Dong, L. Jian, and E. Fitzgerald, “Two-dimensional AlGaInP/GaInP photonic crystal membrane lasers operating in the visible regime at room temperature,” *Appl. Phys. Lett.*, vol. 90, p. 011113, 2007.

[56] Z. Zhang, T. Yoshie, X. Zhu, J. Xu, and A. Scherer, “Visible two-dimensional photonic crystal slab laser,” *Appl. Phys. Lett.*, vol. 89, p. 071102, 2006.

[57] D. Nelson and E. Turner, “Electro-optic and piezoelectric coefficients and refractive index of gallium phosphide,” *Journal of Applied Physics*, vol. 39, no. 7, pp. 3337–3343, 1968.

[58] F. Hatami, W. Masselink, and J. Harris, “Colour-tunable light-emitting diodes based on InP/GaP nanostructures,” *Nanotechnology*, vol. 17, pp. 3703–3706, 2006.

[59] A. Baca and C. Ashby, *Fabrication of GaAs Devices.* Institution of Electrical Engineers, 2005.

[60] G. Wang, T. Ogawa, K. Murase, K. Hori, T. Soga, B. Zhang, G. Zhao, H. Ishikawa, T. Egawa, T. Jimbo, and M. Umeno, “Passivation of bulk and surface defects in GaAs grown on Si substrate by radio frequency phosphine/hydrogen plasma exposure,” *Japanese Journal of Applied Physics*, vol. 1, no. 8, pp. 4781–4784, 2001.

[61] H. Altug and J. Vuckovic, “Polarization control and sensing with two dimensional coupled photonic crystal microcavity arrays,” *Optics Letters*, vol. 30, no. 9, pp. 982–984, 2005.

[62] D. Englund, A. Faraon, I. Fushman, N. Stoltz, P. Petroff, and J. Vuckovic, “Controlling cavity reflectivity with a single quantum dot,” *Nature*, vol. 450, no. 7171, pp. 857–861, 2007.

[63] D. Englund, I. Fushman, and J. Vuckovic, “General recipe for designing photonic crystal cavities,” *Optics Express*, vol. 12, no. 16, pp. 5961–5975, 2005.

[64] K. L. Vodopyanov, M. M. Fejer, X. Yu, J. S. Harris, Y.-S. Lee, W. C. Hurlbut, V. G. Kozlov, D. Bliss, and C. Lynch, “Terahertz-wave generation in quasi-phase-matched GaAs,” *Appl. Phys. Lett.*, vol. 89, no. 14, p. 141119, 2006.

[65] I. Shoji, T. Kondo, A. Kitamoto, M. Shirane, and R. Ito, “Absolute scale of second-order nonlinear-optical coefficients,” *J. Opt. Soc. Am. B*, vol. 14, no. 9, pp. 2268–2294, 1997.

[66] L. Scaccabarozzi, M. M. Fejer, Y. Huo, S. Fan, X. Yu, and J. S. Harris, "Enhanced second-harmonic generation in AlGaAs/AlxOy tightly confining waveguides and resonant cavities," *Opt. Lett.*, vol. 31, no. 24, pp. 3626–3628, 2006.

[67] Z. Yang, P. Chak, A. D. Bristow, H. M. van Driel, R. Iyer, J. S. Aitchison, A. L. Smirl, and J. E. Sipe, "Enhanced second-harmonic generation in algaas microring resonators," *Opt. Lett.*, vol. 32, no. 7, pp. 826–828, Apr 2007.

[68] M. Liscidini, A. Locatelli, L. C. Andreani, and C. De Angelis, "Maximum-exponent scaling behavior of optical second-harmonic generation in finite multilayer photonic crystals," *Phys. Rev. Lett.*, vol. 99, p. 053907, Aug 2007.

[69] W. J. Kozlovsky, C. Nabors, and R. L. Byer, "Efficient second harmonic generation of a diode-laser-pumped CW Nd : YAG laser using monolithic MgO : LiNbO_3 external resonant cavities," *IEEE J. Quant. Elect.*, vol. 28, no. 11, pp. 2631–2654, 1988.

[70] A. Hayat and M. Orenstein, "Photon conversion processes in dispersive microcavities: Quantum-field model," *Phys. Rev. A*, vol. 77, no. 1, p. 013830, 2008.

[71] M. Liscidini and L. C. Andreani, "Highly efficient second-harmonic generation in doubly resonant planar microcavities," *Applied Physics Letters*, vol. 85, no. 11, pp. 1883–1885, 2004.

[72] T. Carmon and K. Vahala, "Visible continuous emission from a silica microphotonic device by third-harmonic generation," *Nature Phys.*, vol. 3, pp. 430–435, 2007.

[73] B. Corcoran, C. Monat, C. Grillet, D. Moss, B. Eggleton, T. White, L. O'Faolain, and T. Krauss, "Green light emission in silicon through slow-light enhanced third-harmonic generation in photonic-crystal waveguides," *Nature Photon.*, vol. 3, pp. 206–210, 2009.

[74] M. Toishi, D. Englund, A. Faraon, and J. Vučković, "High-brightness single photon source from a quantum dot in a directional-emission nanocavity," *Opt. Express*, vol. 17, no. 17, pp. 14 618–14 626, 2009.

[75] A. Faraon, E. Waks, D. Englund, I. Fushman, and J. Vučković, "Efficient photonic crystal cavity-waveguide couplers," *Appl. Phys. Lett.*, vol. 90, no. 7, p. 073102, 2007.

[76] A. R. A. Chalcraft, S. Lam, D. O'Brien, T. F. Krauss, M. Sahin, D. Szymanski, D. Sanvitto, R. Oulton, M. S. Skolnick, A. M. Fox, D. M. Whittaker, H.-Y. Liu, and M. Hopkinson, "Mode structure of the L3 photonic crystal cavity," *Appl. Phys. Lett.*, vol. 90, no. 24, p. 241117, 2007.

[77] B. Corcoran, C. Monat, M. Pelusi, C. Grillet, T. P. White, L. O'Faolain, T. F. Krauss, B. J. Eggleton, and D. J. Moss, "Optical signal processing on a silicon chip at 640 Gb/s using slow-light," *Opt. Express*, vol. 18, no. 8, pp. 7770–7781, Apr 2010.

[78] F. Hatami, W. T. Masselink, L. Schrottke, J. W. Tomm, V. Talalaev, C. Kristukat, and A. R. Goñi, "InP quantum dots embedded in GaP: Optical properties and carrier dynamics," *Phys. Rev. B*, vol. 67, no. 8, p. 085306, Feb 2003.

[79] Y. Song, P. Simmonds, and M. Lee, "Self-assembled $\mathrm{In}_{0.5}\mathrm{Ga}_{0.5}\mathrm{As}$ quantum dots on GaP," *Appl. Phys. Lett.*, vol. 97, p. 223110, 2010.

[80] D. Englund, B. Shields, K. Rivoire, F. Hatami, J. Vučković, H. Park, and M. Lukin, "Deterministic coupling of a single nitrogen vacancy center to a photonic crystal cavity," *Nano Lett.*, vol. 10, pp. 3922–3926, 2010.

[81] M. Lončar, T. Doll, J. Vučković, and A. Scherer, "Design and fabrication of silicon photonic crystal optical waveguides," *J. Lightwave Tech.*, vol. 18, pp. 1402–1411, 2009.

[82] J. Li, T. P. White, L. O'Faolain, A. Gomez-Iglesias, and T. F. Krauss, "Systematic design of flat band slow light in photonic crystal waveguides," *Opt. Express*, vol. 16, no. 9, pp. 6227–6232, Apr 2008.

[83] A. Faraon, I. Fushman, D. Englund, N. Stoltz, P. Petroff, and J. Vuckovic, "Dipole induced transparency in waveguide coupled photonic crystal cavities," *Opt. Express*, vol. 16, no. 16, pp. 12 154–12 162, Aug 2008.

[84] D. Englund, B. Ellis, E. Edwards, T. Sarmiento, J. S. Harris, D. A. B. Miller, and J. Vuckovic, "Electrically controlled modulation in a photonic crystal nanocavity," *Opt. Express*, vol. 17, no. 18, pp. 15 409–15 419, Aug 2009.

[85] M. Notomi, K. Yamada, A. Shinya, J. Takahashi, C. Takahashi, and I. Yokohama, "Extremely large group-velocity dispersion of line-defect waveguides in photonic crystal slabs," *Phys. Rev. Lett.*, vol. 87, no. 25, p. 253902, Nov 2001.

[86] X. Yu, L. Scaccabarozzi, J. J. S. Harris, P. S. Kuo, and M. M. Fejer, "Efficient continuous wave second harmonic generation pumped at 1.55 μm in quasi-phase-matched AlGaAs waveguides," *Opt. Express*, vol. 13, no. 26, pp. 10 742–10 748, Dec 2005.

[87] J. Vučković, M. Lončar, H. Mabuchi, and A. Scherer, "Optimization of Q factor in photonic crystal microcavities," *IEEE J. Quant. Electron.*, vol. 38, pp. 850–856, 2002.

[88] G. Shambat, K. Rivoire, J. Lu, F. Hatami, and J. Vučković, "Tunable-wavelength second harmonic generation from gap photonic crystal cavities coupled to fiber tapers," *Opt. Express*, vol. 18, no. 12, pp. 12 176–12 184, Jun 2010.

[89] C. Langrock, E. Diamanti, R. V. Roussev, Y. Yamamoto, M. M. Fejer, and H. Takesue, "Highly efficient single-photon detection at communication wavelengths by use of upconversion in reverse-proton-exchanged periodically poled linbo3 waveguides," *Opt. Lett.*, vol. 30, no. 13, pp. 1725–1727, 2005.

[90] M. A. Albota and F. N. C. Wong, "Efficient single-photon counting at 1.55 μm by means of frequency upconversion," *Opt. Lett.*, vol. 29, no. 13, pp. 1449–1451, 2004.

[91] A. Beveratos, R. Brouri, T. Gacoin, J.-P. Poizat, and P. Grangier, "Nonclassical radiation from diamond nanocrystals," *Phys. Rev. A*, vol. 64, p. 061802(R), 2001.

[92] P. Michler, A. Kiraz, C. Becher, W. Schoenfeld, P. Petroff, L. Zhang, E. Hu, and A. Imamoglu, "A quantum dot single-photon turnstile device," *Science*, vol. 290, pp. 2282–2285, 2000.

[93] A. Kohn, M. Hennrich, and G. Rempe, "Deterministic single-photon source for distributed quantum networking," *Phys. Rev. Lett.*, vol. 89, p. 067901, 2002.

[94] N. Gisin, G. Ribordy, W. Tittel, and H. Zbinden, "Quantum cryptography," *Rev. Mod. Phys.*, vol. 74, no. 1, pp. 145–195, Mar 2002.

[95] E. Knill, R. Laflamme, and G. Milburn, "A scheme for efficient quantum computation with linear optics," *Nature*, vol. 409, pp. 46–52, 2001.

[96] C. Santori, D. Fattal, J. Vučković, G. Solomon, and Y. Yamamoto, "Indistinguishable photons from a single-photon device," *Nature*, vol. 419, pp. 494–497, 2002.

[97] Z. Yuan, B. Kardynal, R. Stevenson, A. Shields, C. Lobo, K. Cooper, N. Beattie, D. Ritchie, and M. Pepper, "Electrically driven single photon source," *Science*, vol. 295, pp. 102–105, 2002.

[98] M. T. Rakher, N. G. Stoltz, L. A. Coldren, P. M. Petroff, and D. Bouwmeester, "Polarization-switchable single photon source using the stark effect," *Appl. Phys. Lett.*, vol. 93, no. 9, p. 091118, 2008.

[99] B. Ellis, T. Sarmiento, M. Mayer, B. Zhang, J. Harris, E. Haller, and J. Vuckovic, "Electrically pumped photonic crystal nanocavity light sources using a laterally doped p-i-n junction," *Appl. Phys. Lett.*, vol. 96, p. 181103, 2010.

[100] S. Kako, C. Santori, K. Hoshino, S. Gotzinger, Y. Yamamoto, and Y. Arakawa, "A gallium nitride single-photon source operating at 200k," *Nat. Mat.*, vol. 5, pp. 887–892, 2006.

[101] C. Santori, D. Fattal, J. Vučković, G. Solomon, E. Waks, and Y. Yamamoto, "Submicrosecond correlations in photoluminescence from InAs quantum dots," *Phys. Rev. B*, vol. 69, p. 205324, 2004.

[102] J. Vučković, D. Fattal, C. Santori, G. Solomon, and Y. Yamamoto, "Enhanced single-photon emission from a quantum dot in a micropost microcavity," *Appl. Phys. Lett.*, vol. 82, pp. 3596–3598, 2003.

[103] M. W. McCutcheon, D. E. Chang, Y. Zhang, M. D. Lukin, and M. Loncar, "Broadband frequency conversion and shaping of single photons emitted from a nonlinear cavity," *Opt. Express*, vol. 17, no. 25, pp. 22 689–22 703, 2009.

[104] M. W. McCutcheon, G. W. Rieger, I. W. Cheung, J. F. Young, D. Dalacu, S. Frederick, P. J. Poole, G. C. Aers, and R. L. Williams, "Resonant scattering and second-harmonic spectroscopy of planar photonic crystal microcavitites," *Appl. Phys. Lett.*, vol. 87, p. 221110, 2005.

[105] M. Galli, D. Gerace, K. Welna, T. F. Krauss, L. O'Faolain, G. Guizzetti, and L. C. Andreani, "Low-power continuous-wave generation of visible harmonics in silicon photonic crystal nanocavities," *Nature Photonics*, vol. 4, pp. 37–40, 2010.

[106] M. W. McCutcheon, P. B. Deotare, Y. Zhang, and M. Lončar, "High-Q transverse-electric/transverse-magnetic photonic crystal cavities," *Appl. Phys. Lett.*, vol. 98, p. 111117, 2011.

[107] M. McCutcheon and M. Lončar, "Design of a silicon nitride photonic crystal nanocavity with a quality factor of one million for coupling to a diamond nanocrystal," *Opt. Express*, vol. 16, pp. 19 136–19 145, 2008.

[108] C. Sauvan, G. Lecamp, P. Lalanne, and J. Hugonin, "Modal-reflectivity enhancement by geometry tuning in photonic crystal microcavities," *Opt. Express*, vol. 13, no. 1, pp. 245–255, Jan 2005.

[109] S. Johnson and J. Joannopoulos, "Block-iterative frequency-domain methods for Maxwell's equations in a planewave basis," *Opt. Express*, vol. 8, no. 3, pp. 173–190, Jan 2001.

[110] S. G. Johnson, C. Manolatou, S. Fan, P. R. Villeneuve, J. D. Joannopoulos, and H. A. Haus, "Elimination of cross talk in waveguide intersections," *Opt. Lett.*, vol. 23, no. 23, pp. 1855–1857, Dec 1998.

[111] Q. Quan, P. Deotare, and M. Lončar, "Photonic crystal nanocavity strongly coupled to the feeding waveguide," *Appl. Phys. Lett.*, vol. 96, p. 203102, 2010.

[112] I. Luxmoore, E. Ahmadi, A. Fox, M. Hugues, and M. Skolnick, "Unpolarized H1 photonic crystal nanocavities fabricated by stretched lattice design," *Appl. Phys. Lett.*, vol. 98, p. 041101, 2011.

[113] O. Benson, C. Santori, M. Pelton, and Y. Yamamoto, "Regulated and entangled photons from a single quantum dot," *Phys. Rev. Lett.*, vol. 84, no. 11, pp. 2513–2516, Mar 2000.

[114] K. Hennessy, C. Hogerle, E. Hu, A. Badolato, and A. Imamoglu, "Tuning photonic nanocavities by atomic force microscope nano-oxidation," *Appl. Phys. Lett.*, vol. 89, p. 041118, 2006.

[115] H. Lee, S. Kiravittaya, S. Kumar, J. Plumhof, L. Balet, L. Li, M. Francardi, A. Gerardino, A. Fiore, A. Rastelli, and O. Schmidt, "Local tuning of photonic crystal nanocavity modes by laser-assisted oxidation," *Appl. Phys. Lett.*, vol. 95, p. 191109, 2009.

[116] A. Faraon and J. Vučković, "Local temperature control of photonic crystal devices via micron-scale electrical heaters," *Appl. Phys. Lett.*, vol. 95, p. 043102, 2009.

[117] M. Galli, S. Portalupi, M. Belotti, L. Andreani, L. O'Faolain, and T. Krauss, "Light scattering and Fano resonances in high-Q photonic crystal nanocavities," *Appl. Phys. Lett.*, vol. 94, p. 071107, 2009.

[118] D. Englund and J. Vučković, "A direct analysis of photonic nanostructures," *Opt. Express*, vol. 14, no. 8, pp. 3472–3483, Apr 2006.

[119] M. Banaee and J. F. Young, "Squeezed state generation in photonic crystal microcavities," *Opt. Express*, vol. 16, pp. 20 908–20 919, 2008.

[120] D. Englund, D. Fattal, E. Waks, G. Solomon, B. Zhang, T. Nakaoka, Y. Arakawa, Y. Yamamoto, and J. Vučković, "Controlling the spontaneous emission rate of single quantum dots in a 2D photonic crystal," *Phys. Rev. Lett.*, vol. 95, p. 013904, 2005.

[121] M. Bajcsy, A. Faraon, K. Rivoire, A. Majumdar, and J. Vuckovic, "Atoms and photonic crystal cavities," 2011, annual Meeting of the APS Division of Atomic, Molecular and Optical Physics.

[122] T. Yoshie, A. Scherer, J. Hendrickson, K. Khitrova, H. Gibbs, G. Rupper, C. Ell, O. Shchekin, and D. Deppe, "Vacuum Rabi splitting with a single quantum dot in a photonic crystal nanocavity," *Nature*, vol. 432, p. 200, 2004.

[123] M. Barth, N. Nusse, B. Lochel, and O. Benson, "Controlled coupling of a single-diamond nanocrystal to a photonic crystal cavity," *Opt. Lett.*, vol. 34, p. 1108, 2009.

[124] P. Barclay, C. Santori, K.-M. Fu, R. Beausoleil, and O. Painter, "Coherent interference effects in a nano-assembled diamond nv center cavity-qed system," *Opt. Express*, vol. 17, p. 8081, 2009.

[125] K. Hennessy, A. Badolato, M. Winger, D. Gerace, M. Atature, S. Gulde, S. Falt, E. Hu, and A. Imamoglu, "Quantum nature of a strongly coupled single quantum dot-cavity system," *Nature*, vol. 445, p. 896, 2007.

[126] S. Thon, M. Rakher, H. Kim, J. Gudat, W. Irvine, P. Petroff, and D. Bouwmeester, "Strong coupling through optical positioning of a quantum dot in a photonic crystal cavity," *Appl. Phys. Lett.*, vol. 94, p. 111115, 2009.

[127] Y. Avlasevich, S. Muller, P. Erk, and K. Mullen, "Novel core-expanded rylenebis(dicarboximide) dyes bearing pentacene units: Facile synthesis and

photophysical properties," *Chem. A – European Journal*, vol. 13, pp. 6555–6561, 2007.

[128] H. Zhou, B. Chong, P. Stopford, G. Mills, A. Midha, L. Donaldson, and J. Weaver, "Lithographically defined nano and micro sensors using "float coating" of resist and electron beam lithography," *J. Vac. Sci. Tech. B.*, vol. 18, p. 3594, 2000.

[129] L. Martiradonna, T. Stomeo, M. D. Giorgi, R. Cingolani, and M. D. Vittorio, "Lithographic nano-pattering of colloidal nanocrystal emitters for the fabrication of waveguide photonic devices," *Microelectronic Engineering*, vol. 83, p. 1478, 2006.

[130] A. Faraon, P. E. Barclay, C. Santori, K.-M. C. Fu, and R. G. Beausoleil, "Resonant enhancement of the zero-phonon emission from a colour center in a diamond cavity," *Nature Photon.*, vol. 5, pp. 301–305, 2011.

[131] B. Kozankiewicz, J. Bernard, and M. Orrit, "Single molecule lines and spectral hole burning of terrylene in different matrices," *The Journal of Chemical Physics*, vol. 101, no. 11, pp. 9377–9383, 1994.

[132] A. Kiraz, M. Ehrl, C. Brauchle, and A. Zumbusch, "Low temperature single molecule spectroscopy using vibronic excitation and dispersed fluorescence detection," *The Journal of Chemical Physics*, vol. 118, no. 24, pp. 10 821–10 824, 2003.

[133] C. A. Werley and W. E. Moerner, "Single-molecule nanoprobes explore defects in spin-grown crystals," *The Journal of Physical Chemistry B*, vol. 110, no. 38, pp. 18 939–18 944, 2006.

[134] R. Pfab, J. Zimmermann, C. Hettich, I. Gerhardt, A. Renn, and V. Sandoghdar, "Aligned terrylene molecules in a spin-coated ultrathin crystalline film of p-terphenyl," *Chemical Physics Letters*, vol. 387, no. 46, pp. 490 – 495, 2004.

[135] T. J. Grassman, M. R. Brenner, S. Rajagopalan, R. Unocic, R. Dehoff, M. Mills, H. Fraser, and S. A. Ringel, “Control and elimination of nucleation-related defects in GaP/Si(001) heteroepitaxy,” *Appl. Phys. Lett.*, vol. 94, p. 232106, 2009.

[136] A. C. Lin, J. S. Harris, and M. M. Fejer, “Two-dimensional III-V nucleation on Si for nonlinear optics,” *J. Vac. Sci Tech. B*, vol. 29, p. 03C120, 2011.

[137] N. Talebi and M. Shahabadi, “All-optical wavelength converter based on a heterogeneously integrated gap on a silicon-on-insulator waveguide,” *J. Opt. Soc. Am. B*, vol. 27, no. 11, pp. 2273–2278, Nov 2010.

[138] N. Curtz, R. Thew, C. Simon, N. Gisin, and H. Zbinden, “Coherent frequency-down-conversion interface for quantum repeaters,” *Opt. Express*, vol. 18, no. 21, pp. 22 099–22 104, Oct 2010.

[139] S. Zaske, A. Lenhard, and C. Becher, “Efficient frequency downconversion at the single photon level from the red spectral range to the telecommunications c-band,” *Opt. Express*, vol. 19, no. 13, pp. 12 825–12 836, Jun 2011.

[140] A. Ugur, F. Hatami, W. T. Masselink, A. N. Vamivakas, L. Lombez, and M. Atatüre, “Single-dot optical emission from ultralow density well-isolated inp quantum dots,” *Appl. Phys. Lett.*, vol. 93, p. 143111, 2008.

[141] I. Luxmoore, E. D. Ahmadi, N. A. Wasley, A. M. Fox, A. Tartakovskii, A. B. Krysa, and M. S. Skolnick, “Control of spontaneous emission from InP single quantum dots in GaInP photonic crystal nanocavities,” *Appl. Phys. Lett.*, vol. 97, p. 181104, 2010.

[142] D. Richter, R. Roßbach, W. Schulz, E. Koroknay, C. Kessler, M. Jetter, and P. Michler, “Low-density InP quantum dots embedded in $Ga_{0.51}In_{0.49}P$ with high optical quality realized by a strain inducing layer,” *Appl. Phys. Lett.*, vol. 97, p. 063107, 2010.

[143] M. Reischle, C. Kessler, W.-M. Schulz, M. Eichfelder, R. Roßbach, M. Jetter, and P. Michler, “Triggered single-photon emission from electrically excited quantum dots in the red spectral range,” *Appl. Phys. Lett.*, vol. 97, p. 143513, 2010.

[144] F. Hatami, W. T. Masselink, L. Schrottke, J. W. Tomm, V. Talalaev, C. Kristukat, and A. R. Goñi, “InP quantum dots embedded in GaP: optical properties and carrier dynamics,” *Phys. Rev. B*, vol. 67, p. 085306, Feb 2003.

[145] F. Hatami, W. T. Masselink, and L. Shrottke, “Radiative recombination from InP quantum dots on (100) GaP,” *Appl. Phys. Lett.*, vol. 78, no. 15, pp. 2163–2165, 2001.

[146] W.-M. Schulz, M. Eichfelder, R. Roßbach, M. Jetter, and P. Michler, “InP/AlGaInP quantum dot laser emitting at 638 nm,” *Journal of Crystal Growth*, vol. 315, no. 1, pp. 123 – 126, 2011.

[147] W.-M. Schulz, R. Roßbach, M. Reischle, G. J. Beirne, M. Bommer, M. Jetter, and P. Michler, “Optical and structural properties of InP quantum dots embedded in $(\mathrm{Al}_x\mathrm{Ga}_{1-x})_0.51\mathrm{In}_0.49\mathrm{P}$,” *Phys. Rev. B*, vol. 79, p. 035329, Jan 2009.

[148] S. Gerhard, V. Baumann, S. Höfling, , and A. Forchel, “The structural and optical characterization of high areal density $\mathrm{Ga}_x\mathrm{In}_{1-x}\mathrm{P}$ quantum dots on GaP,” *Nanotechnology*, vol. 20, p. 434016, 2009.

[149] R. Leon, C. Lobo, T. Chin, J. Woodall, S. Fafard, S. Ruvimov, Z. Liliental-Weber, and M. A. S. Kalceff, “Self-forming InAs/GaP quantum dots by direct island growth,” *Appl. Phys. Lett.*, vol. 72, p. 1356, 1998.

[150] S. Gerhard, S. Kremling, S. Höfling, L. Worschech, and A. Forchel, “Short wavelength emission of AlGaInP quantum dots grown on GaP substrate,” *Nanotechnology*, vol. 22, p. 415604, 2011.

[151] T. N. Tranh, C. Robert, C. Cornet, M. Perrin, J. Jancu, N. Bertru, J. Even, N. Chevalier, H. Folliot, O. Durand, and A. L. Corre, "Self-assembled $In_{0.5}Ga_{0.5}As$ quantum dots on GaP," *Appl. Phys. Lett.*, vol. 97, p. 223110, 2010.

[152] Y. P. Varshni, "Temperature dependence of the energy gap in semiconductors," *Physica*, vol. 34, pp. 149–154, 1967.

[153] B. G. Lee, M. A. Belkin, R. Audet, J. MacArthur, L. Diehl, C. Pflugl, F. Capasso, D. C. Oakley, D. Chapman, A. Napoleone, D. Bour, S. Corzine, G. Hofler, and J. Faist, "Widely tunable single-mode quantum cascade laser source for mid-infrared spectroscopy," *Applied Physics Letters*, vol. 91, no. 23, p. 231101, 2007.

[154] D. J. Ellis, A. J. Bennett, S. J. Dewhurt, C. A. Nicoll, D. A. Ritchie, and A. J. Shields, "Cavity-enhanced radiative emission rate in a single-photon-emitting diode operating at 0.5 Ghz," *New. J. Phys.*, vol. 10, p. 043035, 2008.

[155] A. Lochmann, E. Stock, J. Tofflinger, W. Unrau, A. Toropov, A. Bakarov, V. Haisler, and D. Bimberg, "Electrically pumped, micro-cavity based single photon source driven at 1 Ghz," *Electronics Letters*, vol. 45, no. 11, pp. 566–567, 2009.

[156] M. T. Rakher and K. Srinivasan, "Subnanosecond electro-optic modulation of triggered single photons from a quantum dot," *Appl. Phys. Lett.*, vol. 98, p. 211103, 2011.

[157] M. T. Rakher, L. Ma, M. Davanço, O. Slattery, X. Tang, and K. Srinivasan, "Simultaneous wavelength translation and amplitude modulation of single photons from a quantum dot," *Phys. Rev. Lett.*, vol. 107, p. 083602, Aug 2011.